bioRxiv preprint doi: https://doi.org/10.1101/2020.09.05.284133; this version posted September 8, 2020. The copyright holder for this preprint (which was not certified by peer review) is the author/funder, who has granted bioRxiv a license to display the preprint in perpetuity. It is made available under aCC-BY-NC 4.0 International license.

Direct comparison of population receptive fields from fMRI and large-scale neurophysiological recordings in awake non-human primates.

P. Christiaan Klink[1,2*], Xing Chen[1], Wim Vanduffel[3,4,5,6] & Pieter R. Roelfsema[1,2,7]

[1] Netherlands Institute for Neuroscience, Royal Netherlands Academy of Arts and Sciences, Amsterdam, Meibergdreef 47, 1105 BA Amsterdam, The Netherlands.
[2] Psychiatry Department, Amsterdam UMC, Meibergdreef 9, 1105 AZ Amsterdam, The Netherlands.
[3] Laboratory for Neuro- and Psychophysiology, Department of Neurosciences, KU Leuven Medical School, 3000, Leuven, Belgium.
[4] Massachusetts General Hospital, Martinos Ctr. for Biomedical Imaging, Charlestown, MA, 02129, USA.
[5] Leuven Brain Institute, KU Leuven, 3000, Leuven, Belgium.
[6] Harvard Medical School, Boston, MA, 02115, USA.
[7] Department of Integrative Neurophysiology, Center for Neurogenomics and Cognitive Research, VU University, De Boelelaan 1085, 1081 HV Amsterdam, The Netherlands.

***Corresponding author:**
P.C. Klink
Netherlands Institute for Neuroscience
Meibergdreef 47, 1105BA, Amsterdam, The Netherlands
Email: c.klink@nin.knaw.nl
Phone: +31(0)20 5664581
Fax: +31(0)20 5666121

Data availability

Preprocessed MRI-data: *t.b.d. [xxx]*
Preprocessed electrophysiology data: *t.b.d. [xxx]*
Model fitting results: https://identifiers.org/neurovault.collection:8082

Code availability *(to be updated)*

Running the experiments: https://github.com/VisionandCognition/Tracker-MRI
Preprocessing MRI data: https://github.com/VisionandCognition/NHP-BIDS
Model fitting & post-processing: https://github.com/VisionandCognition/NHP-PRF
Figure generation: https://github.com/VisionandCognition/NHP-PRF

bioRxiv preprint doi: https://doi.org/10.1101/2020.09.05.284133; this version posted September 8, 2020. The copyright holder for this preprint (which was not certified by peer review) is the author/funder, who has granted bioRxiv a license to display the preprint in perpetuity. It is made available under aCC-BY-NC 4.0 International license.

Abstract

Population receptive field (pRF) modeling is a popular method to map the retinotopic organization of the human brain with fMRI. While BOLD-based pRF-maps are qualitatively similar to invasively recorded single-cell receptive fields in animals, it remains unclear what neuronal signal they truly represent. We address this question with whole-brain fMRI and large-scale neurophysiological recordings in awake non-human primates. Several pRF-models were independently fit to the BOLD signal, multi-unit spiking activity (MUA) and local field potential (LFP) power in distinct frequency bands. Our results provide a retinotopic characterization of cortical and subcortical areas, suggest brain-wide compressive (i.e., sublinear) spatial summation, and demonstrate a visually tuned deactivation of default mode network nodes. Cross-signal analysis of pRF-map structure (eccentricity-size relation) indicates that the neural underpinnings of BOLD-pRFs are area-specific. In V1, BOLD-pRFs mirror MUA, while in V4 they are more similar to the tuning of the gamma LFP-power.

Introduction

The characterization of neural response selectivity is crucial for our understanding of the mechanisms of perception and cognition. Receptive fields describe the range in feature space to which a neuron is sensitive (Hartline, 1938; Sherrington, 1906). The term is most commonly used in the context of space, where it describes stimulus locations that evoke or modulate neuronal responses, but it can be generalized to different stimulus features. While the neural response that characterizes a receptive field has classically been the rate of action potentials (Hubel and Wiesel, 1998, 1968, 1959), receptive fields can also be defined based on different neural signals such as subthreshold activity (Priebe, 2008), aspects of the local field potential (Victor et al., 1994), or fluorescence modulations derived from molecular calcium indicators (Bonin et al., 2011; van Beest et al., 2019).

Non-invasive methods lack the spatial resolution to measure the receptive field properties of single neurons, but they can characterize the receptive field properties of the aggregate neural signals they measure. The retinotopic organization of the human brain has been characterized with functional magnetic resonance imaging for decades (Wandell et al., 2007; Wandell and Winawer, 2010), first with phase-encoded approaches that identify only the most effective visual field location to evoke a response in a voxel (Engel, 2012; Engel et al., 1994; Sereno et al., 1995), and later also with methods that estimate both the location and size of a voxel's receptive field. This 'population receptive field' method (Dumoulin and Wandell, 2008; Wandell et al., 2007; Wandell and Winawer, 2015, 2010) has rapidly become a popular method to map the functional organization of the human brain. In addition to describing the retinotopic organization of retinal activation in cortical and subcortical brain areas, the method has been used to map the cortical representation of other stimulus features such as tonotopy (Thomas et al., 2015), numerosity (Harvey et al., 2015), tactile sensations (Puckett et al., 2020), and visual timing (Harvey et al., 2020).

bioRxiv preprint doi: https://doi.org/10.1101/2020.09.05.284133; this version posted September 8, 2020. The copyright holder for this preprint (which was not certified by peer review) is the author/funder, who has granted bioRxiv a license to display the preprint in perpetuity. It is made available under aCC-BY-NC 4.0 International license.

The term 'population receptive field' highlights the analogy to neuronal receptive fields. It is based on the assumption that the blood oxygen level derived signal (BOLD) that is measured with fMRI reflects the aggregate response of a large population of neurons within a voxel. Indeed, there are qualitative similarities in pRF-based characterizations of the retinotopic organization of the human cortex and the electrophysiologically determined receptive field (RF) organization of single neurons or multi-unit activity in animals (Dumoulin and Wandell, 2008). However, these comparisons may be confounded by inter-species differences, or differences in the measurement or analytical techniques that are used to generate pRF and RF properties (Barlow et al., 1966; Hubel and Wiesel, 1968).

The original method to estimate pRFs from BOLD responses (Dumoulin and Wandell, 2008) uses a forward modeling approach to fit the location and size of a symmetrical two-dimensional Gaussian pRF to the BOLD responses. This is done by minimizing the difference between the measured and predicted responses, calculated by multiplying the estimated pRF profile with the stimulus and convolving the result with a hemodynamic response function (HRF) to account for neurovascular coupling (Fig 1D). Later efforts to refine this linear pRF model have implemented a Difference-of-Gaussians pRF profile (DoG) to account for center-surround pRF configurations (Zuiderbaan et al., 2012) (Fig 1C), or a static non-linearity to account for non-linear spatial summation across receptive fields (Britten and Heuer, 1999; Kay et al., 2013; Oleksiak et al., 2011; Winawer et al., 2013). Both refinements provide better fits than the linear model, with the DoG-model showing the strongest improvements in early visual cortical areas (Zuiderbaan et al., 2012), and the non-linear spatial summation model showing better fit accuracy in more anterior extrastriate visual areas (Kay et al., 2013). The static non-linearity parameter in the non-linear pRF model revealed sub-additive spatial summation in all visual areas. For this reason, the non-linear spatial summation model has also been called the 'compressive spatial summation' (CSS) model. It is common to constrain pRF models to positive pRFs, which means that the presence of a stimulus is associated with increases of the BOLD signal. A recent study expanded this approach to allow negative pRFs based on stimulus driven decreases in BOLD activity, demonstrating that a number of areas in the so-called default mode network (DMN) were selectively inactivated by visual stimuli in humans (Szinte and Knapen, 2019).

What neuronal signal is does the fMRI BOLD signal represent best? This basic question has far-reaching consequences for the interpretation of human neuroimaging results in terms of the underlying neuronal mechanisms and is therefore a topic of ongoing debate and rigorous investigation (Arthurs and Boniface, 2002; Bartels et al., 2008; Boynton, 2011; Drew, 2019; Ekstrom, 2010; Goense and Logothetis, 2008; Logothetis, 2010, 2003, 2003; Logothetis et al., 2001; Logothetis and Wandell, 2004; Maier et al., 2008; Scholvinck et al., 2010; Winawer et al., 2013; Winder et al., 2017). Under some circumstances the BOLD signal is in agreement with both neuronal spiking and the local field potential (LFP) dynamics (Mukamel et al., 2005; Nir et al., 2007; Rees et al., 2000), while under other circumstances it is consistent with the LFP but not with spiking (Maier et al., 2008; Niessing et al., 2005; Viswanathan and Freeman, 2007), or more rarely, consistent with spiking, but not so much with the LFP (Lima et al., 2014). The LFP in itself is a complex signal and can either be regarded as a single broadband signal by taking its (rectified) amplitude or

bioRxiv preprint doi: https://doi.org/10.1101/2020.09.05.284133; this version posted September 8, 2020. The copyright holder for this preprint (which was not certified by peer review) is the author/funder, who has granted bioRxiv a license to display the preprint in perpetuity. It is made available under aCC-BY-NC 4.0 International license.

decomposed into a number of frequency components with time-varying power. Different frequency components of the LFP are correlated with different cognitive processes and distinct neurobiological processes spurring elaborate theories on their potential functions (Buzsaki, 2006, 2004; Einevoll et al., 2013; Fries, 2009; van Kerkoerle et al., 2014). The LFP is most commonly subdivided into delta (LFP-δ, ~1-4 Hz), theta (LFP-θ, ~4-8 Hz), alpha (LFP-α, ~8-16 Hz), beta (LFP-β, ~16-30 Hz) and gamma (LFP-γ, >30 Hz) frequency bands, but the exact ranges of these frequency bands are arbitrary and vary substantially across studies. The gamma band is often further divided into a low gamma band (γ_{low}, ~30-60 Hz) thought to reflect synaptic potentials in the local cortical network and a high gamma band (γ_{high}, >60 Hz) that more closely reflects local spiking activity (Ray and Maunsell, 2014, 2011). In visual cortex, low frequency components tend to dominate the LFP in the absence of visual stimulation, whereas higher frequency components become prominent when stimuli are presented.

The complex relationship between the BOLD signal and underlying neuronal dynamics raises the question of what neuronal sensitivity is captured by the pRF method when it is applied to functional imaging data. This question becomes especially relevant when the pRF-mapping method is used to make inferences about cognitive functions, for instance when comparing patients with control subjects in clinical studies (Dumoulin and Knapen, 2018). We investigated the neuronal basis of the BOLD-pRF by comparing pRFs from fMRI and large-scale neurophysiological recordings (1,024 chronic V1/V4 electrodes per subject) across awake non-human primates (Fig. 1). Four different pRF models were fit to each of the recorded neural signals (BOLD, MUA, and LFP-power, with LFP-power subdivided into five distinct frequency bands). These models were 1) a positively constrained linear model (U-LIN), 2) an unconstrained linear model (P-LIN), 3) a non-linear spatial summation model (CSS), and 4) a difference-of-Gaussians model (DoG). Cross-validated fitting results were compared across pRF models within signals and across signals within models to obtain a detailed characterization of the spatial tuning of each signal type. We also compared the electrophysiological pRF estimates with results obtained from conventional receptive field mapping procedures. Finally, we compared the structure of pRF-based retinotopic maps across the visual field (i.e., eccentricity-size relationship) of the BOLD-defined pRFs with the range of electrophysiology-pRFs. These intraspecies crossmodal comparisons provide insight into the neurophysiological basis of the BOLD signal, and directly benchmark visual field maps that are obtained with non-invasive methods against those from more precise invasive redordings.

bioRxiv preprint doi: https://doi.org/10.1101/2020.09.05.284133; this version posted September 8, 2020. The copyright holder for this preprint (which was not certified by peer review) is the author/funder, who has granted bioRxiv a license to display the preprint in perpetuity. It is made available under aCC-BY-NC 4.0 International license.

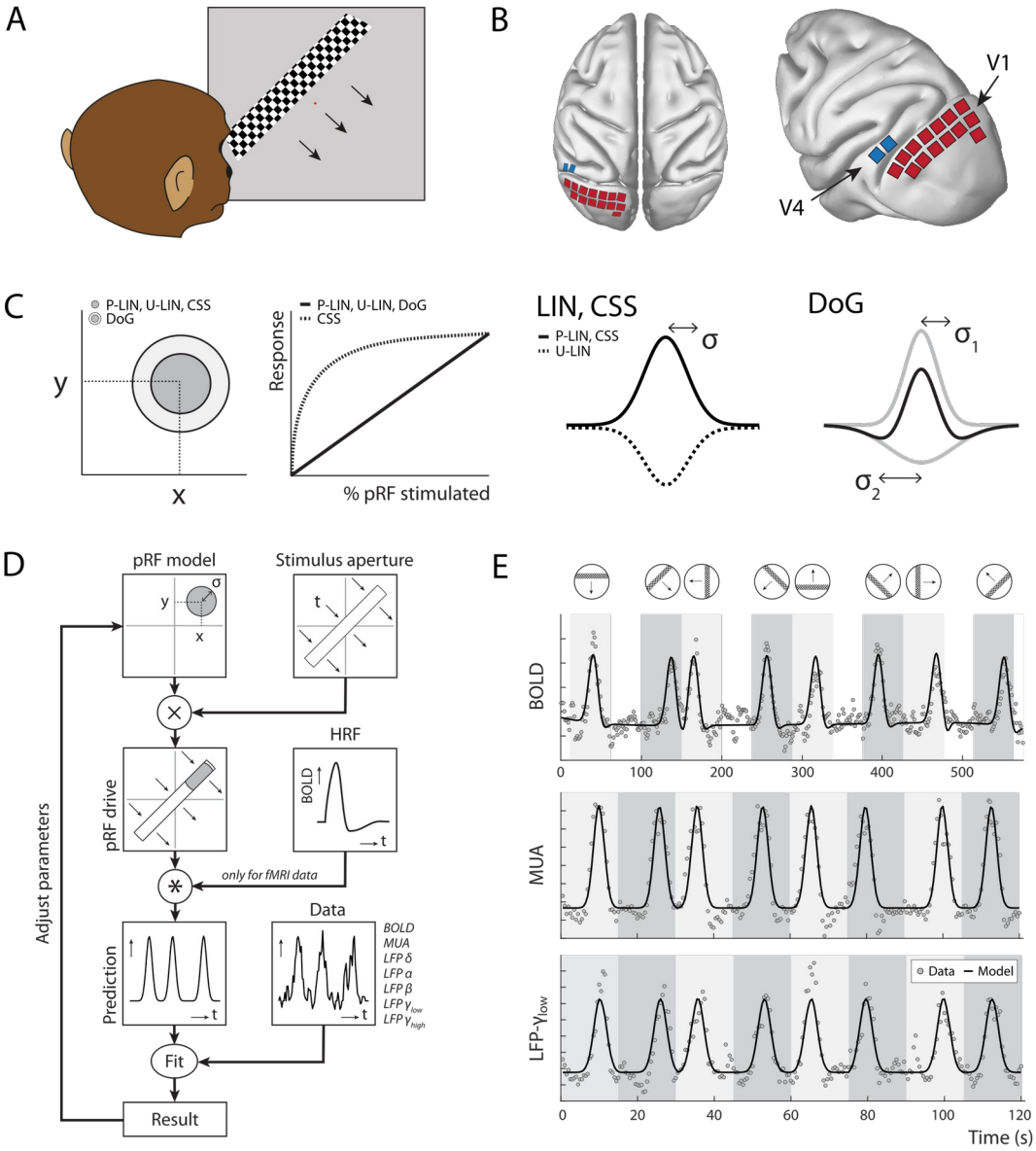

Figure 1. Experimental set-up and study design. (A) Monkeys maintained fixation on a red dot while bars with high-contrast moving checkerboards moved across the screen in eight different directions. **(B)** Two animals performed the task in the MRI-scanner. Two other animals were each implanted with 16 Utah arrays (1,024 electrodes/animal) in left visual cortex. The approximate locations of 14 V1 arrays V1 (red) and the 2 V4 arrays (blue) are depicted on the NMT standard macaque brain. **(C)** Four different pRF models were fit to all data, differing in their pRF shape (location: x,y; size: σ) and spatial summation characteristics. The Difference-of-Gaussians (DoG) pRFs are described by a 2D Gaussian with an excitatory center and an inhibitory surround (left panel: dark gray circle and light gray annulus respectively) yielding two size parameters (rightmost panel: σ_1, σ_2). All other models are described with single Gaussians that are either constrained to be positive (third panel: solid line) or, for the unconstrained linear model (U-LIN), allowed to be negative (dashed line). Non-linear spatial summation across the receptive field is implemented in the CSS model (second panel: dashed line), while all other models implemented linear summation (solid line). **(D)** The pRF model fitting procedure. A model pRF is multiplied with an 'aperture version' of the moving bar stimulus to generate a predicted response. For fMRI data this prediction was convolved with either a monkey specific or a canonical hemodynamic response function (HRF). The difference between the recorded neural signal (BOLD, MUA, LFP) and the predicted response was minimized by adjusting the pRF model parameters. **(E)** Examples of data and model fits for a V1-voxel (top panel), and a V1-electrode (middle and bottom panel). Average recorded activity (gray data points) depicts the BOLD signal (top), MUA (middle) and LFP-power in the low gamma band (bottom). Black lines are the model fits for a P-LIN pRF model. Light and dark gray areas depict visual stimulation periods. In the white periods, the animals viewed a uniform gray background.

bioRxiv preprint doi: https://doi.org/10.1101/2020.09.05.284133; this version posted September 8, 2020. The copyright holder for this preprint (which was not certified by peer review) is the author/funder, who has granted bioRxiv a license to display the preprint in perpetuity. It is made available under aCC-BY-NC 4.0 International license.

Results

Four macaque monkeys (*Macaca mulatta*) participated in this study. They were rewarded with fluid for maintaining their gaze fixed on a central fixation point presented on a frontoparallel screen. While they fixated, a bar containing full contrast moving checkerboards traversed the screen behind a large circular aperture in eight different directions (Figure 1). Two animals performed this task in a 3T horizontal bore MRI scanner. They sat in the sphinx position and viewed a screen at the end of the bore while their whole-brain BOLD activity was registered using a custom-built 8-channel phased array receive coil (Kolster et al., 2009). Two other monkeys were each implanted with 1,024 electrodes (16 Utah arrays) in the visual cortex (V1, V4). They performed the same task in an upright primate chair while neuronal activity (MUA and LFP) was registered simultaneously from all electrodes.

After preprocessing (see Material and Methods) we independently fit four pRF models to the average BOLD time-courses. These models were: (1) a linear pRF model constrained on positive visual responses (P-LIN) (Dumoulin and Wandell, 2008), (2) an unconstrained version of the linear pRF model that is also capable of capturing negative visual responses (U-LIN), (3) a non-linear 'compressive spatial summation' (CSS) pRF model (Kay et al., 2013), and (4) a difference-of-Gaussians pRF model (DoG) (Zuiderbaan et al., 2012) (Fig. 1). Fitting results were assessed based on the percentage of variance explained (R^2) and a range of model parameters describing the pRF size, shape and location (see Material and Methods for details).

BOLD pRFs

All models provided good fits to the BOLD time-courses in a range of cortical and subcortical areas known for their involvement in visual processing. The absolute percentage of variance in the BOLD signal that was explained by the pRF models was smaller than typically obtained in human neuroimaging studies, but this is not unexpected in neuroimaging studies with awake behaving animals. For both monkeys, we found robust retinotopic information in occipital, temporal, and parietal cortex (Figure 2). All these areas were responsive to stimuli in the contralateral visual field and retinotopic maps were consistent with previous reports (Figure 2C). Weaker and sparser retinotopic information was also observed in the frontal cortex, e.g. around the arcuate sulcus (area 8, including the Frontal Eye Fields) and in the ventrolateral prefrontal cortex (VLPFC). For the remainder of the manuscript we use a voxel inclusion criterion of $R^2 > 5\%$ unless otherwise noted. While fit accuracy was generally much higher than 5% for visual areas (Figure 2A, bottom panel) this relatively low threshold also allows inclusion of areas with weaker retinotopic information, including the more frontal areas and some subcortical regions (where the signal that is picked up by our surface coils had a much lower SNR(. Figure 2B shows the number of voxels within a range of areas for which the models explained more than 5% of the variance (See Supplemental Figure S1 for proportionals). Functional parcellation of visual areas based on field sign inversions around horizontal and vertical meridians lined-up well with a probabilistic atlas, co-registered to the individual animal's anatomy (D99, Reveley et al., 2016).

bioRxiv preprint doi: https://doi.org/10.1101/2020.09.05.284133; this version posted September 8, 2020. The copyright holder for this preprint (which was not certified by peer review) is the author/funder, who has granted bioRxiv a license to display the preprint in perpetuity. It is made available under aCC-BY-NC 4.0 International license.

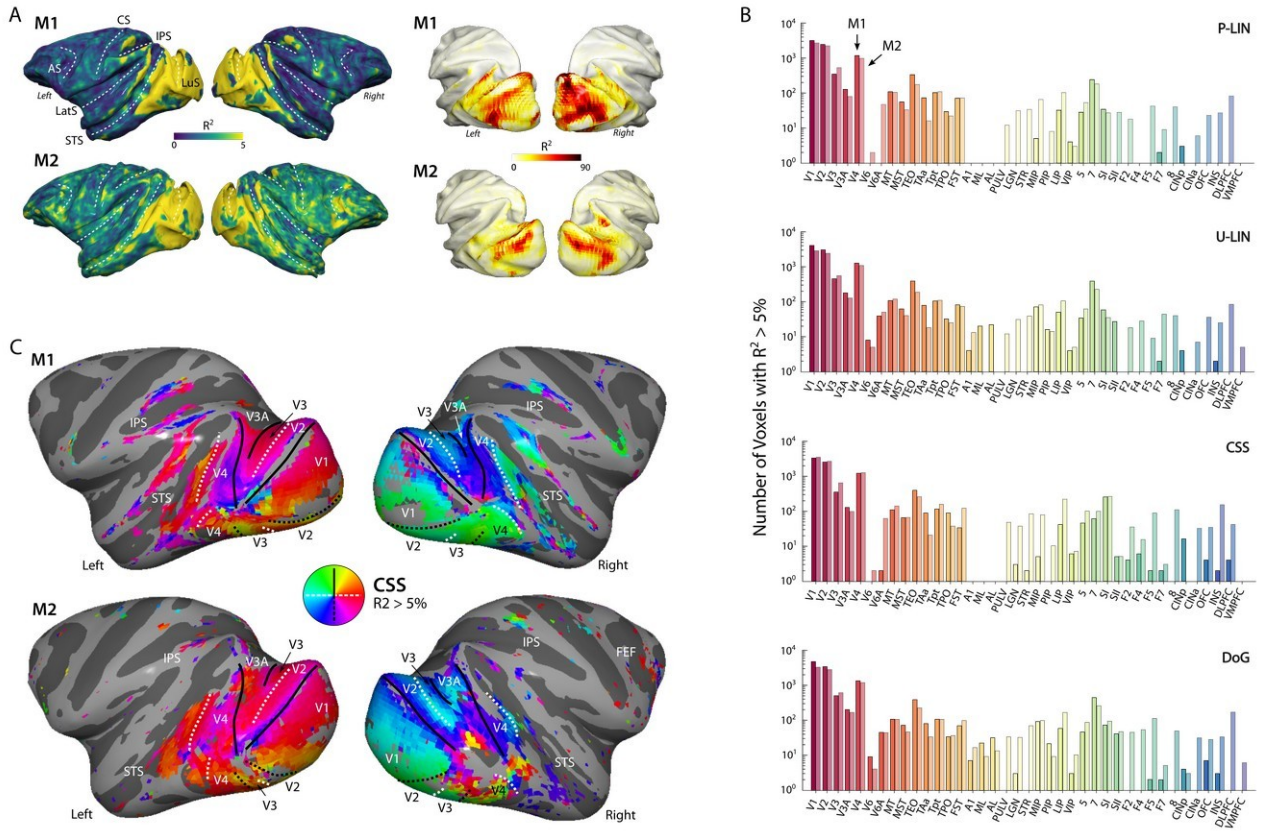

Figure 2. PRF model fits and retinotopic maps. (A) R^2 value map of the CSS pRF-model projected on the surface rendering of the brains of two monkeys (M1, M2). The right panel illustrates that the R2 value in the visual cortex is generally much higher than 5% (going up to ~90%) but the chosen color range in the left panels also visualizes the weaker retinotopic information elsewhere in the cortex. (*AS: Arcuate Sulcus; CS: Central Sulcus; IPS: Intraparietal Sulcus; LatS: Lateral Sulcus; LuS: Lunate Sulcus; STS: Superior Temporal Sulcus*) **(B)** Number of voxels with an R2 value larger than 5% per brain area and subject for each model. Note the logarithmic scale. See Supplemental Figure S1 for proportions per ROI, and Supplemental Table T1 for all ROI abbreviations. **(C)** Polar angle maps for both subjects, derived from the fits with the CSS model, thresholded at R^2 > 5%, and displayed on the inflated cortical surfaces. Functional delineation of several visual areas is superimposed. (*IPS: Intraparietal Sulcus; STS: Superior Temporal Sulcus; FEF: Frontal Eye Fields*).

Subcortically, the lateral geniculate nucleus (LGN), pulvinar and striatum were dissociable from their surrounding areas on the basis of a higher pRF fit accuracy. In both monkeys, the bilateral LGNs contained clear retinotopic maps (Figure 3A). Results were less consistent for the pulvinar and striatum. A retinotopic organization was evident in the bilateral pulvinar of M1, but some of the pRFs in M2 were rather large and crossed the vertical meridian resulting in noisy polar angle maps (Figure 3A). In M2, we found a robust retinotopic map for the contralateral visual field in the head of the caudate nucleus and anterior putamen (Figure 3B). These maps were also present, but less pronounced, in M1. In the more posterior putamen, retinotopic maps were noisier, and they seemed to be dominated by the ipsilateral visual field (Figure 3C). In both animals, the right ventral striatum (Nucleus Accumbens) contained pRFs that were sensitive to the lower right (i.e., ipsilateral) visual field. No consistent visual tuning was observed in the left ventral striatum (Supplemental Figure S2).

bioRxiv preprint doi: https://doi.org/10.1101/2020.09.05.284133; this version posted September 8, 2020. The copyright holder for this preprint (which was not certified by peer review) is the author/funder, who has granted bioRxiv a license to display the preprint in perpetuity. It is made available under aCC-BY-NC 4.0 International license.

Cross-validated fit accuracies were pooled across subjects and compared across the four pRF models (Figure 4A). This comparison revealed that the CSS model generally provided better fits to the data than the conventional P-LIN model (Kruskal-Wallis test on all four models, H = 21326, df = 3, p = 0; post-hoc Tukey's HSD multiple comparisons of mean rank, $R^2_{CSS} > R^2_{P\text{-}LIN}$, $p < 0.0001$). Similar to what has previously been shown in humans, the advantage of the CSS model over the P-LIN model increased when moving up the early visual hierarchy, with a notable exception for V4 where the difference was about the same as in V1 (Supplemental Figure S3). Both the U-LIN and DoG models also performed better than the standard P-LIN model (Kruskal-Wallis, Tukey's HSD, both $p < 0.0001$), with the DoG having slightly better fits on average than the U-LIN model (Kruskal-Wallis, Tukey's HSD, $p < 0.0001$). The advantage of the DoG model over the P-LIN model decreased from V1 to areas higher in the visual hierarchy, like V4 and MT.

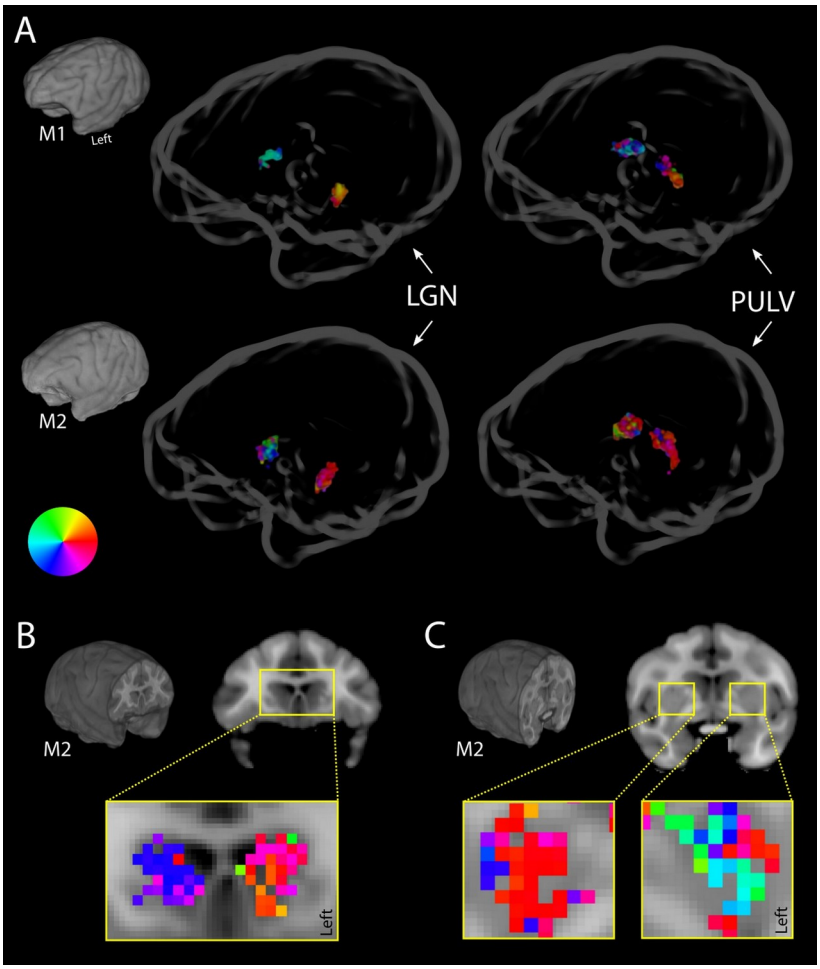

Figure 3. Subcortical retinotopy. (A) Thalamic pRFs. Both the lateral geniculate nucleus (LGN, left) and the pulvinar (PULV, right) contained retinotopic maps of the contralateral visual field in both monkeys (M1: top, M2, bottom). Voxels were thresholded at $R^2 > 3\%$ for these polar angle visualizations, due to the generally poorer fits. Results from the CSS model are shown in a 'glass' representation of the individual animals' brains. Other models produced comparable results. **(B)** In M2, the head of the caudate nucleus in the striatum contained retinotopic maps of the lower contralateral visual field. **(C)** In the more posterior striatum of M2, retinotopic information was also present. While spatial preferences were more mixed here, there seemed to be a dominant representation of the ipsilateral visual field.

bioRxiv preprint doi: https://doi.org/10.1101/2020.09.05.284133; this version posted September 8, 2020. The copyright holder for this preprint (which was not certified by peer review) is the author/funder, who has granted bioRxiv a license to display the preprint in perpetuity. It is made available under aCC-BY-NC 4.0 International license.

There was a subset of voxels for which both the DoG and U-LIN models provided much better pRF fits than the P-LIN and CSS models (Figure 4A). This dichotomy suggests that these voxels might be best characterized by a reduction or suppression of their BOLD activity in response to visual stimulation. Models that are capable of capturing negative BOLD responses (DoG and U-LIN) estimated pRFs for these voxels with either a negative gain parameter (U-LIN, median gain = -0.31, Wilcoxon Signed Rank one-tailed ($g < 0$), z = -43.9356, p = 0) (Figure 4B) or a strong inhibitory component (DoG, median normalized suppressive amplitude = 1.14, IQR 0.98-1.29) (Figure 4E, Supplemental Figure S4). There were two categories of voxels for which negative pRF fits outperformed positive pRF fits. First, in visual cortex there were voxels for which the negative component pRFs (fit with DoG or U-LIN) were all rather large and foveally located within the first several degrees from the center of the visual field, while positively constrained models (e.g., P-LIN) estimated pRFs for the same voxels to be smaller and peripherally located (Figure 4C,F).

This pattern was significant (Wilcoxon Signed Rank tests, Eccentricity: U-LIN vs. P-LIN, z = -46.40, p = 0, $\text{median}_{(P\text{-}LIN\ -\ U\text{-}LIN)} = 6.84$; DoG vs. P-LIN, z = -49.35, p = 0, $\text{median}_{(DoG\ -\ U\text{-}LIN)} = 4.71$; Size: U-LIN vs. P-LIN, z = 33.25, $p < 10^{-240}$, $\text{median}_{(P\text{-}LIN\ -\ U\text{-}LIN)} = -1.11$) and is consistent with the observation that these voxels respond positively to peripheral stimuli but reduce their activity when visual stimuli are presented in the foveal region of visual space. Such a pattern has previously been demonstrated in humans (Smith et al., 2004) and with simultaneous fMRI and direct electrical stimulation of foveal V1 regions in monkeys (Shmuel et al., 2006). The cortical locations of these particular voxels is also consistent with this explanation. In V1, for instance, voxels with the above-described tuning profile were located on the medial side of the occipital pole, an area where neurons tend to be sensitive for visual stimulation in the peripheral contra-lateral visual field (Figure 4D). We also found voxels for which both the DoG and P-LIN models estimated foveal receptive fields with the DoG model outperforming the P-LIN model. These voxels were not clustered, but scattered throughout the visual cortex (Supplemental Figure S5). The second category of voxels with good negative pRF fits comprised voxels for which the positively constrained models could not fit pRFs at all, suggesting that these voxels could only be characterized by a visually tuned reduction in BOLD activity. These voxels were primarily located around the lateral sulcus, in the medial occipital parietal cortex and at the superior border of the superior temporal sulcus in the lateral occipital parietal cortex (Figure 4G).

The fitting procedures for all models were performed both with a monkey-specific hemodynamic response function (HRF, see Material and Methods for details on how these were estimated) and with a canonical 'human' HRF. The difference between the two is that the monkey-specific HRF had a slightly faster decay than the canonical HRF (Supplemental Figure S5A). The choice of HRF had a surprisingly small effect on the fitting accuracy (Supplemental Figure S5). For the P-LIN and CSS models, there was a small but significant advantage of using the specific monkey HRF over a canonical HRF in terms of the percentage of variance explained (Wilcoxon Signed Rank, P-LIN: z = 8.41, p < 0.0001; CSS: z = 16.39, p < 0.0001). This overall difference was primarily driven by the early visual areas that were used to estimate the monkey HRF and contained most voxels with retinotopic information. For the DoG model, the canonical HRF fits were consistently better in all areas except for the early visual areas resulting in an overall significant advantage

bioRxiv preprint doi: https://doi.org/10.1101/2020.09.05.284133; this version posted September 8, 2020. The copyright holder for this preprint (which was not certified by peer review) is the author/funder, who has granted bioRxiv a license to display the preprint in perpetuity. It is made available under aCC-BY-NC 4.0 International license.

across all voxels ($z = -29.79$, $p < 0.0001$). For the U-LIN model the difference between HRFs was not significant for the analysis across all voxels ($z = 0.97$, $p = 0.33$). In all cases however, the effect sizes were very small ($\text{mean}_{(\text{mHRF-dHRF})}$ ± standard deviation, P-LIN: 0.09 ± 1.92%, U-LIN: 0.04 ± 2.01%, CSS: 0.16 ± 1.83%, DoG: -0.11 ± 2.12%) and the estimated pRF sizes and locations were highly comparable across HRFs ($\text{Size}_{(\text{mHRF-dHRF})}$, P-LIN: -0.07 ± 1.10 dva, U-LIN: -0.05 ± 1.68 dva, CSS: -0.19 ± 7.66 dva, DoG: -0.19 ± 1.68 dva; $\text{Eccentricity}_{(\text{mHRF-dHRF})}$, P-LIN: -0.07 ± 2.13 dva, U-LIN: -0.09 ± 2.30 dva, CSS: -0.02 ± 1.93 dva, DoG: -0.08 ± 2.43 dva). For this reason, we only included the results obtained with the faster monkey-specific HRF in post-fit analyses of the MRI results.

The estimated pRF sizes were generally larger for areas higher in the visual cortical hierarchy (Felleman and van Essen, 1991). The well-described positive correlation between RF eccentricity and size (Dumoulin and Wandell, 2008) was evident in the monkey fMRI results for all areas with a substantial number of well-fit voxels and the slope of the eccentricity-size relation was generally larger in higher cortical areas (Figure 5A-C).

The static non-linearity parameter (*n*) that models non-linear spatial summation in the fits with the CSS model was smaller than one in all functional areas (Wilcoxon Signed Rank, one-tailed, all ROI's with more than four voxels $R^2 > 5\%$, $p < 0.001$), indicating the presence of compressive spatial summation (Figure 5D). This is similar to what has previously been demonstrated for human visual cortex (Kay et al., 2013; Winawer et al., 2013). The estimated values of the exponential parameter in early visual cortex of the monkey are comparable to what was previously reported for human V1. However, while values became a lot lower in human extrastriate cortex (indicating stronger spatial compression), they were fairly similar throughout monkey cortex suggesting that spatial compression may be global but less pronounced in monkey visual cortex.

bioRxiv preprint doi: https://doi.org/10.1101/2020.09.05.284133; this version posted September 8, 2020. The copyright holder for this preprint (which was not certified by peer review) is the author/funder, who has granted bioRxiv a license to display the preprint in perpetuity. It is made available under aCC-BY-NC 4.0 International license.

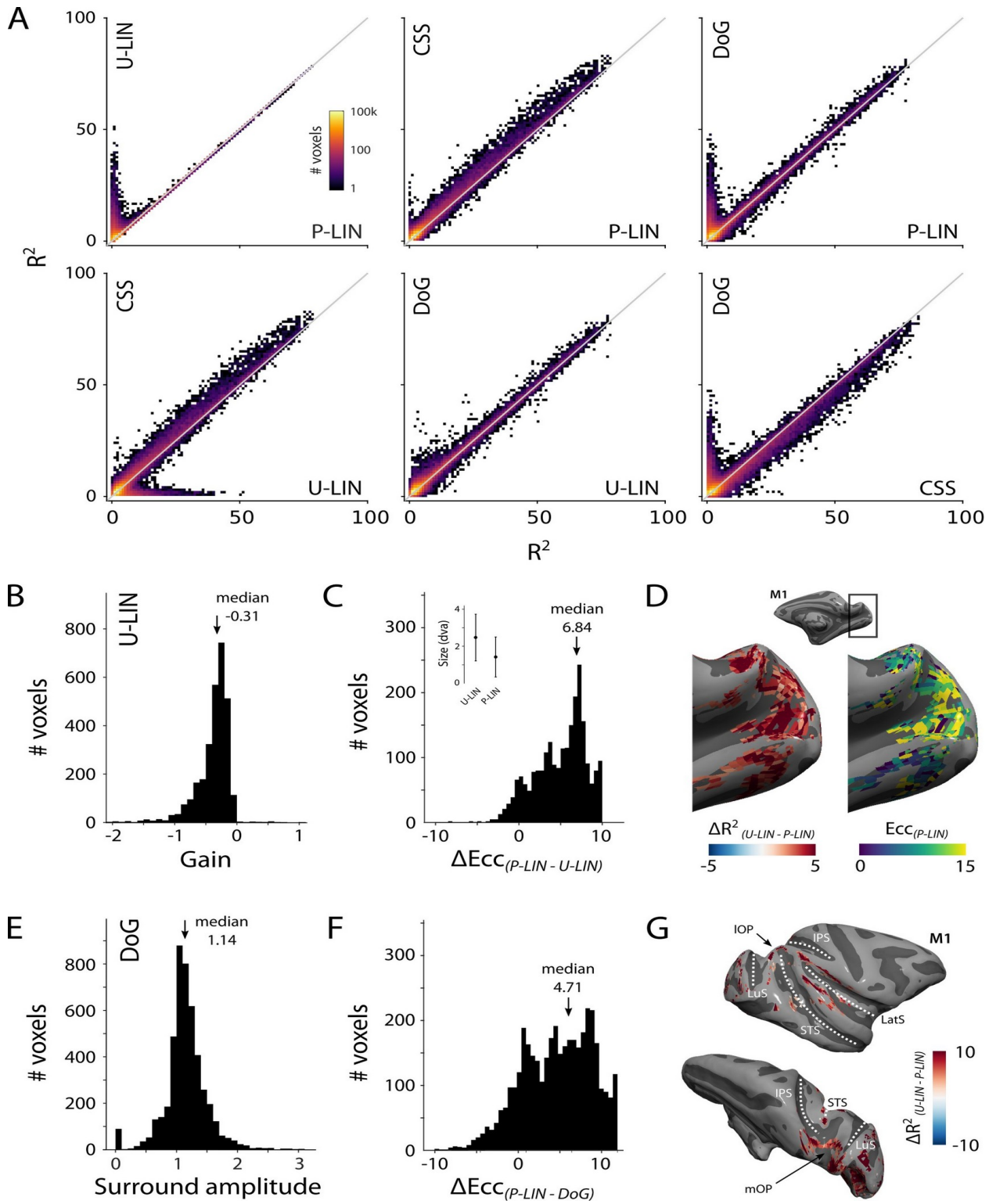

bioRxiv preprint doi: https://doi.org/10.1101/2020.09.05.284133; this version posted September 8, 2020. The copyright holder for this preprint (which was not certified by peer review) is the author/funder, who has granted bioRxiv a license to display the preprint in perpetuity. It is made available under aCC-BY-NC 4.0 International license.

Figure 4. Comparison of MRI-based fit-results from the four pRF models. (A) Binned scatter-plots comparing the fit accuracy across pRF models. Data is binned in two-dimensional R^2 bins of 1% X 1%, with the color-map indicating the number of voxels in each 2D bin. These plots indicate that the CSS model fits the data best across the board while the DoG and U-LIN models give good fits for voxels that are more poorly characterized by the P-LIN and CSS models. **(B)** Distribution of gain values of the U-LIN pRF fits for voxels where the cross-validated R^2 of the U-LIN model was larger than 5% and at least 5% higher than that of the P-LIN model. Negative gain values indicate a negative or suppressed BOLD response (arrow indicates the median, -0.31). **(C)** Distribution of the differences in estimated eccentricity from the U-LIN and P-LIN models for the same voxels as in (B). Positive values indicate that the pRFs estimated by the P-LIN model were more peripherally located than those estimated by the U-LIN model (arrow indicates the median, 6.84 dva). The inset displays the mean (± standard deviation) of the pRF sizes for the U-LIN and P-LIN models. **(D)** One cluster of voxels for which the U-LIN model fit better than the P-LIN model was located in the medial occipital lobe (left panel) where voxels had a high eccentricity for P-LIN pRFs (right panel). **(E)** Distribution of the normalized suppressive surround amplitude values from the DoG pRF fits (*a* in Equation 4 of the Material & Methods section). Values larger than one indicate that the amplitude of the suppressive surround Gaussian is larger than that of the excitatory center (arrow indicates median, 1.14). **(F)** Distribution of the differences in estimated eccentricity from the DoG and P-LIN models for the same voxels as in (E). Positive values indicate that the P-LIN model estimated pRFs to be more peripherally located than the U-LIN model (arrow indicates the median, 4.71 dva). Note that in addition to the peak in the distribution around the radius of the visual stimulus (i.e., 8 dva) that is also present in (C), there is a second peak around zero, indicating that the DoG model also outperforms the P-LIN when it estimates pRFs to be in a highly similar location (see also Supplemental Figure S4). **(G)** Clusters of voxels that were well-captured by the negative pRFs of the U-LIN model but not by the positive pRFs of the P-LIN model were located around the lateral sulcus (LatS), in the medial occipital parietal cortex (mOP), and in the lateral occipital parietal cortex (lOP).

bioRxiv preprint doi: https://doi.org/10.1101/2020.09.05.284133; this version posted September 8, 2020. The copyright holder for this preprint (which was not certified by peer review) is the author/funder, who has granted bioRxiv a license to display the preprint in perpetuity. It is made available under aCC-BY-NC 4.0 International license.

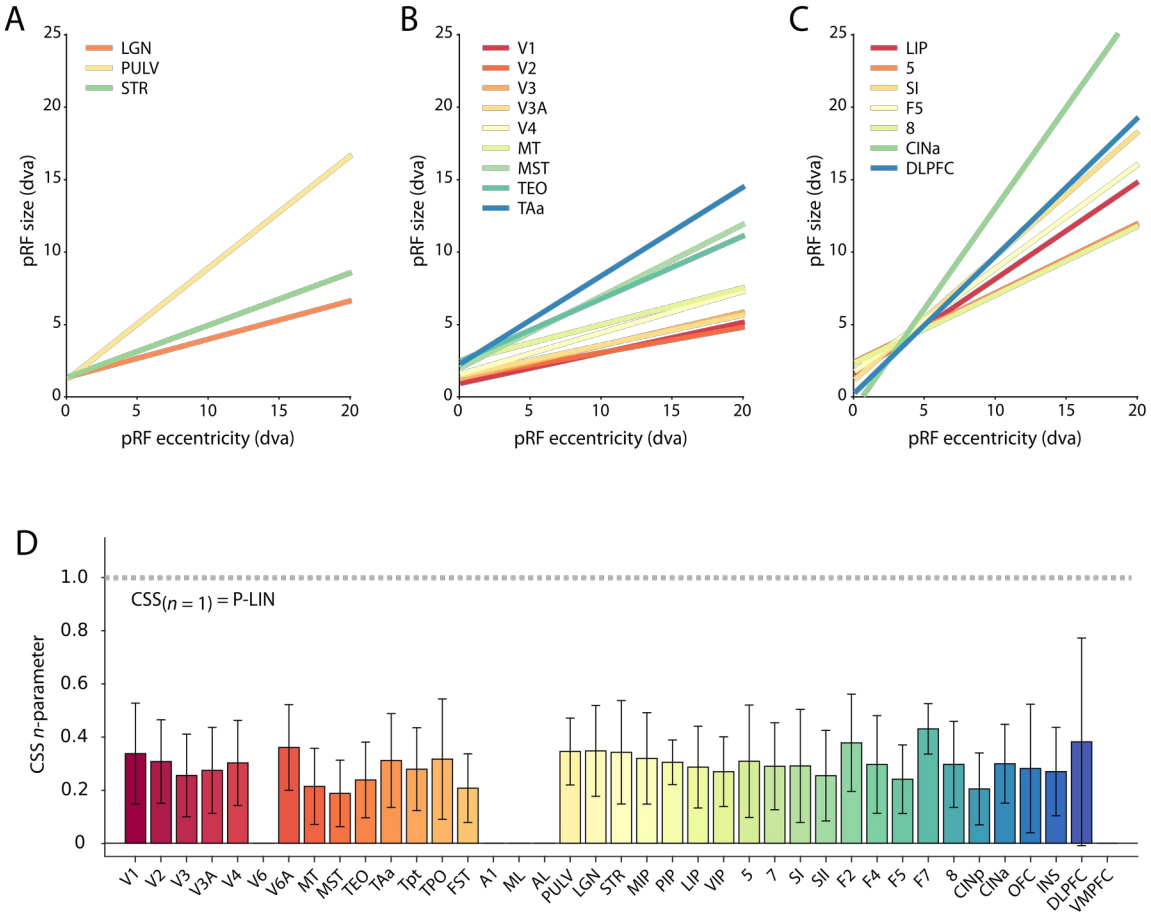

Figure 5. Characterization of pRF estimates from the CSS model. (A) Eccentricity-size relationship for subcortical areas. **(B)** Eccentricity size relationship for early and mid-visual areas in the occipital and temporal lobes. **(C)** Eccentricity size relationship for parietal and frontal cortical areas. Lines in all panels are linear fits with a significant slope ($p < 0.01$). Confidence intervals are omitted in this figure to avoid clutter, but this information can be found in Supplemental Figure S7. Note that some fit lines overlap to a large extent. **(D)** Mean values of the static non-linearity in the CSS model for voxels with $R^2 > 5\%$ per ROI. When the exponential parameter (n) in the CSS equals one, the CSS model is the same as the conventional P-LIN model (dashed gray line). Values lower than one indicate subadditive or compressive spatial summation (Kay et al., 2013). The exponent parameter value was significantly below one for all areas with more than four voxels above the R^2 threshold, but not distinctly different along the visual cortical hierarchy. Error bars indicate the standard deviation.

bioRxiv preprint doi: https://doi.org/10.1101/2020.09.05.284133; this version posted September 8, 2020. The copyright holder for this preprint (which was not certified by peer review) is the author/funder, who has granted bioRxiv a license to display the preprint in perpetuity. It is made available under aCC-BY-NC 4.0 International license.

Multi-unit spiking activity pRFs

The same four pRF models (P-LIN, U-LIN, CSS, and DoG) were also independently fit to the MUA dynamics and the power in five different frequency bands of the LFP. We obtained excellent fits based on the MUA for all pRF models, covering a large proportion of the lower right visual field (Figure 6, Supplemental Figure S8). The locations of estimated pRFs from individual electrodes on the same arrays are clustered in space, with more medial electrode arrays representing a more peripheral region of the visual field. Fit accuracies were generally much higher in terms of the percentage of variance explained for the electrophysiology data compared to the fMRI data.

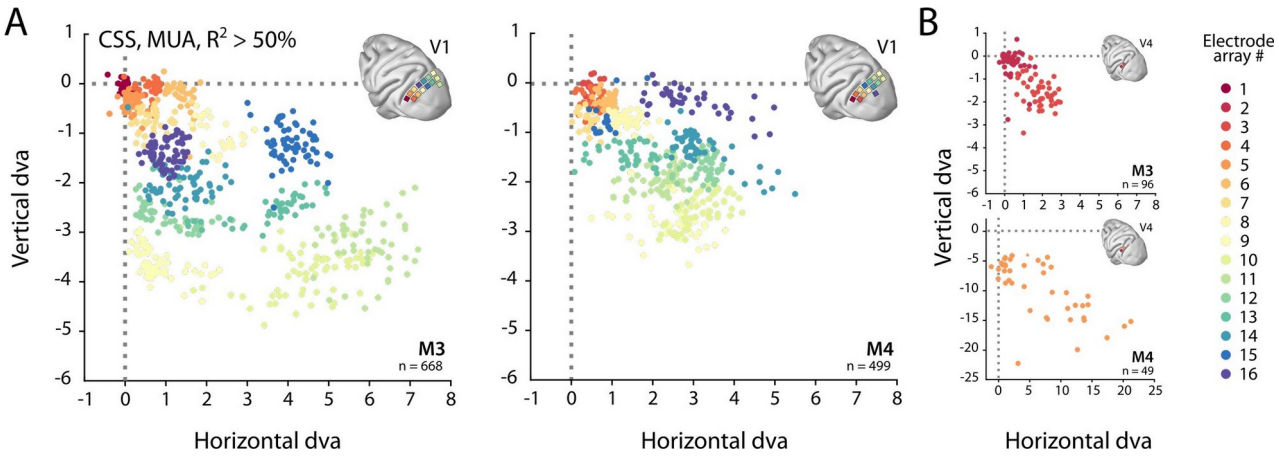

Figure 6. Visual field coverage of pRF from Utah arrays. (A) In both monkeys (M3, M4), most Utah arrays were implanted in the superior part of left V1. The location of MUA-based pRFs are plotted with the individual arrays color-coded. These pRFs represent the lower right visual field. Only electrodes with R^2 > 50% in the CSS model are included in these plots. **(B)** Same as in (A), but for the fewer electrode arrays implanted in V4 of the left hemisphere. Note the different scale in the lower panel. Supplementary Figure S8 plots the same data, but as a heat-map that takes pRF sizes into account.

Cross-validated comparisons of fit accuracy showed significant differences across the models (Kruskal-Wallis test on all four models: $H_{V1} = 204.63$, $df_{V1} = 3$, $p_{V1} < 0.0001$; $H_{V4} = 13.4$, $df_{V4} = 3$, $p_{V4} < 0.01$) (Figure 7). Post-hoc pairwise comparisons (Tukey's HSD) revealed that the CSS and DoG models were generally able to explain a higher percentage of variance than the linear models, although for V4 the advantage of the CSS model over the P-LIN model was only significant when electrodes with a poor fit accuracy (R^2 < 25%) were excluded from the comparison (V1, all electrodes: CSS vs. P-LIN, $p < 0.001$, DoG vs. P-LIN, $p < 0.001$; V4, all electrodes: CSS vs. P-LIN, $p = 0.16$, DoG vs. P-LIN, $p < 0.001$; V1, electrodes with R^2 > 25%: CSS vs. P-LIN, $p < 0.001$, DoG vs. P-LIN, $p < 0.001$; V4, electrodes with R^2 > 25%: CSS vs. P-LIN, $p < 0.02$, DoG vs. P-LIN, $p < 0.01$). When all channels were included, there was no significant difference between the CSS and DoG models (V1: $p = 0.74$; V4: $p = 0.79$) but for V1 electrodes with good pRF fits the CSS model significantly outperformed the DoG model (R^2 > 25%; V1: $p < 0.05$). There were no electrodes for which the U-LIN model showed a clear advantage over the P-LIN model (V1 and V4, $p = 1$), suggesting that there were

bioRxiv preprint doi: https://doi.org/10.1101/2020.09.05.284133; this version posted September 8, 2020. The copyright holder for this preprint (which was not certified by peer review) is the author/funder, who has granted bioRxiv a license to display the preprint in perpetuity. It is made available under aCC-BY-NC 4.0 International license.

no purely negative pRFs in spiking activity for the V1 and V4 regions covered by the electrode arrays. For electrodes where the DoG model performed better than the P-LIN model, both models generally estimated a similar pRF location (Median position difference = 0.56, IQR 0.12 – 1.00 dva), but there was a substantial contribution of the suppressive surround (median normalized suppressive amplitude = 0.71, IQR 0.56 – 0.86).

The exponential parameters (*n*) in the MUA-based fits of the non-linear CSS model were significantly lower than one (R^2 > 25%; mean 0.37 ± std 0.23; Wilcoxon Signed Rank, one-tailed, z = -33.49, p < 0.001), and highly similar to the MRI-based values in V1 (Wilcoxon Rank Sum test, z = 0.30, p = 0.76).

The size of the estimated pRFs generally increased with eccentricity (Figure 12A,B). Notable exceptions to this well-known relationship between the eccentricity and size of visual receptive fields were the pRFs estimated from responses recorded with the V1 electrode arrays located most medially on the occipital surface in both monkeys (Supplemental Figure S9). While the pRF locations for the electrodes on these arrays were as expected based on their cortical location (rather peripheral in the lower contralateral visual hemifield), their sizes were about a factor of three smaller than predicted from the trend in the data from the other arrays. The gray matter of the medial primary visual cortex is thinner than that of lateral V1, and the deviating arrays were physically located in the posterior-medial corner of the craniotomy (Supplemental Figure S9). It is conceivable that closure of the craniotomy may have exerted pressure on the 1.5 mm long shanks of the Utah array electrodes, causing their tips to extend beyond the cortical gray matter into the underlying white matter where they might have picked up signals from thalamic afferents (i.e., the geniculostriate pathway). We decided to exclude the results from electrodes on these arrays from analyses that use pRF size as a variable.

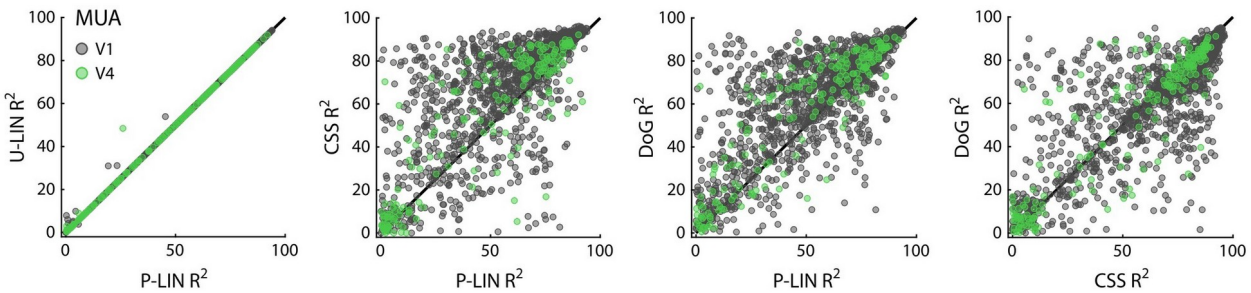

Figure 7. Comparison of MUA-based fit-results from the four pRF models. Scatter-plots comparing the fit accuracy across pRF models. Each dot represents an electrode. Black dots are V1 electrodes, green dots are V4 electrodes.

There was a good correspondence between the MUA-pRFs and the receptive fields (MUA-RF) estimated with our laboratory's standard RF-mapping method for the same electrodes (Supplementary Figure S10). Whenever both methods were able to estimate a (p)RF accurately (R^2 > 25% for pRF method, SNR > 3 for RF method), their estimated locations were highly similar (median distance between CSS-pRF and RF center, V1: 0.40, IQR 0.21 – 0.58 dva; V4: 0.84, IQR 0.11 – 1.57 dva). On average, the classic method estimated slightly

bioRxiv preprint doi: https://doi.org/10.1101/2020.09.05.284133; this version posted September 8, 2020. The copyright holder for this preprint (which was not certified by peer review) is the author/funder, who has granted bioRxiv a license to display the preprint in perpetuity. It is made available under aCC-BY-NC 4.0 International license.

smaller RFs than the pRF method (CSS model, V1: Median size difference = 0.39 dva, IQR 0.19 – 0.59 dva; Wilcoxon Signed Rank $z = 27.17$, $p < 0.001$; V4: Median size difference = 0.75 dva, IQR -0.07 – 1.57 dva; Wilcoxon Signed Rank $z = 9.09$, $p < 0.001$), but since the two methods have different definitions of what constitutes a receptive field size these differences are difficult to interpret.

Local Field Potential pRFs

The local field potential signal (LFP) was split into five frequency bands (LFP-θ: 4-8 Hz; LFP-α: 8-16 Hz; LFP-β: 16-30 Hz; LFP-γ_{low}: 30-60 Hz; LFP-γ_{high}: 60-120 Hz) for which we calculated the power fluctuations over time using a multi-taper approach (Bokil et al., 2010). Each pRF model was independently fit to each LFP frequency band to estimate pRFs. The models differed significantly in their fit accuracy for all LFP components in both V1 and V4 (Kruskal-Wallis test for each LFP component separately, $p < 0.01$), except for LFP- γ_{high} in V4 where there were no such differences ($p = 0.27$). Detailed evaluation of fit accuracy across models for the LFP signals revealed some interesting patterns (Figure 8, Supplementary Figure S11). The higher frequency components (LFP-γ_{low} and LFP-γ_{high}) largely mirrored the MUA results with excellent fit accuracy for a large proportion of the electrodes, especially in V1. For LFP-γ_{low} pRFs, the CSS model outperformed all other models in both V1 and V4 (Tukey's HSD; all $p < 0.01$), except for the DoG model in V4 where the difference did not reach significance ($p = 0.07$). For LFP-γ_{high} pRFs in V1, both the CSS and DoG outperformed the P-LIN and U-LIN model (all $p < 0.001$) with no difference between them ($p = 0.55$). The U-LIN model did not perform any better than the P-LIN model for these higher frequency LFP components (all $p > 0.99$), indicating that there were no negative pRFs observed in the gamma-power dynamics. For some electrodes, the DoG model did a little better than the CSS model for LFP-γ_{low} (Figure 8). While this may weakly suggest the presence of a center-surround structure in LFP-γ_{low} pRFs, the overall fit accuracy remained too low to draw robust conclusions ($R^2 < 25\%$).

This pattern was different for the lower-frequency LFP components. For the lowest frequency band tested (LFP-θ), fit accuracies were generally low, but better for the DoG model than for any of the other models (Tukey's HSD; all $p < 0.01$). For LFP-α and LFP-β, both effects were present. There were advantages of the CSS and DoG models for electrodes with high fit accuracies, as well as advantages of the DoG and U-LIN models for electrodes with poor fits for the positively constrained CSS and P-LIN models. This dispersed pattern of model advantages for the LFP-α and LFP-β suggests that there may be two types of pRF signals captured by this LFP component. The occurrence of negative pRFs in these LFP frequency bands was further investigated by specifically selecting electrodes that had a U-LIN fit accuracy of at least 20% and an advantage of U-LIN over P-LIN of at least 5%. Naturally, these electrodes had significant negative gain values for both LFP-α and LFP-β (LFP-α: median gain = -247.87, IQR = 208.34; Wilcoxon Signed Rank one-tailed ($g < 0$), $z = -10.45$, $p < 0.0001$; LFP-β: median gain = -94.81, IQR = 60.33; Wilcoxon Signed Rank one-tailed ($g < 0$), $z = -10.12$, $p < 0.0001$) (Figure 9A). Comparing the P-LIN and U-LIN locations and sizes of the pRFs for these electrodes revealed that the negative U-LIN pRFs were both smaller (Wilcoxon Signed

bioRxiv preprint doi: https://doi.org/10.1101/2020.09.05.284133; this version posted September 8, 2020. The copyright holder for this preprint (which was not certified by peer review) is the author/funder, who has granted bioRxiv a license to display the preprint in perpetuity. It is made available under aCC-BY-NC 4.0 International license.

Rank; LFP-α: z = -8.20, p < 0.0001; LFP-β: z = -9.78, p < 0.0001) and more foveal (Wilcoxon Signed Rank; LFP-α: z = -10.93, p < 0.0001; LFP-β: z = -10.37, p < 0.0001) than the positive P-LIN pRFs (Figure 9B). Note that this is different from what we observed with fMRI where the negative pRFs were also more foveally located but substantially larger than the positively constrained fits for the same voxels. Electrodes for which the DoG model outperformed the P-LIN in LFP-α and LFP-β ($R^2 > 20$ and 5% better for DoG than for P-LIN) had substantial suppressive surround amplitudes (Amplitude of the suppressive surround for LFP-α: median = -20.79, IQR = 18.06; for LFP-β: median = -8.58, IQR = 6.31) (Figure 9C). They were again much more foveally located than the pRFs estimated by the P-LIN based on the exact same signal (Wilcoxon Signed Rank; LFP-α: z = -15.79, p < 0.0001; LFP-β: z = -17.12, p < 0.0001).

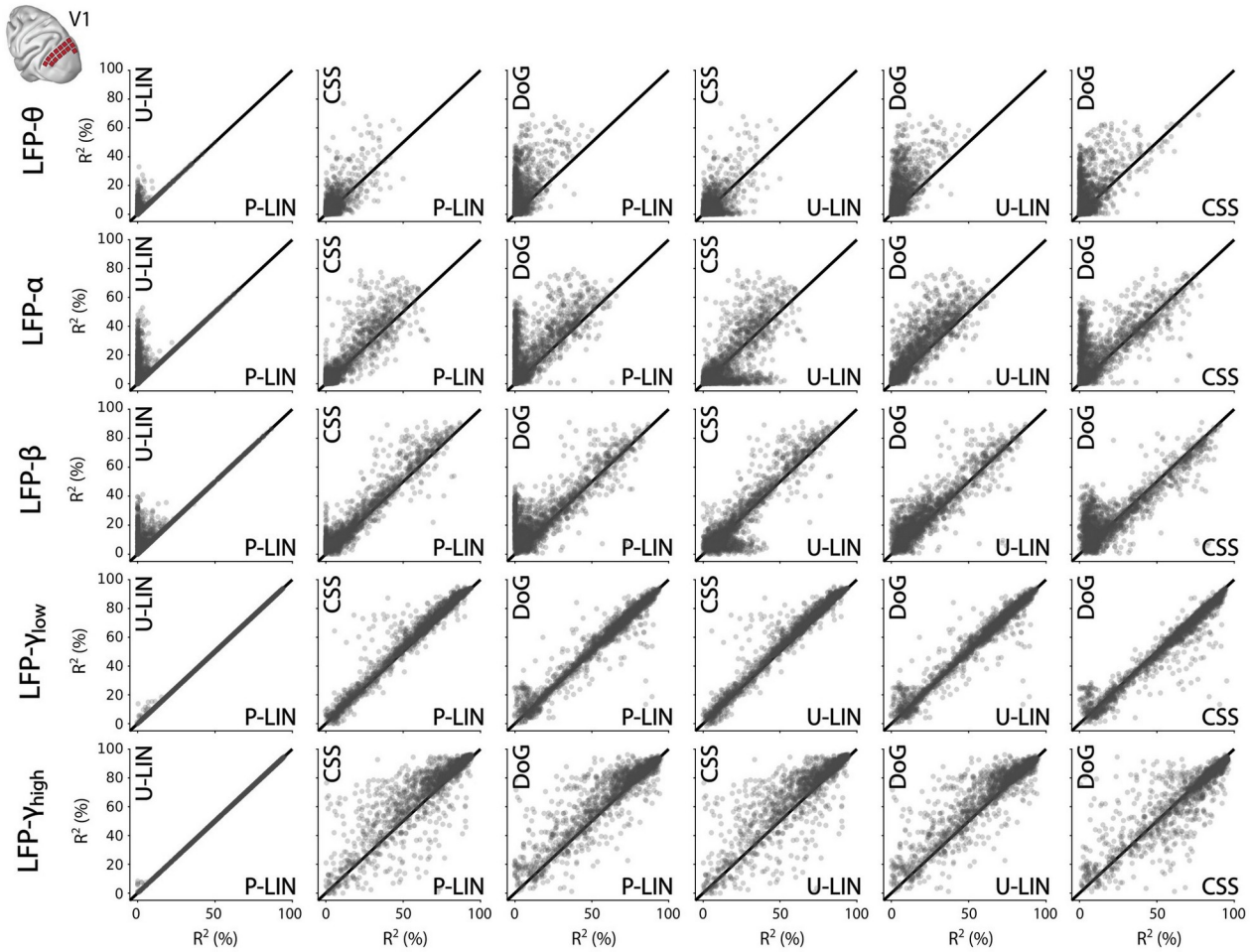

Figure 8. Comparison of LFP-based fit-results from the four pRF models for V1 electrodes. Scatter-plots comparing the fit accuracy across pRF models and LFP frequency bands. Each dot represents an electrode. Note how the pRF models that are able to capture negative responses (DoG, U-LIN) fit better to the lower frequency components of the LFP (α, β). Supplemental Figure S11 shows similar results for the V4 electrodes.

Are the electrodes with good pRF fits based on the MUA the same ones that can be fit well based on the LFP signal? In Figure 10, fit accuracy for the CSS and DoG models are compared across electrophysiological

bioRxiv preprint doi: https://doi.org/10.1101/2020.09.05.284133; this version posted September 8, 2020. The copyright holder for this preprint (which was not certified by peer review) is the author/funder, who has granted bioRxiv a license to display the preprint in perpetuity. It is made available under aCC-BY-NC 4.0 International license.

signals recorded from the same electrode. Fit accuracy values differed significantly across neuronal signals (Kruskal-Wallis, H = 5371.40, df = 5, p = 0). The comparison of R^2 values for each combination of signals is visualized as a two-dimensional scatter-histogram with the color-map indicating how many electrodes fall within a two-dimensional bin of R^2 pairs. Electrodes that fall on the diagonal of the subplots have comparable fit accuracies for the two signal types. For electrodes above the diagonal, fits were better based on the signal on the y-axis, while for electrodes below the diagonal, fit accuracy was higher for the signal on the x-axis. Asterisks in the plot indicate which signal had significantly higher R^2 values. In general, and for both models, pRF fits based on MUA were better when than those based on low frequency LFP components (LFP-θ, LFP-α, LFP-β) and similar to those based on LFP-γ_{low}. Fits based on the LFP-γ_{high} were generally better than those based on any of the other signals. Within the LFP, higher frequency components yielded better fits than lower frequency components, with a smaller difference between LFP-α and LFP-β than between any other signal pair. These patterns were also present in the P-LIN and U-LIN model results (Supplemental Figure S12).

While fit quality differs substantially across electrophysiological signals on the same electrode, the different signals did generally estimate the same pRF location, which in turn aligned well with receptive field locations that were determined with conventional RF-mapping methods for the same electrodes (Shown for the CSS model in Figure 11). Differences in estimated pRF location across signals were generally smaller than one degree visual angle (Figure 11A). Because of the previously demonstrated dissociation between positive and negative pRFs in the low LFP frequencies (LFP-α and LFP-β in particular), we performed a similar analysis on the fits of the U-LIN in which we separated the positive and negative pRFs (Supplemental Figure S13). This analysis showed that the negative low frequency LFP pRFs were generally closer to the MUA and high frequency LFP pRFs on the same electrodes than the positive ones.

In order to compare pRF size across signals while taking into account that pRF sizes will depend on eccentricity as well, we normalized all pRF sizes to the MUA pRF size on the same electrode. Receptive fields determined with conventional RF-mapping methods were smallest (but note that the size definition is also different), while LFP-based pRFs were generally larger than MUA-based pRFs. Within the LFP frequency bands, the low-frequency LFP signals had larger pRFs than the high-frequency LFP signals: LFP-θ and LFP-α pRFs were about a factor two larger than the MUA pRFs, while LFP-γ_{high} pRFs were less than 1.5 times larger than MUA-pRFs. In general though, there was substantial variation in the pRF size relation across signals.

The eccentricity-size relationship that we observed for BOLD-pRFs and MUA-pRFs was also observed for some components of the LFP, but not for all (Figure 12). There were not enough above-threshold electrodes (R^2 > 50%) to estimate the eccentricity-size relationship for LFP-θ. In V1, pRF-sizes estimated by the CSS model increased with eccentricity for LFP-β, LFP-γ_{low}, and LFP-$\gamma_{high,}$ but not for LFP-α (Figure 12A). When the eccentricity-size relationship was determined separately for positive and negative U-LIN pRFs for LFP-α and LFP-β, it became clear that for LFP-α, neither positive nor negative pRFs exhibited a significant eccentricity-size relationship (Supplemental Figure S14). While this relationship was significant for both

bioRxiv preprint doi: https://doi.org/10.1101/2020.09.05.284133; this version posted September 8, 2020. The copyright holder for this preprint (which was not certified by peer review) is the author/funder, who has granted bioRxiv a license to display the preprint in perpetuity. It is made available under aCC-BY-NC 4.0 International license.

positive and negative LFP-β pRFs, the actual slope was negligibly small for the positive pRFs (slope for LFP-β_+: 0.04, $p < 0.01$; slope for LFP-β_-: 0.27, $p < 0.001$). In V4, there were not enough channels with high-quality fits for the low-frequency LFP components to estimate an eccentricity size relationship, but for the LFP-γ_{low} and LFP-γ_{high}, pRF-size consistently increased with eccentricity (Figure 12B).

For the CSS model fits, the exponential parameter that indicates the nature of spatial summation, was significantly below one for all LFP components ($R^2 > 25\%$; Wilcoxon Signed Rank, all $p < 0.0001$). It also increased with LFP frequency, indicating that spatial compression is present in all LFP pRFs but more pronounced in the lower frequency components (Median, IQR; LFP-θ 0.19, 0.15; LFP-α 0.27, 0.21; LFP-β 0.31, 0.19; LFP-γ_{low} 0.34, 0.20; LFP-γ_{high} 0.40, 0.27) (Kruskal-Wallis test across LFP frequency bands, H = 387.97, df = 4, $p < 0.0001$; post-hoc Tukey's HSD multiple comparisons of mean rank showed that the only pairwise comparison that was not significant at $p < 0.05$ was between LFP-θ and LFP-α). Note, that pRF sizes were generally also larger for lower LFP frequencies. Furthermore, all exponential parameter values were furthermore in the same range as the MRI-based values in V1 (Wilcoxon Rank Sum tests; MRI vs. LFP-θ z = 1.61, p = 0.11; MRI vs. LFP-α 0z = 1.07, p = 0.29; MRI vs. LFP-β z = 0.75, p = 0.45; MRI vs. LFP-γ_{low} z = 0.51, p = 0.61; MRI vs. LFP-γ_{high} z = -0.003, p = 0.997).

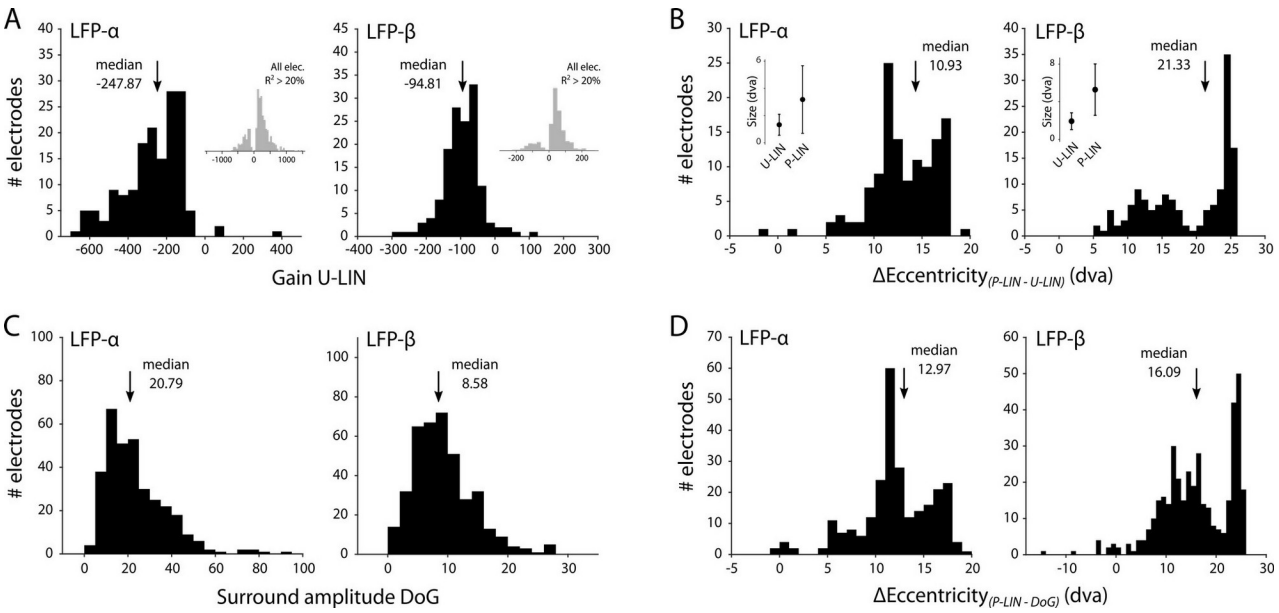

Figure 9. Negative pRFs in low frequency LFP components. (A) Distributions of gain values for the U-LIN model fits of the LFP-α (left panel) and LFP-β (right panel) signals for electrodes that have a fit accuracy of $R^2 > 20\%$ and for which the U-LIN model outperformed the P-LIN model by at least 5%. The gray histogram in the insets show the distribution for all electrodes with only the $R^2 > 20\%$ requirement. **(B)** Histograms of differences in estimated eccentricity from the P-LIN and U-LIN models for the electrodes included in (A). Positive values indicate that the P-LIN model estimated a more eccentric pRF than the U-LIN model. The inset shows the mean pRF size (± std) as estimated by the two models. **(C)** Distributions of normalized suppressive surround amplitude values for the DoG model fits of the LFP-α (left panel) and LFP-β (right panel) signals for electrodes that have a fit accuracy of $R^2 > 20\%$ and for which the DoG model outperformed the P-LIN model by at least 5%. **(D)** Histograms of differences in estimated eccentricity from the P-LIN and DoG models for the electrodes included in (C). Positive values indicate that the P-LIN model estimated a more eccentric pRF than the DoG model.

bioRxiv preprint doi: https://doi.org/10.1101/2020.09.05.284133; this version posted September 8, 2020. The copyright holder for this preprint (which was not certified by peer review) is the author/funder, who has granted bioRxiv a license to display the preprint in perpetuity. It is made available under aCC-BY-NC 4.0 International license.

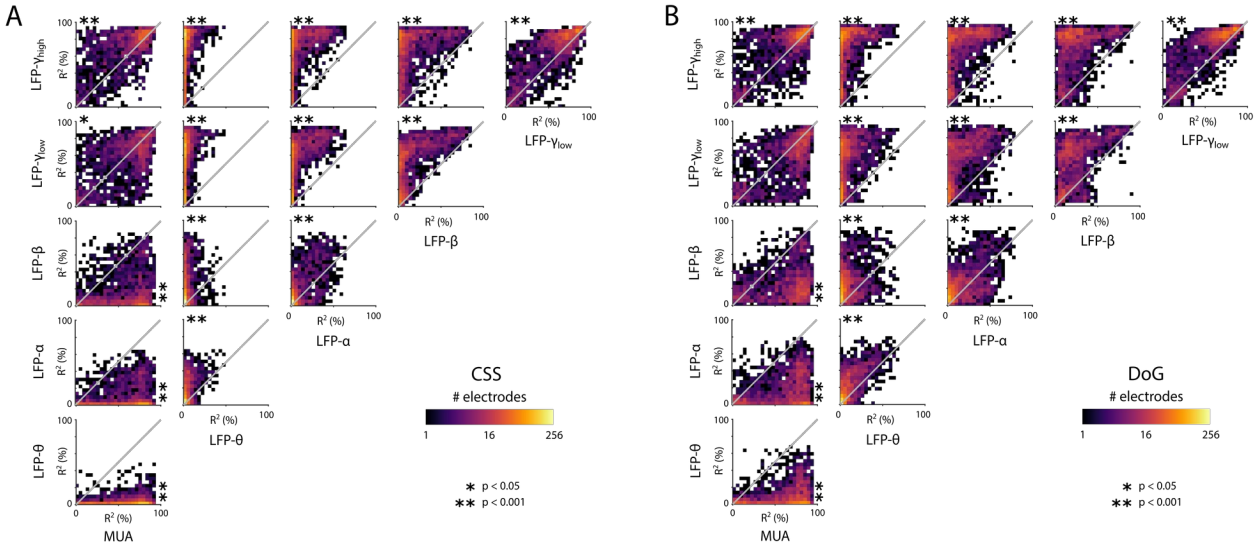

Figure 10. Comparison of pRF fit accuracies for MUA and LFP signals from the same electrodes. (A) Binned scatter plots comparing the R^2 values of pRF fits from the CSS model based on different electrophysiological signals. The gray line indicates similar fit accuracy for the two signals. Colors indicate the number of electrodes in a 4 × 4 % two-dimensional bin (logarithmic scale). Asterisks indicate which of the two signals has significantly higher R^2 values (Kruskal-Wallis, with post-hoc Tukey's HSD multiple comparisons of mean rank, *p < 0.05, **p < 0.001). **(B)** Same as in (A) but for the DoG model. Supplemental Figure S12 shows similar results for the P-LIN and U-LIN models.

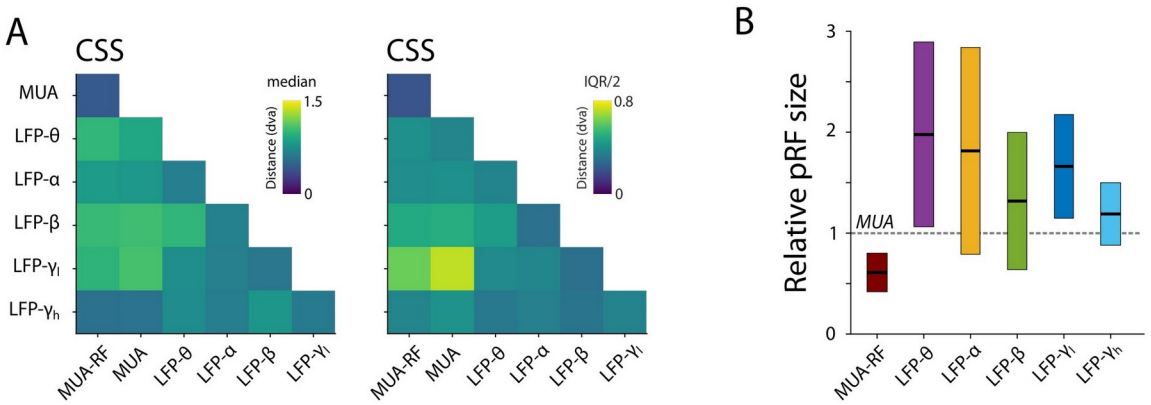

Figure 11. Comparison of pRF location and size from different electrophysiological signals on the same electrode, estimated by the CSS model. (A) Median distance (left) and half the IQR (right). For this comparison electrodes were only included when their pRF fit accuracy R^2 > 25% (MUA, LFP) or the SNR was higher than 3 (MUA-RF). **(B)** Relative pRF size for the same electrode pairs as in (A). For each signal, pRF/RFs were normalized by the MUA-pRF from the same electrode (dashed line). Horizontal lines indicate the median, colored rectangles depict the IQR.

bioRxiv preprint doi: https://doi.org/10.1101/2020.09.05.284133; this version posted September 8, 2020. The copyright holder for this preprint (which was not certified by peer review) is the author/funder, who has granted bioRxiv a license to display the preprint in perpetuity. It is made available under aCC-BY-NC 4.0 International license.

Comparison of pRF eccentricity-size relationship between fMRI and electrophysiology signals

The eccentricity-size relationship of pRFs across the cortex is perhaps an important feature of retinotopic maps. Since we observed this characteristic across all signals for which we modeled pRFs it constitutes an excellent basis to investigate what neuronal tuning profile is best captured by the BOLD-fMRI pRF-maps. We used Linear Mixed Models (LMM) to investigate the effects of pRF eccentricity and signal type on pRF size. Within signal types, a significant effect of eccentricity with a positive slope indicates that pRFs get larger when their location is more eccentric. In a comparison between signals, a significant effect of signal type indicates a difference in pRF size independent of eccentricity, while a significant interaction between signal type and eccentricity implies that the slope between eccentricity and size (i.e., the structure of the pRF-map) is different across signal types. A comparison of the slope across signals can provide a more detailed picture of the nature of this difference.

We first performed this analysis on the results of the CSS model since this model generally performed best for all signal types (inclusion thresholds were $R^2 > 50\%$ for electrophysiology signals and $R^2 > 5\%$ for MRI). Comparisons were done separately for V1 and V4 (voxels and electrodes). In V1, significant eccentricity-size relationships existed for MRI, MUA, LFP-β, LFP-γ_{low}, and LFP-γ_{high} (Figure 12A). All these relationships had positive eccentricity-size slopes. Signals with significant eccentricity-size relationships were further tested in a single LMM that revealed a highly significant interaction effect of Signal Type × Eccentricity ($F = 11.88$, $df = 4$, $p < 0.0001$) indicating that the eccentricity-size slope depends on the type of signal used to estimate the pRFs. We further investigated these differences with pairwise LMM's that compared the MRI-pRFs against each electrophysiological signal with a significant eccentricity-size relationship. This analysis revealed significant interactions between signal type and eccentricity for MRI vs. LFP-β ($F = 10.44$, $df = 1$, $p < 0.01$), LFP-γ_{low} ($F = 23.60$, $df = 1$, $p < 0.001$), and LFP-γ_{high} ($F = 6.66$, $df = 1$, $p < 0.01$), but not for MRI vs. MUA ($F = 0.01$, $df = 1$, $p = 0.92$), providing evidence for the idea that the structure of the BOLD-based pRF map in V1 (or at least the eccentricity-size relationship) is most similar to that of MUA-pRFs (Figure 12C).

This analysis was also performed for V4 (Figure 12B) where we had fewer electrodes. Fit quality for these electrodes was generally low for the low-frequency components of the LFP and as a consequence it was not possible to estimate any eccentricity-size relationships for LFP-θ, LFP-α, and LFP-β. For MUA, LFP-γ_{low}, and LFP-γ_{high} there were significant positive eccentricity-size slopes. The difference across these signals was not as pronounced as for V1 ($F = 2.15$, $df = 3$, $p = 0.09$), but pairwise comparisons of electrophysiology signals with MRI results revealed that there was a significant interaction between signal type and eccentricity for MRI vs. MUA ($F = 5.66$, $df = 1$, $p < 0.02$), but not for MRI vs. LFP-γ_{low} ($F = 0.17$, $df = 1$, $p = 0.68$), or MRI vs. LFP-γ_{high} ($F = 0.03$, $df = 1$, $p = 0.85$).

We already noted that there was a difference in eccentricity-size relationship between positive and negative pRFs of lower frequency LFP-components. To investigate the consequences of this effect for the cross-signal eccentricity-size comparison we also performed the LMM analysis for U-LIN model results with the LFP-θ, LFP-α, and LFP-β pRFs separated into positive and negative pRF subgroups (lowering the electrode inclusion

bioRxiv preprint doi: https://doi.org/10.1101/2020.09.05.284133; this version posted September 8, 2020. The copyright holder for this preprint (which was not certified by peer review) is the author/funder, who has granted bioRxiv a license to display the preprint in perpetuity. It is made available under aCC-BY-NC 4.0 International license.

criterion to $R^2 > 25\%$ to allow the relevant data to be included) (Supplemental Figure S14). While the fit accuracy did not meet the inclusion threshold in the V4 electrodes, there was a substantial number of V1 electrodes for both the positive and negative pRF subgroups (LFP-α: $n_+ = 354$, $n_- = 89$; LFP-β: $n_+ = 535$, $n_- = 45$). In the case of LFP-α, there was no significant eccentricity-size relationship in either the positive ($t = 1.01$, $p = 0.31$), the negative ($t = 1.00$, $p = 0.32$), or the full set of U-LIN pRFs ($t = -0.54$, $p = 0.59$). For LFP-β, such a significant relationship did exist for both positive ($t = 3.60$, $p < 0.001$) and negative ($t = 3.89$, $p < 0.001$) pRFs separately, but not for the combined group ($t = 1.03$, $p = 0.30$). Furthermore, for the positive pRFs subgroup, the slope was negligibly low (0.04, 95% CI 0.02-0.05) and significantly different from the slope in the corresponding MRI data ($F = 37.49$, $df = 1$, $p < 0.0001$). The negative LFP-β pRFs had a more substantial slope (0.27, 95% CI 0.13-0.41) and due to a rather large confidence interval, this slope did not significantly differ from the MRI-based slope ($F = 0.30$, $df = 1$, $p = 0.58$). However, similar to the CSS results, the MUA-based pRF slopes from the U-LIN model (with a much smaller 95% CI: 0.12-0.22) did also not significantly differ from the MRI-based slopes ($F = 0.83$, $df = 1$, $p = 0.36$). In V4, again similar to the CSS results, MUA-based eccentricity-size slopes did differ from MRI-based slopes ($F = 9.98$, $df = 1$, $p < 0.01$), which were instead similar to the LFP-γ slopes (LFP-γ_{low}: $F = 1.49$, $df = 1$, $p = 0.22$; LFP-γ_{high}: $F = 2.02$, $df = 1$, $p = 0.16$).

bioRxiv preprint doi: https://doi.org/10.1101/2020.09.05.284133; this version posted September 8, 2020. The copyright holder for this preprint (which was not certified by peer review) is the author/funder, who has granted bioRxiv a license to display the preprint in perpetuity. It is made available under aCC-BY-NC 4.0 International license.

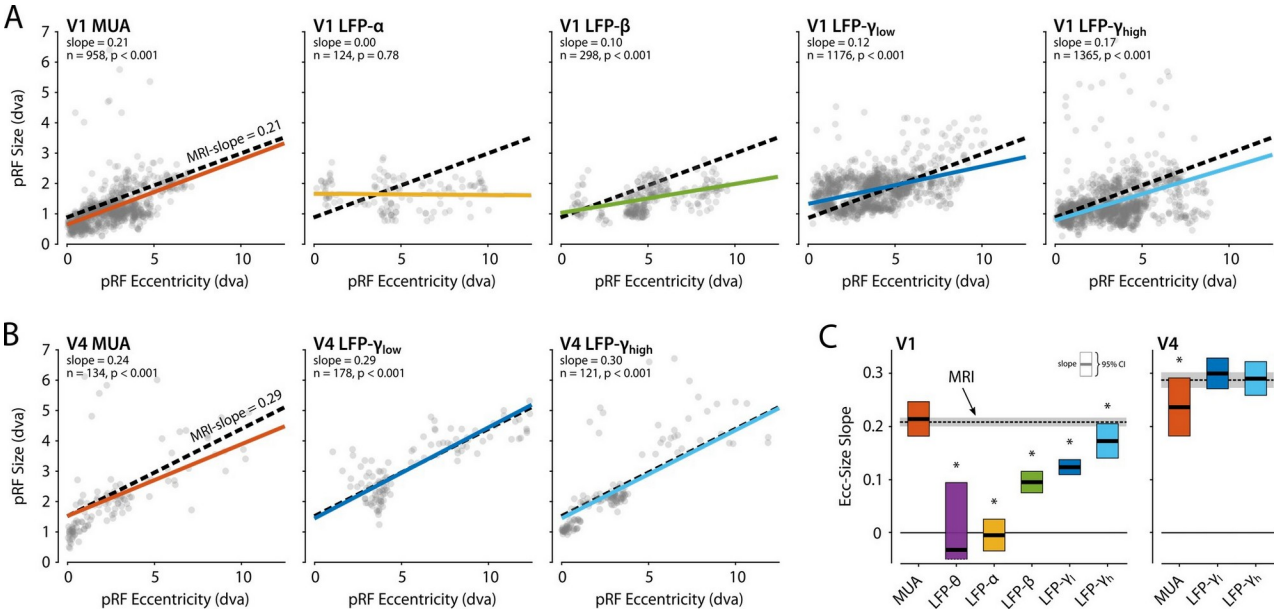

Figure 12. Eccentricity-size relationship for pRF based on different types of neural activity. (A) The pRF size as a function of pRF eccentricity for V1 electrodes where the CSS model had a fit accuracy of R^2 > 50%. Panels represent the different electrophysiological signals that were independently used to fit the pRF model. Dots are individual electrodes, colored lines represent the slope of the eccentricity-size relationship, and the dashed black line represents the same relationship for V1 voxels with R2 > 5%. Only the signal types with > 25 electrodes meeting the R^2 threshold are shown. **(B)** Same as in (A), but now for the V4 electrodes. **(C)** Comparison of the eccentricity-size slope across neural signals (left: V1, right: V4). The dashed line represents the slope for MRI-based pRF with the 95% confidence interval depicted as the gray area. Colored rectangles indicate the 95% confidence intervals for the different electrophysiological signals, with the horizontal black line indicating the slope estimate. Note that the lower bound of the LFP-θ extends beyond what is displayed (there were only a few electrodes with good LFP-θ pRF fits). Asterisks indicate a significant interaction between signal type and eccentricity from a linear mixed model comparing the eccentricity size relationship of MRI-based pRFs with each electrophysiological signal (i.e., the absence of such interaction indicates that there is no evidence for a difference in slope between the electrophysiological signal and the MRI-based pRFs). LFP-θ: 4-8 Hz; LFP-α: 8-16 Hz; LFP-β: 16-30 Hz; LFP-γ_l: 30-60 Hz; LFP-γ_h: 60-120 Hz.

bioRxiv preprint doi: https://doi.org/10.1101/2020.09.05.284133; this version posted September 8, 2020. The copyright holder for this preprint (which was not certified by peer review) is the author/funder, who has granted bioRxiv a license to display the preprint in perpetuity. It is made available under aCC-BY-NC 4.0 International license.

Discussion

The population receptive field (pRF) mapping technique (Dumoulin and Wandell, 2008) has rapidly become a popular method in human neuroimaging, allowing a relatively fast characterization of the retinotopic organization of the brain. Furthermore, since it describes the tuning properties of the underlying voxels, it can also provide insight into more complex visual and cognitive functions (Binda et al., 2018; Ekman et al., 2020; Harvey et al., 2020, 2015; He et al., 2019; Hughes et al., 2019; Mo et al., 2017; Poltoratski et al., 2019; Poltoratski and Tong, 2020; Shao et al., 2013; Shen et al., 2020; Silson et al., 2018; Stoll et al., 2020; Thomas et al., 2015; Welbourne et al., 2018; Zuiderbaan et al., 2017), dysfunctions (Ahmadi et al., 2020; Alvarez et al., 2020; Best et al., 2019; Dumoulin and Knapen, 2018; Green et al., 2019; Schwarzkopf et al., 2014), brain development (Dekker et al., 2019), cortical evolution (Zhu and Vanduffel, 2019), and information transfer across different brain areas (Haak et al., 2013). Human pRFs from neuroimaging studies qualitatively resemble receptive fields recorded with invasive electrophysiological techniques in animal experiments, but since these signals are derived from different species, often with different analytical or experimental methods, it remains an important question what type of neuronal population characteristic is actually measured by the fMRI BOLD-signal (Dumoulin and Wandell, 2008). In the few pRF studies that did have access to human intracranial recordings (Harvey et al., 2013; Winawer et al., 2013), there tended to be a rather low number of surface electrodes (EcoG, or intracranial EEG) that can only measure the local field potential, not spiking activity. Nevertheless, pRFs could be derived from broadband LFP signals, and they exhibited similar spatial summation characteristics as the BOLD signal pRFs (Winawer et al., 2013). A direct comparison of BOLD-based pRFs and electrophysiologically recorded receptive fields has been performed on a small scale in monkeys in the context of validating a new approach that allows estimation of average single-neuron receptive fields within a voxel (Keliris et al., 2019). In this study, only the MUA activity from the electrophysiological recording was used, since its explicit goal was to get estimates from the smallest possible neuronal population.

The current study investigated the neuronal basis of population receptive fields using fMRI and large-scale electrophysiological recordings in awake behaving macaque monkeys. Within the same species, we fit four different pRF models to seven different signal types (BOLD, MUA, and the power in five distinct frequency bands of the local field potential) to gain unique insight into the neuronal basis of pRF measurements in nneuroimaging (Wandell and Winawer, 2015). The original and perhaps still most broadly used pRF model was constrained to positive responses and assumed linear spatial summation (Dumoulin and Wandell, 2008). We labeled this model P-LIN (Positive-LINear) to contrast it with a version in which we removed the positive response constraint to allow for negative pRFs (corresponding to stimulus-driven suppression or reductions of activity) (U-LIN, Unconstrained-LINear). Such negative visual BOLD responses have been reported in human visual cortex (Smith et al., 2004) and the broader default mode network (Szinte and Knapen, 2019). The other two models that we tested were the Difference-of-Gaussians model (DoG) designed to capture the possible center-surround structure of a pRF through the addition of a suppressive surround Gaussian (Zuiderbaan et al., 2012), and the 'compressive spatial summation' model (CSS) that adds a static non-linearity to the P-LIN

bioRxiv preprint doi: https://doi.org/10.1101/2020.09.05.284133; this version posted September 8, 2020. The copyright holder for this preprint (which was not certified by peer review) is the author/funder, who has granted bioRxiv a license to display the preprint in perpetuity. It is made available under aCC-BY-NC 4.0 International license.

model to account for non-linear spatial summation (Kay et al., 2013). This non-linearity was experimentally shown to consistently describe sub-additive spatial summation in humans, hence the 'compressive spatial summation' attribution in its name. All models were fit in a cross-validated manner to avoid over-fitting and allow comparison of fit accuracy across models with different numbers of parameters.

Cortical and subcortical retinotopic tuning of the BOLD signal

We found retinotopic information in a range of brain areas, both subcortical and cortical, spanning occipital, temporal, parietal, and frontal regions. Fit accuracy was far superior in occipital and temporal cortex compared to other areas. Lower accuracy in subcortical areas is likely due to the fact that the types of surface coils commonly used in non-human primate imaging exhibit a substantial drop in signal-to-noise ratio deeper in the brain. Nonetheless, known subcortical visual areas such as the lateral geniculate nucleus (LGN) and pulvinar could be clearly delineated from their surrounding areas based on their higher fit accuracy. In humans, subcortical retinotopic maps have been demonstrated in LGN, pulvinar, superior colliculus (SC), thalamic reticular nucleus (TRN), and substantia nigra (SN) (Cotton and Smith, 2007; DeSimone et al., 2015; Schneider et al., 2004). In our monkey data, we did observe some voxels with above-thresholds fits extending both laterally and medially beyond the pulvinar. While these voxels could, theoretically, represent retinotopic information from the TRN and SC respectively, they were too few to constitute true retinotopic maps and it was difficult to assign them to specific subcortical nuclei with certainty. In a more targeted investigation of subcortical retinotopic maps with fMRI in non-human primates, additional anatomical imaging would be necessary for detailed individual segmentation of the thalamus (DeSimone et al., 2015; Tani et al., 2011). It is perhaps also possible to significantly increase the SNR in these areas by using implanted coils instead of the more conventional external surface coils (Janssens et al., 2012). Both approaches are, however, beyond the scope of the current study.

It is interesting to note that we also observed subcortical retinotopic maps in the head of the caudate nucleus in the striatum. Neurons in the head of the caudate have long been known to play a role in processing visual information in a reward-related context (Hikosaka et al., 1989a, 1989b; Kim and Hikosaka, 2013; Rolls et al., 1983). The head of the caudate receives projections from the thalamus, temporal cortex, prefrontal cortex and cingulate cortex (Griggs et al., 2017) and plays a role in the updating of stimulus-reward associations (Ghazizadeh et al., 2018; Vanduffel, 2018). Although the moving bar stimulus used to estimate pRFs had no predictive value for reward delivery (the animals received juice reward for maintaining fixation), they were presented in a reward-related context, which may have been enough for them to show up in our results. The apparent ipsilateral visual tuning of the more posterior putamen is a bit more puzzling. Although neurons in this area do sometimes respond to ipsilateral visual information, they typically respond more strongly to contralateral stimuli (Kunimatsu et al., 2018). The visual tuning of the unilateral, right-sided, nucleus accumbens (NAc) to visual stimuli in the lower right visual field (ipsilateral) is similarly surprising. Anecdotally, in a deep brain stimulation (DBS) study on addiction, where intracranial EEG activity from the

bioRxiv preprint doi: https://doi.org/10.1101/2020.09.05.284133; this version posted September 8, 2020. The copyright holder for this preprint (which was not certified by peer review) is the author/funder, who has granted bioRxiv a license to display the preprint in perpetuity. It is made available under aCC-BY-NC 4.0 International license.

NAc was recorded in response to symptom-provoking visual stimuli, the right NAc responded more strongly than the left NAc (Valencia-Alfonso et al., 2012). Perhaps the right-sided NAc responds more strongly to visual stimulation in general, but this still would not explain the specificity of its tuning to ipsilateral stimuli. Another potential factor is the location of the reward through which fluid rewards were delivered. This tube was located on the lower right side of the monkey's head, which coincides with the location the NAc appeared to be sensitive for. However, since reward delivery was independent of the location of the pRF mapping stimulus it remains unclear how this could lead to a unilateral tuned response of the NAc.

The occipital, temporal and parietal cortical areas with good pRF fits were generally areas for which retinotopic organization has previously been shown in monkey imaging studies with phase-encoded retinotopic mapping (Arcaro et al., 2011; Janssens et al., 2014; Kolster et al., 2014, 2010, 2009; Patel et al., 2010). While our moving checkerboard stimuli are not ideally suited to investigate visual tuning of frontal areas that are more strongly driven by complex visual stimuli (Janssens et al., 2014; Saygin and Sereno, 2008), there was still a substantial number of voxels with above-threshold fit accuracies in several frontal areas, including the insula, cingulate cortex, frontal eye fields (FEF, area 8), orbitofrontal cortex, ventromedial prefrontal cortex, and dorsolateral prefrontal cortex. These are all areas involved in visual processing and visual attention.

We did not observe any robust retinotopic tuning in the cerebellum. A recent analysis of the extensive Human Connectome Project (HCP) dataset of population receptive fields mapped with 7T fMRI (Benson et al., 2018) revealed comprehensive visual organization of the cerebellum (van Es et al., 2019). While this study reproduced these results with high-powered single-subject experiments at 7T, a combination of lower field strength, coil placement and animals being in the sphinx position likely reduced the SNR in the monkey cerebellum to a level where we could not pick up on such an organization. With monkeys in a more optimal position (e.g., sitting upright in a vertical scanner) and coils specifically designed or placed to target the cerebellum, it may however be possible to investigate the retinotopic organization of the cerebellum in non-human primates as well.

Negative pRFs

Both the U-LIN and DoG pRF models can capture negative pRF components but in very different ways. The U-LIN is a single-Gaussian model that only differs from the original linear pRF model (P-LIN; Dumoulin and Wandell, 2008) in that it does not constrain the 'gain' parameter to positive values. This means that for voxels or electrodes where the U-LIN more accurately fits the neural dynamics than the P-LIN model, the tuning of the underlying neural substrate is negatively related to the location of a visual stimulus, i.e. the signal magnitude decreases in a spatially selective way. This does not necessarily mean that for the same voxel or electrode, a positive relation cannot also be fit with reasonably good accuracy. In that case, however, it is likely that the features of the resulting pRFs will be very different. Both scenarios were observed in the monkey fMRI data, but in very different parts of the brain. In visual cortex we find voxels with small

bioRxiv preprint doi: https://doi.org/10.1101/2020.09.05.284133; this version posted September 8, 2020. The copyright holder for this preprint (which was not certified by peer review) is the author/funder, who has granted bioRxiv a license to display the preprint in perpetuity. It is made available under aCC-BY-NC 4.0 International license.

positively tuned pRFs for peripheral stimulus locations that stretch beyond the eccentricities at which our stimulus was presented and larger negatively tuned pRFs at foveal locations. This pattern is in line with the previously demonstrated notion that visual stimuli can simultaneously cause positive and negative BOLD responses at different cortical locations (Smith et al., 2004). A study with simultaneous electrophysiological recordings and fMRI in anesthetized monkeys showed that negative BOLD responses are related to suppression of neuronal broadband and spiking activity below baseline by stimulation outside the 'positive aggregate receptive field' (Shmuel et al., 2006). The higher accuracy for negative pRFs likely results from the fact that the centers of the peripheral positive pRFs are never stimulated by the mapping stimulus resulting in relatively low positive fit accuracy. We did not find any subgroups of electrodes for which the MUA or high frequency LFP components (LFP-γ_{low}, LFP-γ_{high}) were better explained by negative pRFs (U-LIN) than by positive pRFs (P-LIN). Such electrodes were however clearly present for the lower frequency bands of the LFP (LFP-θ, LFP-α, LFP-β). The negative pRFs in the LFP are different from those based on the BOLD signal, in that they were in fact a lot smaller than their positively constrained counterparts from the same electrodes. This matches a neural mechanism in which low frequency LFP power and spiking activity are negatively correlated and low frequency oscillations play a role in suppressing stimulus-driven spiking (Haegens et al., 2011; Harvey et al., 2013). In a previous human iEEG study with only a few electrodes, this was the only type of LFP-α dynamics in V1 (Harvey et al., 2013). The LFP-α power in the intraparietal sulcus (IPS) on the other hand did not show any spatial tuning. Instead, it decreased in power relative to baseline during visual stimulation. This led the authors to suggest that alpha oscillations may subserve different mechanisms in V1 and IPS. In our current study, we did not have any electrodes in IPS, but the number of electrodes in V1 was one or two orders of magnitude larger than in previous human iEEG study. Not all low frequency LFP signals were better fit with negative pRFs than positive ones. In fact, there were many more electrodes for which positive pRFs could be fit more accurately than negative pRFs. However, there were clear qualitative differences between the positive and negative low-frequency LFP pRFs. The centers of negative pRFs were closer to the MUA-based pRFs on the same electrodes, and their sizes increased with eccentricity, a relationship that was absent in positive pRFs. While negative responses thus seem to be in line with a role of the low frequency LFP components in suppression of spiking, the overall role of slow oscillatory LFP signals in visual information processing in V1 appears to be more diverse and complex.

The DoG model also captures negative pRF components but instead of modeling a single Gaussian with a free gain parameter, it explicitly models the pRF as a combination of two Gaussians. A central positive Gaussian (the same as P-LIN pRFs) is combined with a negative 'surround' Gaussian that has the same center location as the positive Gaussian and is constrained to be larger. The relative amplitudes of the positive and negative Gaussians can vary freely. At one end of the spectrum, where positive amplitudes are much larger than negative amplitudes, the model's pRFs are very similar to those of the P-LIN model. At the other end, where negative amplitudes are much larger than positive ones DoG pRFs resemble U-LIN pRFs. In between these two extremes, pRFs can capture a range of center-surround pRFs with both a central positive and surrounding negative component. As a result, the DoG model captures the same negative pRF phenomena described

bioRxiv preprint doi: https://doi.org/10.1101/2020.09.05.284133; this version posted September 8, 2020. The copyright holder for this preprint (which was not certified by peer review) is the author/funder, who has granted bioRxiv a license to display the preprint in perpetuity. It is made available under aCC-BY-NC 4.0 International license.

above, but it additionally reveals which signals and brain areas are more accurately described in center-surround terms. In the MRI-based pRFs, advantages of the DoG model were primarily found in early visual cortex, which is similar to previous results in humans (Zuiderbaan et al., 2012). In the electrophysiology data, there was a large advantage of the DoG model over both P-LIN and U-LIN in the MUA-based pRF fits, consistent with pronounced center-surround effects in spike-based receptive fields (Allman et al., 1985; Cavanaugh et al., 2002; Hubel and Wiesel, 1968; Knierim and van Essen, 1992). A similar advantage was present in all LFP components except for LFP-γ_{low}. It is not immediately clear why the center-surround organization of pRFs would be so much weaker or even absent in LFP-γ_{low}. The LFP signal in this frequency band is thought to reflect combined local inhibitory and excitatory synaptic processes (Buzsáki and Wang, 2012). Perhaps the excitatory and inhibitory synaptic processes either cancel out or manifest similarly in the power of the LFP-γ_{low} signal. Detailed investigation of synaptic activity would be required to gain more insight into this mechanism.

There were also voxels for which the BOLD dynamics could be fit well with a negative pRF (U-LIN or DoG), but not at all with a positive pRF (P-LIN), suggesting exclusively tuned suppression of activity by the visual stimulus. These voxels were not located in visual cortex. Instead, we found them in areas reminiscent of the default mode network (DMN) (Mantini et al., 2011). A recent analysis of the HCP retinotopy dataset complemented with extensive single-subject analysis at 7T reported negative pRFs in the human default mode network as well, specifically in the angular gyrus, medial parietal area, lateral temporal area, and the superior medial frontal area (Szinte and Knapen, 2019). While our monkey imaging results likely lacks the power to detect such patterns in the most frontal parts of the brain we did observe purely negative pRFs around the lateral sulcus, in the medial occipital parietal cortex and at the superior border of the superior temporal sulcus in the lateral occipital parietal cortex, all areas that have previously been implicated in the monkey's DMN (Mantini et al., 2011). Unfortunately, we did not have any electrodes located in these areas to investigate the electrophysiological nature of negative visual tuning in the DMN, but the similarity between human and monkey findings suggests a general sensory-based organization of the DMN that might facilitate the DMN's role in coordinating cognitive functions (e.g., Arsenault et al., 2018).

Spatial summation

The CSS pRF model was first introduced to account for non-linear spatial summation of driving visual stimuli across a receptive field (Kay et al., 2013). Subadditive spatial summation (spatial compression) was found throughout the human visual cortex in BOLD-based pRFs, with more anterior areas showing stronger compression than V1. In the monkey MRI data spatial compression was present in all areas with good CSS-pRF fits, both subcortically and cortically, and similar in strength to compression in human V1 (Kay et al., 2013; Winawer et al., 2013) suggesting that subadditive spatial summation is a universal characteristic of the primate visual system. The strength of compression did not differ much across areas, but in early visual areas it tended to be slightly weaker in V1 compared to V2, V3, and V4. In human iEEG recordings, spatial

bioRxiv preprint doi: https://doi.org/10.1101/2020.09.05.284133; this version posted September 8, 2020. The copyright holder for this preprint (which was not certified by peer review) is the author/funder, who has granted bioRxiv a license to display the preprint in perpetuity. It is made available under aCC-BY-NC 4.0 International license.

compression of similar strength of that in the BOLD signal was observed in the broadband iEEG signal, but not in narrow-band power increases related to synchronization of the iEEG signal with a periodically flickering visual stimulus (Winawer et al., 2013). The moving checkerboard in our pRF mapping bar caused local luminance changes at a frequency well below the Theta-band making it unlikely that any component of our LFP signal would become strongly locked to the stimulus. Furthermore, we observed spatial compression in both the MUA-pRFs and in all frequency bands of the LFP. The strength of spatial compression in V1 was highly comparable for BOLD, MUA and LFP, but within the LFP signals it tended to be stronger for lower-frequency components. This could be due to the larger pRF that were typically fit to these low-frequency signals and/or reflect the larger spatial reach of lower-frequency components of the LFP (Łęski et al., 2013).

The neuronal nature of BOLD-based pRFs

What type of neuronal signal is captured by the BOLD-based pRFs? We compared pRF-map structure across signal types in terms of their eccentricity-size relationship, a prominent feature of retinotopic maps (Amano et al., 2009; Dumoulin and Wandell, 2008; Felleman and Van Essen, 1987; Gattass et al., 2005; Kay et al., 2013; Larsson and Heeger, 2006; Van Essen et al., 1984; Victor et al., 1994). We observed a positive correlation between pRF eccentricity and pRF size in the BOLD signal of all cortical and subcortical areas with significant retinotopic information. The slope of this relationship was generally larger for areas higher in the visual cortical hierarchy. Subcortically, the slope for pRFs in the pulvinar was much larger than for those in the LGN. In fact, the slope in the LGN was similar to that of early visual areas, while that of the pulvinar resembled parietal areas such as LIP, and frontal areas such as area 8 (including FEF). This is consistent with both the cortical connectivity pattern of the pulvinar and its role in the regulation of visual attention (Fiebelkorn et al., 2019; Fiebelkorn and Kastner, 2019; Halassa and Kastner, 2017; Saalmann et al., 2012).

Positive eccentricity-size correlations were present in the MUA and LFP-γ signals of both V1 and V4, with steeper slopes in V4 for all these signals. In V1, this relationship also existed for negative LFP-β pRFs. We compared the eccentricity-size relationship in the different electrophysiology signals with the eccentricity-size relationship in MRI data for V1 and V4 to reveal which neuronal signal was most similar to what is measured with BOLD-fMRI. This cross-signal analysis shows that this depends on the brain area of interest, or more specifically, on the heterogeneity of the neuronal population occupying the volume of a voxel. In V1, where retinotopic maps are large in terms of cortical surface area and neurons captured by a single voxel are presumably rather homogeneous in terms of their spatial tuning, the BOLD-based pRF map structure resembled the MUA-based maps most. In V4, that has a smaller surface area than V1, the BOLD-based pRF-map structure was instead more similar to the electrophysiological pRF-map structure based on the gamma power of the LFP. A voxel in V4 will sample a neuronal population with much more heterogeneous spatial tuning profile than an equally sized voxel in V1. As a result, the BOLD signal tuning will thus likely resemble neuronal signals derived from larger population of neurons (i.e., the LFP). This may be a constraint of both the voxel size and the relatively poorly understood neurovascular coupling mechanism that links neuronal

bioRxiv preprint doi: https://doi.org/10.1101/2020.09.05.284133; this version posted September 8, 2020. The copyright holder for this preprint (which was not certified by peer review) is the author/funder, who has granted bioRxiv a license to display the preprint in perpetuity. It is made available under aCC-BY-NC 4.0 International license.

activity to BOLD activity. While advances in imaging sequences, coil design, and field strength may increase the feasibility of neuroimaging at higher spatiotemporal resolutions, the real limit on the size of the neuronal population signal that can be measured with fMRI may very well be partially determined by the biophysical transfer from neuronal to BOLD signals (Goense et al., 2016).

Choice of pRF modeling approach

In the current study, we extensively compared pRF estimates for a range of neural signals across several pRF models. Upon its introduction, the original pRF modeling method (Dumoulin and Wandell, 2008) offered significant advantages over the phase-encoded retinotopic mapping methods that were common at the time (Sereno et al., 1995; Wandell et al., 2007). In the years since this seminal publication, several improvements or extensions to the original model and method have been proposed and tested. The DoG and CSS models included in the current study are already more flexible in terms of pRF profile, but they still employ a priori constraints on the pRF shape. Methods to estimate pRFs without such constraints also exist (Carvalho et al., 2020; Lee et al., 2013) and they can be particularly robust in their estimation of peripheral pRFs near the border of the visual stimulus (Lee et al., 2013). An ambition to estimate pRFs from neuroimaging data and that reflect neural populations that are as small as possible has inspired computationally intensive approaches to estimate pRFs for neuronal subpopulations within a voxel though 'micro-probing' (Carvalho et al., 2020) or to estimate the average receptive field size of single neurons within a voxel (Keliris et al., 2019). These novel methods, as well as the pRF models included in the current study, each offer specific advantages over the original pRF modeling approach that may or may not be important in addressing particular experimental questions.

Conclusions

In an extensive comparative study, we used fMRI in awake non-human primates to investigate BOLD-based population receptive fields throughout the primate brain and reveal their neuronal origins with large-scale neurophysiological recordings in visual cortex. Different pRF models captured different aspects of spatial tuning in the BOLD signal and relates them to different components of the underlying neurophysiological signals. Sub-additive spatial summation, was a general feature throughout brain areas and across BOLD, MUA and LFP signals. PRF models with negative components demonstrated tuned visual suppression in areas of the monkey default mode network and center-surround organization of pRFs in early visual areas. The structure of pRF-maps from neuroimaging, as captured by their eccentricity-size relationship, reflected the MUA in V1, but was more similar to the gamma power of the local field potential in V4. We conclude that population receptive fields in neuroimaging accurately represent the spatial tuning of the underlying neuronal populations, but that the spatial scope of these populations crucially depends on the brain area that is being probed.

bioRxiv preprint doi: https://doi.org/10.1101/2020.09.05.284133; this version posted September 8, 2020. The copyright holder for this preprint (which was not certified by peer review) is the author/funder, who has granted bioRxiv a license to display the preprint in perpetuity. It is made available under aCC-BY-NC 4.0 International license.

Materials and Methods

Subject details

Four male macaques (*Macaca mulatta;* 7-12 kg, 5-8 years old) participated in this study. Animal care and experimental procedures were in accordance with the NIH Guide for Care and Use of Laboratory Animals (National Institutes of Health, Bethesda, Maryland), the European legislation (Directive 2010/63/EU) and approved by the institutional animal care and use committee of the Royal Netherlands Academy of Arts and Sciences and the Central Authority for Scientific Procedures on Animals (CCD) in the Netherlands. The animals were socially housed in an enriched specialized primate facility with natural daylight, controlled temperature and humidity, and fed with standard primate chow, supplemented with raisins, fresh fruits, and vegetables. Their access to fluid was controlled, according to a carefully designed regime for fluid uptake. During weekdays the animals received diluted fruit juice in the experimental set-up. We ensured that the animals drank sufficient fluid in the set-up and supplemented with extra fluid after experimental sessions if they did not drink enough. On the weekends, animals received at least 700 ml of water in the home-cage. The animals were regularly checked by veterinary staff and animal caretakers and their weight and general appearance were recorded in an electronic logbook on a daily basis during fluid-control periods.

Surgical procedures

Two animals (M1 & M2) participated in the MRI experiments and were implanted with an MRI-compatible plastic (PEEK) head-post, fixed to the skull with ceramic bone screws and acrylic (Farivar and Vanduffel, 2014; Vanduffel et al., 2001). Anesthetics, analgesics and monitoring procedures were similar to previous surgical procedures in our laboratory and are described in detail elsewhere (Klink et al., 2017; Poort et al., 2012; Supèr and Roelfsema, 2005). Two other animals (M3 & M4) participated in the electrophysiology experiments. They were implanted with a custom 3D-printed titanium head-post that was designed in-house based on a CT-scan of the skull, aligned to a T1-weighted anatomical MRI-scan of the brain (Chen et al., 2017). Head-posts were attached to the skull with titanium bone-screws and the skin was closed around the implant without the use of any acrylic. In a second surgery, each animal was additionally implanted with a total of 1,024 electrodes spread over 16 Utah electrode arrays (Blackrock Microsystems) in their visual cortices (14 arrays in V1, 2 arrays in V4; Figure 1B). Each array contained an 8-by-8 grid of 64 iridium oxide electrodes with a length of 1.5 mm spaced at a distance of 400 µm from each other. Pre-implantation electrode impedances ranged from 6 to 12 kΩ. A custom designed 1,024-channel pedestal was attached to the skull with titanium bone screws and the skin was closed around it. More details on the surgical procedures are published elsewhere (Chen et al., 2017).

bioRxiv preprint doi: https://doi.org/10.1101/2020.09.05.284133; this version posted September 8, 2020. The copyright holder for this preprint (which was not certified by peer review) is the author/funder, who has granted bioRxiv a license to display the preprint in perpetuity. It is made available under aCC-BY-NC 4.0 International license.

Visual stimuli and procedures

Population receptive fields were measured using conventional moving bar stimuli that traversed the screen in eight different directions (Dumoulin and Wandell, 2008) (Fig. 1). In the MRI experiments, the bar sweep spanned a diameter of 16° in 20 steps (Dumoulin and Wandell, 2008). The moving bars were 2° wide and contained a checkerboard pattern (100% contrast, 0.5° checkers) that moved parallel to the bar's orientation. Each bar position was on the screen for 2.5 s (1 TR) making one full bar sweep last 50 s. Bar sweep series (all directions presented once) were preceded and followed by 37.5 s (15 TRs) of mean luminance. Each horizontal or vertical bar sweep was followed by a mean luminance period of 25 s. The order of the bar sweep directions was 270°, 315°, 180°, 225°, 90°, 135°, 0°, 45° on most runs, but for one animal we inverted the directions to 90°, 135°, 0°, 45°, 270°, 315°, 180°, 225° on some runs to compensate for the animal's tendency to fall asleep near the end of runs. Included data came from 8 scanning sessions for monkey M1 (34 runs, 268 included bar sweeps) and 10 sessions for monkey M2 (66 runs, 406 bar sweeps). During stimulus presentation the animals received fluid rewards (Crist Instruments, Hagerstown, MD) for maintaining fixation within 1.5° of a 0.15° red fixation dot, surrounded by a 0.75° aperture of mean luminance background color. In the electrophysiology experiments, the stimulus and task were very similar, but bar sweeps now spanned a diameter of 28° due to the animal being closer to the monitor. Bars now traveled along this path in 30 steps of 500 ms, and the mean luminance intervals were reduced to 2.5 s due to the much faster neuronal response (compared to the BOLD signal). In the MRI experiment, animals were head-fixed, sitting in the sphinx position (Farivar and Vanduffel, 2014; Vanduffel et al., 2001), and viewing a 32" screen (1920×1080 pixels, 100 Hz) (Cambridge Research Systems) at the far end of the bore, 130 cm away. Eye-position and pupil diameter were tracked with an MRI-compatible infrared eye-tracking system at 120 Hz (ISCAN ETL-200). Hand positions were also monitored using fiber optic amplifiers (Omron E3X-NH) and several sets of optic fibers. In the electrophysiology experiments, animals were head-fixed in a conventional vertical primate chair and viewed a 21" CRT monitor (1024×768, 85 Hz) at a distance of 64 cm while their eye-position and pupil diameters were tracked at 230 Hz using an infrared eye-tracker (TREC ET-49B, Thomas Recording GmbH).

MRI acquisition

MR-imaging was performed in a standard Philips Ingenia 3.0 T horizontal bore full-body scanner (Spinoza Center for Neuroimaging, Amsterdam, the Netherlands). We used a custom-built 8-channel phased array receive coil system (KU Leuven) and the scanner's full-body transmit coil. Functional images were obtained using a gradient-echo T2* echo-planar sequence (44 horizontal slices, in-plane 72 × 68 matrix, TR = 2500 ms, TE = 20 ms, flip angle = 77.2°, 1.25×1.25×1.25 mm isotropic voxels, SENSE-factor of 2 in the AP direction, and phase-encoding in the AP direction).

bioRxiv preprint doi: https://doi.org/10.1101/2020.09.05.284133; this version posted September 8, 2020. The copyright holder for this preprint (which was not certified by peer review) is the author/funder, who has granted bioRxiv a license to display the preprint in perpetuity. It is made available under aCC-BY-NC 4.0 International license.

fMRI preprocessing

All fMRI data was preprocessed with a custom-written Nipype pipeline that we have made available online (https://github.com/visionandcognition/NHP-BIDS). In short, MRI scans were exported from the scanner as DICOM images and converted to NIFTI files with the dcm2niix tool (Li et al., 2016). The volumes were then re-oriented to correct for the animal being in the sphinx position and resampled to 1 mm^3 isotropic voxels. The resulting images were then re-aligned using a non-rigid slice-by-slice registration algorithm based on AFNI tools (Cox, 1996) followed by FSL-based motion correction procedure MCFLIRT (Jenkinson et al., 2002). Functional volumes were linearly aligned to the individual high-resolution anatomical volumes, which were in turn non-linearly registered to the NMT standard space (Seidlitz et al., 2017). Preprocessed data was further processed with a combination of custom written Matlab (Mathworks, Natick, MA) and shell scripts (https://github.com/visionandcognition/NHP-PRF). BOLD time-courses for each voxel were normalized to percentage signal change and averaged across runs (or parts of runs) for which fixation was maintained at 80% of the time or more. We separately averaged odd and even runs to allow for a cross-validation approach in the evaluation of the pRF model fits. Anatomical regions of interest (ROI's) were defined based on a probabilistic atlas (Reveley et al., 2016; Seidlitz et al., 2017) and the individual retinotopic maps.

Post-fit comparisons across pRF-models, HRFs, and ROI's were performed in Matlab based on the volumetric results. For visualization of the fMRI data, volumetric results were also projected to the individual cortical surfaces. To create these surfaces, we averaged multiple anatomical scans (T1-weighted, 3D-FFE, TE = 6 ms, TR = 13 ms, TI = 900 ms, flip angle = 8°, 100 horizontal slices, in-plane 224 × 224 matrix, 0.6×0.6×0.6 mm isotropic voxels, and phase-encoding in the AP direction) and processed the result with customized tools based on Freesurfer (Fischl, 2012) and Pycortex (Gao et al., 2015) that were adjusted to handle our NHP data. These tools and their documentation can be found at https://github.com/VisionandCognition/NHP-Freesurfer and https://github.com/VisionandCognition/NHP-pycortex respectively.

Electrophysiology acquisition

Raw neuronal activity was acquired from 1,024 channels simultaneously at a 30 kHz sample rate. The 1,024-channel pedestal connected to eight 128-channel CerePlex M head-stages through an electronic interface board. Each head-stage processed signals from two 64-channel electrode arrays with a 0.3-7,500 Hz analog filter at unity gain (i.e., no amplification). After analog-to-digital conversion, the signal from each head-stage was sent to a 128-channel Digital Hub (Blackrock Microsystems) where it was converted into an optical output signal and sent to a 128-channel Neural Signal Processor (NSP, Blackrock Microsystems) for storage and further processing. The eight NSP's were controlled with eight simultaneously running instances of the Blackrock Central Software Suite (Blackrock Microsystems) distributed over two computers (four instances each).

bioRxiv preprint doi: https://doi.org/10.1101/2020.09.05.284133; this version posted September 8, 2020. The copyright holder for this preprint (which was not certified by peer review) is the author/funder, who has granted bioRxiv a license to display the preprint in perpetuity. It is made available under aCC-BY-NC 4.0 International license.

Electrophysiology data preprocessing

The raw neuronal signal that was acquired using eight simultaneously running software instances was temporally aligned using common TTL pulses sent by the stimulus computer. The data were then separated in 1) envelope multi-unit activity (MUA), and 2) broadband local field potential (LFP). Envelope MUA represents the spiking activity of a local population of neurons around the electrode (Supèr and Roelfsema, 2005). To extract it, we amplified the raw neuronal signal, band-pass filtered it between 500 Hz and 9 kHz, full-wave rectified it, and applied a low-pass filter of 200 Hz. The resulting time-series were down-sampled to 1 kHz. We subtracted the baseline MUA activity in a 1,000 ms prestimulus time-window. Baseline-corrected MUA responses were then averaged, first across runs and then within a 50-500 ms time window for each stimulus position. The broadband LFP signal was generated by low-pass filtering the raw signal at 150 Hz and down-sampling it to 500 Hz. The LFP signal was further processed with a multi-taper method using the Chronux toolbox (Bokil et al., 2010). Power spectra were calculated in a 500 ms moving window (step-size 50 ms), using a time bandwidth product of 5 and 9 tapers. LFP power over time was then averaged within five distinct frequency bands: 4-8 Hz (Theta), 8-16 Hz (Alpha), 16-30 Hz (Beta), 30-60 Hz (low Gamma), and 60-120 Hz (high Gamma). Baseline power in a 1,000 ms prestimulus period was subtracted and the resulting signal on each channel was then averaged across runs, within a 50-500 ms time window during each stimulus position.

Population receptive fields models and fitting procedure

We fit four different pRF-models to all the data (voxels and electrode channels) using a customized version of the analyzePRF toolbox (Kay et al., 2013) for Matlab. In the fitting procedure, the stimuli were spatially down-sampled to a resolution of 10 pixels per degree visual angle and converted to 'effective stimuli', consisting of binary representations that encode stimulus position. Responses predictions were then calculated as the product of the effective stimulus and the pRF shape (Eq. 1). The four pRF-models differed in their description of the pRF shape. Linear models (Eq. 1-3) describe a single isotropic 2D Gaussian-shaped pRF and assume linear spatial summation across the visual field (Dumoulin and Wandell, 2008). We implemented two linear model versions. For the first model, responses were constrained to be positively related to the visual stimuli (P-LIN). A second version lacked this constraint and also allowed negative responses, or stimulus-driven activity reductions (U-LIN). Negative visual responses have been reported in the power of lower frequency components of the LFP and its coherence with spiking activity (Harvey et al., 2013; Klink et al., 2012; van Kerkoerle et al., 2014). Negative BOLD responses have also been demonstrated in some brain areas (Shmuel et al., 2006). The Non-linear Spatial Summation model (Kay et al., 2013) expands the linear model with a power-law exponent that is applied after spatial summation and captures non-linear summation of signals across the visual field. It has previously been shown that the value of this exponent is generally smaller than one in human visual cortex, indicating sub-additive spatial summation or compressive spatial summation (Kay et al., 2013). This model is therefore generally referred to as the compressive spatial

bioRxiv preprint doi: https://doi.org/10.1101/2020.09.05.284133; this version posted September 8, 2020. The copyright holder for this preprint (which was not certified by peer review) is the author/funder, who has granted bioRxiv a license to display the preprint in perpetuity. It is made available under aCC-BY-NC 4.0 International license.

summation (CSS) model. Because the pRF size and static non-linearity interact in the non-linear model, the pRF size is defined as the standard deviation of the predicted Gaussian response profile to a point stimulus (Eq. 3). The mathematical descriptions of the linear and non-linear pRF-models are described in Equations 1-3, where $Resp_{\text{pred}}$ indicates the predicted response, g is a gain factor to scale the response, $S(x,y)$ is the effective stimulus, $G(x,y)$ the Gaussian pRF profile, and n the exponent that determines the static spatial non-linearity. For the P-LIN model, the gain g was constrained to positive values, while for the U-LIN model, gain values could be negative as well. Negative gain factors imply stimulus-induced reductions of activity. In both linear models, the exponent n was fixed to be one. In the definition of the Gaussian, (x_0,y_0) defines the center and σ the standard deviation of the pRF.

Linear and Non-linear spatial summation pRF models

[1] $$Resp_{\text{pred}} = g \cdot \left[\sum_{x,y} S(x,y) G(x,y) \right]^n, \begin{matrix} \text{P-LIN, U-LIN}: n=1 \\ \text{P-LIN, CSS}: g>0 \end{matrix}$$

[2] $$G(x,y) = e^{\frac{-(x-x_0)^2+(y-y_0)^2}{2\sigma^2}}$$

[3] $$pRF_{\text{size}} = \frac{\sigma}{\sqrt{n}}$$

The difference-of-Gaussians model uses a standard linear Gaussian pRF-model (G_1 in Eq. 4) to describe the excitatory center of a pRF but it subtracts a second Gaussian profile (G_2) to explicitly model an inhibitory surround component (Zuiderbaan et al., 2012). This second Gaussian is by definition broader than the one describing the center. The relative sizes (σ_1,σ_2) and amplitudes (a) of the center and surround Gaussians are additional parameters in the model (Eq. 4-6).

Difference-of-Gaussians pRF model

[4] $$Resp_{\text{pred}} = g \cdot \left[\sum_{x,y} S(x,y) \left(G_1(x,y) - a \cdot G_2(x,y) \right) \right]^n$$

[5] $$G_1(x,y) = e^{\frac{-(x-x_0)^2+(y-y_0)^2}{2(\sigma_1)^2}}, G_2(x,y) = e^{\frac{-(x-x_0)^2+(y-y_0)^2}{2(\sigma_2)^2}}; \sigma_2 > \sigma_1$$

[6] $$pRF_{\text{center-size}} = \sigma_1, pRF_{\text{surr-size}} = \sigma_2$$

The models generate temporal response predictions based on the series of stimulus presentations and their estimate of the response properties of neuronal populations (pRF profile). This prediction assumes a near-

bioRxiv preprint doi: https://doi.org/10.1101/2020.09.05.284133; this version posted September 8, 2020. The copyright holder for this preprint (which was not certified by peer review) is the author/funder, who has granted bioRxiv a license to display the preprint in perpetuity. It is made available under aCC-BY-NC 4.0 International license.

instantaneous link between the stimulus and the response dynamics. This assumption holds true for the electrophysiological signals where the stimulus changes position every 500 ms, which is much slower than the typical delay of a neuronal response. The BOLD-response, however, is much slower than the speed with which the stimulus traverses the screen in the fMRI experiments (2,500 ms per position). For this reason we convolved the predicted response with a hemodynamic response function (HRF) to approximate the BOLD-dynamics. This convolution was done at a temporal resolution of 1.25 seconds per sample (twice the acquisition rate of TR = 2.5s) to facilitate model performance. We used both a canonical human HRF and a standard monkey HRF that we derived from separate scanning sessions in our laboratory (Supplemental Figure S5). In short, we presented the animals with brief (0.1 s) full contrast and fullscreen checkerboard stimuli. We then used FMRIB's Linear Optimal Basis Sets (FLOBS) (Woolrich et al., 2004) toolkit from the FSL software package to estimate the relative contributions of a set of basis functions for those voxels in the primary visual cortex that were significantly activated by the stimulus. We then calculated a single weighted average HRF function based on these basis functions and used this average HRF as the standard monkey HRF. Compared to the canonical human HRF this monkey HRF was narrower, with a slightly faster time-to-peak and a clearly faster peak-to-fall time. A comparison of model accuracy for the two HRFs revealed a small overall advantage for the monkey HRF, that was especially evident in the earlier visual areas (Supplemental Figure S5). Because size and location estimates were highly similar for the two HRFs across all models, we only report results from model-fits based on the monkey HRF.

Model-fitting was performed on a cluster-computer (LISA, SURFsara) using nonlinear optimization (MATLAB Optimization Toolbox). The accuracy of the different model-fits was quantified as the cross-validated percentage of variance (R^2) in the measured BOLD-response (Eq. 8: *DATA*) and the model prediction (Eq, 8: *MODEL*). To this end, we divided the data into two non-overlapping sets (odd and even runs) and tested the prediction of a model that was fit one data-set against the time-series of the other data-set and vice-versa. This yielded two R^2 values per voxel or electrode, that were subsequently averaged. The cross-validated determination of model accuracy allows a comparison of model performance across models with different numbers of parameters and prevents over-fitting. Fit-results are available as voxel-based maps warped to the NMT template space on Neurovault.org (Gorgolewski et al., 2015) at https://identifiers.org/neurovault.collection:8082.

Model accuracy

[7] $$R^2 = 100 \times \left[1 - \frac{\sum (MODEL - DATA)^2}{\sum DATA^2} \right]$$

bioRxiv preprint doi: https://doi.org/10.1101/2020.09.05.284133; this version posted September 8, 2020. The copyright holder for this preprint (which was not certified by peer review) is the author/funder, who has granted bioRxiv a license to display the preprint in perpetuity. It is made available under aCC-BY-NC 4.0 International license.

Comparison of pRF (& RF) estimates

After fitting the pRF models to all voxels and electrode channels we compared the pRF estimates both within and across recording modalities. For these comparisons, unless otherwise noted, we pooled voxels and recording channels across subjects and used non-parametric statistical tests (Wilcoxon Signed Rank, Wilcoxon Rank Sum, or Kruskal-Wallis) with post-hoc Tukey's HSD tests to correct for multiple comparisons. For the fMRI data we compared model accuracy between models and hemodynamic response functions. Using the best overall pRF model and HRF, we then constructed retinotopic maps for a large range of ROI's and investigated the relationship between pRF eccentricity and size for a subset of ROI's with good model fits ($R^2 > 5\%$). For the electrophysiological data, we again compared model accuracy and pRF estimates across MUA and LFP components to unravel to which extent retinotopic information is available in the different neuronal signals. We also compared the pRF estimates of each electrode channel to a receptive field characterization based on more conventional techniques that are typically used in our laboratory (and many others). To this end, we recorded the MUA responses to thin, translating bar stimuli. The averaged MUA traces were fitted with a Gaussian curve that determined the onset and offset of the visual response (95% of the peak of the Gaussian). Horizontal and vertical receptive field boundaries were then derived from the onset and offset times for stimuli moving in opposite directions. Receptive field centers were defined as the midpoint between the horizontal and vertical borders, while receptive field size was calculated as the square root of the rectangular receptive field surface, divided by two to be more similar to the sizes obtained through pRF model fits.

In order to compare pRF properties based on fMRI BOLD signals with those estimated from electrophysiologically recorded neuronal signals, we combined data from individual animals to create one pool of BOLD-based voxel pRFs and six pools of electrophysiology-based electrode pRFs (MUA, and the different frequency bands of the LFP) for V1 and V4 data. For each visual area, we then compared the pRFs across modalities on the basis of the relationship between receptive field eccentricity and receptive field size with a set of Linear Mixed Models (LMM's). Each signal type was first tested on the presence of a significant correlation between eccentricity and size. The signal types that exhibited such a correlation were subsequently tested together in a single LMM to determine whether the eccentricity-size relationship depended on signal type (interaction SIGNAL × ECC). Finally, we tested each electrophysiology signal with significant eccentricity-size correlation against the MRI results to determine if this relationship was different for the two selected signal types. For this analysis, we selected voxels from V1 and V4 with a pRF location that fell within the eccentricity range of the electrode arrays and only included voxels and electrodes for which a fit accuracy above a predetermined threshold (fMRI threshold: $R^2 > 5\%$, electrophysiology threshold: $R^2 > 50\%$).

Data and code availability

All data, experiment code, and analysis code used for this study have been made freely available.

bioRxiv preprint doi: https://doi.org/10.1101/2020.09.05.284133; this version posted September 8, 2020. The copyright holder for this preprint (which was not certified by peer review) is the author/funder, who has granted bioRxiv a license to display the preprint in perpetuity. It is made available under aCC-BY-NC 4.0 International license.

Acknowledgments

We thank Jonathan Williford for his contributions to the fMRI preprocessing pipeline; Pieter Buur, Wietske van der Zwaag, Diederick Stoffers, and the Laboratory of Neuro- and Psychophysiology of KU Leuven for technical assistance in setting up the non-human primate MR infrastructure; Kor Brandsma and Anneke Ditewig for animal care and biotechnical assistance; Feng Wang for help with electrophysiology data collection; and Chris van der Togt for help with data management.

Author contributions (CRediT)

P.C. Klink: Conceptualization, Methodology, Software, Investigation, Formal Analysis, Resources, Data Curation, Writing – Original Draft Preparation, Writing – Review & Editing, Visualization, Project Administration, Funding Acquisition.

X. Chen: Investigation, Formal Analysis, Writing – Review & Editing, Funding Acquisition.

W. Vanduffel: Methodology, Writing – Review & Editing.

P.R. Roelfsema: Conceptualization, Resources, Supervision, Funding Acquisition, Writing – Review & Editing.

References

Ahmadi K, Fracasso A, Puzniak RJ, Gouws AD, Yakupov R, Speck O, Kaufmann J, Pestilli F, Dumoulin SO, Morland AB, Hoffmann MB. 2020. Triple visual hemifield maps in a case of optic chiasm hypoplasia. *NeuroImage* **215**:116822. doi:10/ggz9kc

Allman JM, Miezin F, McGuinness E. 1985. Stimulus specific responses from beyond the classical receptive field: neurophysiological mechanisms for local-global comparisons in visual neurons. *Annu Rev Neurosci* **8**:407–430. doi:10.1146/annurev.ne.08.030185.002203

Alvarez I, Smittenaar R, Handley SE, Liasis A, Sereno MI, Schwarzkopf DS, Clark CA. 2020. Altered visual population receptive fields in human albinism. *Cortex J Devoted Study Nerv Syst Behav* **128**:107–123. doi:10/ggz9km

Amano K, Wandell BA, Dumoulin SO. 2009. Visual Field Maps, Population Receptive Field Sizes, and Visual Field Coverage in the Human MT+ Complex. *Journal of Neurophysiology* **102**:2704–2718. doi:10/d79g3p

Arcaro MJ, Pinsk MA, Li X, Kastner S. 2011. Visuotopic Organization of Macaque Posterior Parietal Cortex: A Functional Magnetic Resonance Imaging Study. *J Neurosci* **31**:2064–2078. doi:10.1523/JNEUROSCI.3334-10.2011

Arsenault JT, Caspari N, Vandenberghe R, Vanduffel W. 2018. Attention Shifts Recruit the Monkey Default Mode Network. *J Neurosci* **38**:1202–1217. doi:10.1523/JNEUROSCI.1111-17.2017

bioRxiv preprint doi: https://doi.org/10.1101/2020.09.05.284133; this version posted September 8, 2020. The copyright holder for this preprint (which was not certified by peer review) is the author/funder, who has granted bioRxiv a license to display the preprint in perpetuity. It is made available under aCC-BY-NC 4.0 International license.

Arthurs OJ, Boniface S. 2002. How well do we understand the neural origins of the fMRI BOLD signal? *Trends in Neurosciences* **25**:27–31. doi:10/cjsw99

Barlow H, Levick W, Westheimer G, Spinelli DN. 1966. Computer-plotted receptive fields. *Science* **154**:921.

Bartels A, Logothetis NK, Moutoussis K. 2008. fMRI and its interpretations: an illustration on directional selectivity in area V5/MT. *Trends Neurosci* **31**:444–453. doi:10.1016/j.tins.2008.06.004

Benson NC, Jamison KW, Arcaro MJ, Vu AT, Glasser MF, Coalson TS, Essen DCV, Yacoub E, Ugurbil K, Winawer J, Kay K. 2018. The Human Connectome Project 7 Tesla retinotopy dataset: Description and population receptive field analysis. *J Vision* **18**:23. doi:10/gfsjc2

Best PB de, Raz N, Guy N, Ben-Hur T, Dumoulin SO, Pertzov Y, Levin N. 2019. Role of Population Receptive Field Size in Complex Visual Dysfunctions: A Posterior Cortical Atrophy Model. *Jama Neurol* **76**:1391–1396. doi:10/ggz9kp

Binda P, Kurzawski JW, Lunghi C, Biagi L, Tosetti M, Morrone MC. 2018. Response to short-term deprivation of the human adult visual cortex measured with 7T BOLD. *Elife* **7**:e40014. doi:10/ggz9kw

Bokil H, Andrews P, Kulkarni JE, Mehta S, Mitra PP. 2010. Chronux: A platform for analyzing neural signals. *J Neurosci Methods* **192**:146–151. doi:10.1016/j.jneumeth.2010.06.020

Bonin V, Histed MH, Yurgenson S, Reid RC. 2011. Local diversity and fine-scale organization of receptive fields in mouse visual cortex. *J Neurosci* **31**:18506–18521. doi:10/ffw6ss

Boynton GM. 2011. Spikes, BOLD, Attention, and Awareness: A comparison of electrophysiological and fMRI signals in V1. *J Vis* **11**:12–12. doi:10.1167/11.5.12

Britten KH, Heuer HW. 1999. Spatial summation in the receptive fields of MT neurons. *J Neurosci* **19**:5074–5084.

Buzsaki G. 2006. Rhythms of the Brain. Oxford University Press.

Buzsaki G. 2004. Neuronal Oscillations in Cortical Networks. *Science* **304**:1926–1929. doi:10.1126/science.1099745

Buzsáki G, Wang X-J. 2012. Mechanisms of Gamma Oscillations. *Annu Rev Neurosci* **35**:203–225. doi:10.1146/annurev-neuro-062111-150444

Carvalho J, Invernizzi A, Ahmadi K, Hoffmann MB, Renken RJ, Cornelissen FW. 2020. Micro-probing enables fine-grained mapping of neuronal populations using fMRI. *NeuroImage* **209**:116423. doi:10.1016/j.neuroimage.2019.116423

Cavanaugh P, Bair W, Movshon JA. 2002. Nature and interaction of signals from the receptive field center and surround in macaque V1 neurons. *J Neurophysiol* **88**:2530–2546.

Chen X, Possel JK, Wacongne C, van Ham AF, Klink PC, Roelfsema PR. 2017. 3D printing and modelling of customized implants and surgical guides for non-human primates. *J Neurosci Methods* **286**:38–55. doi:10.1016/j.jneumeth.2017.05.013

Cotton PL, Smith AT. 2007. Contralateral Visual Hemifield Representations in the Human Pulvinar Nucleus. *Journal of Neurophysiology* **98**:1600–1609. doi:10/c2sx5j

bioRxiv preprint doi: https://doi.org/10.1101/2020.09.05.284133; this version posted September 8, 2020. The copyright holder for this preprint (which was not certified by peer review) is the author/funder, who has granted bioRxiv a license to display the preprint in perpetuity. It is made available under aCC-BY-NC 4.0 International license.

Cox RW. 1996. AFNI: Software for Analysis and Visualization of Functional Magnetic Resonance Neuroimages. *Comput Biomed Res* **29**:162–173. doi:10/ctwqf6

Dekker TM, Schwarzkopf DS, de Haas B, Nardini M, Sereno MI. 2019. Population receptive field tuning properties of visual cortex during childhood. *Developmental Cognitive Neuroscience* **37**:100614. doi:10.1016/j.dcn.2019.01.001

DeSimone K, Viviano JD, Schneider KA. 2015. Population Receptive Field Estimation Reveals New Retinotopic Maps in Human Subcortex. *J Neurosci* **35**:9836–9847. doi:10.1523/JNEUROSCI.3840-14.2015

Drew PJ. 2019. Vascular and neural basis of the BOLD signal. *Current Opinion in Neurobiology* **58**:61–69. doi:10/ggf3xg

Dumoulin SO, Knapen T. 2018. How Visual Cortical Organization Is Altered by Ophthalmologic and Neurologic Disorders. *Annual Review of Vision Science* **4**:357–379. doi:10/ggt2mw

Dumoulin SO, Wandell BA. 2008. Population receptive field estimates in human visual cortex. *Neuroimage* **39**:647–660. doi:10.1016/j.neuroimage.2007.09.034

Einevoll GT, Kayser C, Logothetis NK, Panzeri S. 2013. Modelling and analysis of local field potentials for studying the function of cortical circuits. *Nature Reviews Neuroscience* **14**:770–785. doi:10/f5drx4

Ekman M, Roelfsema PR, de Lange FP. 2020. Object selection by automatic spreading of top-down attentional signals in V1 (preprint). Neuroscience. doi:10.1101/2020.02.24.962761

Ekstrom A. 2010. How and when the fMRI BOLD signal relates to underlying neural activity: The danger in dissociation. *Brain Research Reviews* **62**:233–244. doi:10/cm4cxg

Engel SA. 2012. The development and use of phase-encoded functional MRI designs. *Neuroimage* **62**:1195–1200. doi:10.1016/j.neuroimage.2011.09.059

Engel SA, Rumelhart DE, Wandell BA, Lee AT, Glover GH, Chichilnisky E-J, Shadlen MN. 1994. fMRI of human visual cortex. *Nature* **369**:525–525. doi:10.1038/369525a0

Farivar R, Vanduffel W. 2014. Functional MRI of Awake Behaving Macaques Using Standard EquipmentAdvanced Brain Neuroimaging Topics in Health and Disease - Methods and Applications.

Felleman D, van Essen DC. 1991. Distributed hierarchical processing in the primate cerebral cortex. *Cereb Cortex* **1**:1–47.

Felleman DJ, Van Essen DC. 1987. Receptive field properties of neurons in area V3 of macaque monkey extrastriate cortex. *Journal of Neurophysiology* **57**:889–920. doi:10.1152/jn.1987.57.4.889

Fiebelkorn IC, Kastner S. 2019. The Puzzling Pulvinar. *Neuron* **101**:201–203. doi:10.1016/j.neuron.2018.12.032

Fiebelkorn IC, Pinsk MA, Kastner S. 2019. The mediodorsal pulvinar coordinates the macaque fronto-parietal network during rhythmic spatial attention. *Nat Commun* **10**:215. doi:10.1038/s41467-018-08151-4

Fischl B. 2012. FreeSurfer. *Neuroimage* **62**:774–781. doi:10/fzcbq3

Fries P. 2009. Neuronal gamma-band synchronization as a fundamental process in cortical computation. *Annu Rev Neurosci* **32**:209–224. doi:10.1146/annurev.neuro.051508.135603

bioRxiv preprint doi: https://doi.org/10.1101/2020.09.05.284133; this version posted September 8, 2020. The copyright holder for this preprint (which was not certified by peer review) is the author/funder, who has granted bioRxiv a license to display the preprint in perpetuity. It is made available under aCC-BY-NC 4.0 International license.

Gao JS, Huth AG, Lescroart MD, Gallant JL. 2015. Pycortex: an interactive surface visualizer for fMRI. *Front Neuroinform* **9**:162–12. doi:10.3389/fninf.2015.00023

Gattass R, Nascimento-Silva S, Soares JGM, Lima B, Jansen AK, Diogo ACM, Farias MF, Botelho MMEP, Mariani OS, Azzi JCB, Fiorani M. 2005. Cortical visual areas in monkeys: location, topography, connections, columns, plasticity and cortical dynamics. *Philos Trans R Soc Lond B Biol Sci* **360**:709–731. doi:10.1098/rstb.2005.1629

Ghazizadeh A, Griggs W, Leopold DA, Hikosaka O. 2018. Temporal–prefrontal cortical network for discrimination of valuable objects in long-term memory. *Proc Natl Acad Sci USA* **115**:E2135–E2144. doi:10/gc6sbj

Goense J, Bohraus Y, Logothetis NK. 2016. fMRI at High Spatial Resolution: Implications for BOLD-Models. *Front Comput Neurosci* **10**. doi:10/ggmdz8

Goense JBM, Logothetis NK. 2008. Neurophysiology of the BOLD fMRI signal in awake monkeys. *CURR BIOL* **18**:631–640. doi:10.1016/j.cub.2008.03.054

Gorgolewski KJ, Varoquaux G, Rivera G, Schwarz Y, Ghosh SS, Maumet C, Sochat VV, Nichols TE, Poldrack RA, Poline J-B, Yarkoni T, Margulies DS. 2015. NeuroVault.org: a web-based repository for collecting and sharing unthresholded statistical maps of the human brain. *Front Neuroinform* **9**. doi:10/ggz9kx

Green T, Hosseini H, Piccirilli A, Ishak A, Grill-Spector K, Reiss AL. 2019. X-Chromosome Insufficiency Alters Receptive Fields across the Human Early Visual Cortex. *J Neurosci Official J Soc Neurosci* **39**:8079–8088. doi:10/ggz9ks

Griggs WS, Kim HF, Ghazizadeh A, Costello MG, Wall KM, Hikosaka O. 2017. Flexible and Stable Value Coding Areas in Caudate Head and Tail Receive Anatomically Distinct Cortical and Subcortical Inputs. *Front Neuroanat* **11**. doi:10/ggz9j8

Haak KV, Winawer J, Ben M Harvey, Renken R, Dumoulin SO, Wandell BA, Cornelissen FW. 2013. Connective field modeling. *Neuroimage* **66**:376–384. doi:10.1016/j.neuroimage.2012.10.037

Haegens S, Nácher V, Luna R, Romo R, Jensen O. 2011. α-Oscillations in the monkey sensorimotor network influence discrimination performance by rhythmical inhibition of neuronal spiking. *Proc Natl Acad Sci USA* **108**:19377–19382. doi:10.1073/pnas.1117190108

Halassa MM, Kastner S. 2017. Thalamic functions in distributed cognitive control. *Nature Neuroscience* **20**:1669–1679. doi:10.1038/s41593-017-0020-1

Hartline HK. 1938. The response of single optic nerve fibers of the vertebrate eye to illumination of the retina. *American Journal of Physiology-Legacy Content*. doi:10/ggt2mv

Harvey BM, Dumoulin SO, Fracasso A, Paul JM. 2020. A Network of Topographic Maps in Human Association Cortex Hierarchically Transforms Visual Timing-Selective Responses. *Current Biology* **30**:1424-1434.e6. doi:10/ggt2mz

bioRxiv preprint doi: https://doi.org/10.1101/2020.09.05.284133; this version posted September 8, 2020. The copyright holder for this preprint (which was not certified by peer review) is the author/funder, who has granted bioRxiv a license to display the preprint in perpetuity. It is made available under aCC-BY-NC 4.0 International license.

Harvey BM, Fracasso A, Petridou N, Dumoulin SO. 2015. Topographic representations of object size and relationships with numerosity reveal generalized quantity processing in human parietal cortex. *Proc Natl Acad Sci USA* 201515414–6. doi:10.1073/pnas.1515414112

Harvey BM, Vansteensel MJ, Ferrier CH, Petridou N, Zuiderbaan W, Aarnoutse EJ, Bleichner MG, Dijkerman HC, van Zandvoort MJE, Leijten FSS, Ramsey NF, Dumoulin SO. 2013. Frequency specific spatial interactions in human electrocorticography: V1 alpha oscillations reflect surround suppression. *Neuroimage* **65**:424–432. doi:10.1016/j.neuroimage.2012.10.020

He D, Wang Y, Fang F. 2019. The Critical Role of V2 Population Receptive Fields in Visual Orientation Crowding. *Curr Biol* **29**:2229-2236.e3. doi:10/ggz9kt

Hikosaka O, Sakamoto M, Usui S. 1989a. Functional properties of monkey caudate neurons. II. Visual and auditory responses. *J Neurophysiol* **61**:799–813.

Hikosaka O, Sakamoto M, Usui S. 1989b. Functional properties of monkey caudate neurons. III. Activities related to expectation of target and reward. *J Neurophysiol* **61**:814–832.

Hubel DH, Wiesel TN. 1998. Early exploration of the visual cortex. *Neuron* **20**:401–412.

Hubel DH, Wiesel TN. 1974. Uniformity of monkey striate cortex: a parallel relationship between field size, scatter, and magnification factor. *J Comp Neurol* **158**:295–305. doi:10/d4tnkt

Hubel DH, Wiesel TN. 1968. Receptive fields and functional architecture of monkey striate cortex. *J Physiol (Lond)* **195**:215–243.

Hubel DH, Wiesel TN. 1959. Receptive fields of single neurones in the cat's striate cortex. *J Physiol (Lond)* **148**:574–591.

Hughes AE, Greenwood JA, Finlayson NJ, Schwarzkopf DS. 2019. Population receptive field estimates for motion-defined stimuli. *Neuroimage* **199**:245–260. doi:10/ggz9kv

Janssens T, Keil B, Farivar R, McNab JA, Polimeni JR, Gerits A, Arsenault JT, Wald LL, Vanduffel W. 2012. An implanted 8-channel array coil for high-resolution macaque MRI at 3T. *Neuroimage* **62**:1529–1536. doi:10.1016/j.neuroimage.2012.05.028

Janssens T, Zhu Q, Popivanov ID, Vanduffel W. 2014. Probabilistic and Single-Subject Retinotopic Maps Reveal the Topographic Organization of Face Patches in the Macaque Cortex. *J Neurosci* **34**:10156–10167. doi:10.1523/JNEUROSCI.2914-13.2013

Jenkinson M, Bannister P, Brady M, Smith S. 2002. Improved Optimization for the Robust and Accurate Linear Registration and Motion Correction of Brain Images. *Neuroimage* **17**:825–841. doi:10/ctfvqv

Kay KN, Winawer J, Mezer A, Wandell BA. 2013. Compressive spatial summation in human visual cortex. *J Neurophysiol* **110**:481–494. doi:10.1152/jn.00105.2013

Keliris GA, Li Q, Papanikolaou A, Logothetis NK, Smirnakis SM. 2019. Estimating average single-neuron visual receptive field sizes by fMRI. *Proc Natl Acad Sci USA* **62**:201809612–10. doi:10.1073/pnas.1809612116

Kim HF, Hikosaka O. 2013. Distinct Basal Ganglia Circuits Controlling Behaviors Guided by Flexible and Stable Values. *Neuron* 1–10. doi:10.1016/j.neuron.2013.06.044

bioRxiv preprint doi: https://doi.org/10.1101/2020.09.05.284133; this version posted September 8, 2020. The copyright holder for this preprint (which was not certified by peer review) is the author/funder, who has granted bioRxiv a license to display the preprint in perpetuity. It is made available under aCC-BY-NC 4.0 International license.

Klink PC, Dagnino B, Gariel-Mathis M-A, Roelfsema PR. 2017. Distinct Feedforward and Feedback Effects of Microstimulation in Visual Cortex Reveal Neural Mechanisms of Texture Segregation. *Neuron* 1–16. doi:10.1016/j.neuron.2017.05.033

Klink PC, Oleksiak A, Lankheet MJM, van Wezel RJA. 2012. Intermittent stimulus presentation stabilizes neuronal responses in macaque area MT. *J Neurophysiol* **108**:2101–2114. doi:10.1152/jn.00252.2012

Knierim JJ, van Essen DC. 1992. Neuronal responses to static texture patterns in area V1 of the alert macaque monkey. *Journal of Neurophysiology* **67**:961–980. doi:10.1152/jn.1992.67.4.961

Kolster H, Janssens T, Orban GA, Vanduffel W. 2014. The Retinotopic Organization of Macaque Occipitotemporal Cortex Anterior to V4 and Caudoventral to the Middle Temporal (MT) Cluster. *J Neurosci* **34**:10168–10191. doi:10.1523/JNEUROSCI.3288-13.2014

Kolster H, Mandeville JB, Arsenault JT, Ekstrom LB, Wald LL, Vanduffel W. 2009. Visual field map clusters in macaque extrastriate visual cortex. *J Neurosci* **29**:7031–7039. doi:10.1523/JNEUROSCI.0518-09.2009

Kolster H, Peeters R, Orban GA. 2010. The retinotopic organization of the human middle temporal area MT/V5 and its cortical neighbors. *J Neurosci* **30**:9801–9820. doi:10.1523/JNEUROSCI.2069-10.2010

Kunimatsu J, Maeda K, Hikosaka O. 2018. The caudal part of putamen represents the historical object value information. *J Neurosci* 2534–18. doi:10/ggz9j7

Larsson J, Heeger DJ. 2006. Two retinotopic visual areas in human lateral occipital cortex. *J Neurosci* **26**:13128–13142. doi:10.1523/JNEUROSCI.1657-06.2006

Lee S, Papanikolaou A, Logothetis NK, Smirnakis SM, Keliris GA. 2013. A new method for estimating population receptive field topography in visual cortex. *Neuroimage* **81**:144–157. doi:10.1016/j.neuroimage.2013.05.026

Łęski S, Lindén H, Tetzlaff T, Pettersen KH, Einevoll GT. 2013. Frequency Dependence of Signal Power and Spatial Reach of the Local Field Potential. *PLOS Computational Biology* **9**:e1003137. doi:10.1371/journal.pcbi.1003137

Li X, Morgan PS, Ashburner J, Smith J, Rorden C. 2016. The first step for neuroimaging data analysis: DICOM to NIfTI conversion. *J Neurosci Methods* **264**:47–56. doi:10.1016/j.jneumeth.2016.03.001

Lima B, Cardoso MMB, Sirotin YB, Das A. 2014. Stimulus-Related Neuroimaging in Task-Engaged Subjects Is Best Predicted by Concurrent Spiking. *J Neurosci* **34**:13878–13891. doi:10.1523/JNEUROSCI.1595-14.2014

Logothetis NK. 2010. Bold claims for optogenetics. *Nature* **468**:E3–E4. doi:10.1038/nature09532

Logothetis NK. 2003. The underpinnings of the BOLD functional magnetic resonance imaging signal. *J Neurosci* **23**:3963–3971.

Logothetis NK, Pauls J, Augath MA, Trinath T, Oeltermann A. 2001. Neurophysiological investigation of the basis of the fMRI signal. *Nature* **412**:150–157.

Logothetis NK, Wandell BA. 2004. Interpreting the BOLD Signal. *Annu Rev Physiol* **66**:735–769. doi:10.1146/annurev.physiol.66.082602.092845

bioRxiv preprint doi: https://doi.org/10.1101/2020.09.05.284133; this version posted September 8, 2020. The copyright holder for this preprint (which was not certified by peer review) is the author/funder, who has granted bioRxiv a license to display the preprint in perpetuity. It is made available under aCC-BY-NC 4.0 International license.

Maier A, Wilke M, Aura CJ, Zhu C, Ye FQ, Leopold DA. 2008. Divergence of fMRI and neural signals in V1 during perceptual suppression in the awake monkey. *Nat Neurosci* **11**:1193–1200. doi:10.1038/nn.2173

Mantini D, Gerits A, Nelissen K, Durand J-B, Joly O, Simone L, Sawamura H, Wardak C, Orban GA, Buckner RL, Vanduffel W. 2011. Default mode of brain function in monkeys. *J Neurosci* **31**:12954–12962. doi:10.1523/JNEUROSCI.2318-11.2011

Mo C, He D, Fang F. 2017. Attention priority map of face images in human early visual cortex. *J Neurosci* 1206–17. doi:10.1523/JNEUROSCI.1206-17.2017

Mukamel R, Gelbard H, Arieli A, Hasson U, Fried I, Malach R. 2005. Coupling between neuronal firing, field potentials, and FMRI in human auditory cortex. *Science* **309**:951–954. doi:10.1126/science.1110913

Niessing J, Ebisch B, Schmidt KE, Niessing M, Singer W, Galuske RAW. 2005. Hemodynamic Signals Correlate Tightly with Synchronized Gamma Oscillations. *Science* **309**:948–951. doi:10/bz27m7

Nir Y, Fisch L, Mukamel R, Gelbard-Sagiv H, Arieli A, Fried I, Malach R. 2007. Coupling between Neuronal Firing Rate, Gamma LFP, and BOLD fMRI Is Related to Interneuronal Correlations. *Current Biology* **17**:1275–1285. doi:10/b93t7b

Oleksiak A, Klink PC, Postma A, van der Ham IJM, Lankheet MJ, van Wezel RJA. 2011. Spatial summation in macaque parietal area 7a follows a winner-take-all rule. *J Neurophysiol* **105**:1150–1158. doi:10.1152/jn.00907.2010

Patel GH, Shulman GL, Baker JT, Akbudak E, Snyder AZ, Snyder LH, Corbetta M. 2010. Topographic organization of macaque area LIP. *Proceedings of the National Academy of Sciences* **107**:4728–4733. doi:10/c9cfrp

Poltoratski S, Maier A, Newton AT, Tong F. 2019. Figure-Ground Modulation in the Human Lateral Geniculate Nucleus Is Distinguishable from Top- Down Attention. *CURR BIOL* 1–11. doi:10.1016/j.cub.2019.04.068

Poltoratski S, Tong F. 2020. Resolving the spatial profile of figure enhancement in human V1 through population receptive field modeling. *J Neurosci* JN-RM-2377-19. doi:10.1523/jneurosci.2377-19.2020

Poort J, Raudies F, Wannig A, Lamme VAF, Neumann H, Roelfsema PR. 2012. The role of attention in figure-ground segregation in areas v1 and v4 of the visual cortex. *Neuron* **75**:143–156. doi:10.1016/j.neuron.2012.04.032

Priebe NJ. 2008. The relationship between subthreshold and suprathreshold ocular dominance in cat primary visual cortex. *J Neurosci* **28**:8553–8559. doi:10.1523/JNEUROSCI.2182-08.2008

Puckett AM, Bollmann S, Junday K, Barth M, Cunnington R. 2020. Bayesian population receptive field modeling in human somatosensory cortex. *NeuroImage* **208**:116465. doi:10/ggt2mx

Ray S, Maunsell JHR. 2014. Do gamma oscillations play a role in cerebral cortex? *Trends Cogn Sci (Regul Ed)* 1–8. doi:10.1016/j.tics.2014.12.002

Ray S, Maunsell JHR. 2011. Different Origins of Gamma Rhythm and High-Gamma Activity in Macaque Visual Cortex. *PLoS Biol* **9**:e1000610. doi:10.1371/journal.pbio.1000610.g008

bioRxiv preprint doi: https://doi.org/10.1101/2020.09.05.284133; this version posted September 8, 2020. The copyright holder for this preprint (which was not certified by peer review) is the author/funder, who has granted bioRxiv a license to display the preprint in perpetuity. It is made available under aCC-BY-NC 4.0 International license.

Rees G, Friston K, Koch C. 2000. A direct quantitative relationship between the functional properties of human and macaque V5. *Nat Neurosci* **3**:716–723.

Reveley C, Gruslys A, Ye FQ, Glen D, Samaha J, E. Russ B, Saad Z, K. Seth A, Leopold DA, Saleem KS. 2016. Three-Dimensional Digital Template Atlas of the Macaque Brain. *Cerebral Cortex*. doi:10.1093/cercor/bhw248

Rolls ET, Thorpe SJ, Maddison SP. 1983. Responses of striatal neurons in the behaving monkey. 1. Head of the caudate nucleus. *Behavioural Brain Research* **7**:179–210. doi:10/czdgm8

Saalmann YB, Pinsk MA, Wang L, Li X, Kastner S. 2012. The pulvinar regulates information transmission between cortical areas based on attention demands. *Science* **337**:753–756. doi:10.1126/science.1223082

Saygin AP, Sereno MI. 2008. Retinotopy and Attention in Human Occipital, Temporal, Parietal, and Frontal Cortex. *Cereb Cortex* **18**:2158–2168. doi:10/dtms3d

Schneider KA, Richter MC, Kastner S. 2004. Retinotopic Organization and Functional Subdivisions of the Human Lateral Geniculate Nucleus: A High-Resolution Functional Magnetic Resonance Imaging Study. *J Neurosci* **24**:8975–8985. doi:10/bvzk25

Scholvinck ML, Maier A, Frank QY, Duyn JH, Leopold DA. 2010. Neural basis of global resting-state fMRI activity. *Proc Natl Acad Sci USA* **107**:10238–10243. doi:10.1073/pnas.0913110107/-/DCSupplemental

Schwarzkopf DS, Anderson EJ, Haas B de, White SJ, Rees G. 2014. Larger Extrastriate Population Receptive Fields in Autism Spectrum Disorders. *J Neurosci* **34**:2713–2724. doi:10/f5sx87

Seidlitz J, Sponheim C, Glen D, Ye FQ, Saleem KS, Leopold DA, Ungerleider L, Messinger A. 2017. A population MRI brain template and analysis tools for the macaque. *Neuroimage* 1–11. doi:10.1016/j.neuroimage.2017.04.063

Sereno MI, Dale AM, Reppas JB, Kwong KK, Belliveau JW, Brady TJ, Rosen BR, Tootell RB. 1995. Borders of multiple visual areas in humans revealed by functional magnetic resonance imaging. *Science* **268**:889–893.

Shao Y, Keliris GA, Papanikolaou A, Fischer MD, Zobor D, Jägle H, Logothetis NK, Smirnakis SM. 2013. Visual cortex organisation in a macaque monkey with macular degeneration. *The European journal of neuroscience* **38**:3456–3464. doi:10.1111/ejn.12349

Shen L, Han B, Lange FP de. 2020. Apparent motion induces activity suppression in early visual cortex and impairs visual detection. *J Neurosci*. doi:10/ggz9kf

Sherrington CS. 1906. Observations on the scratch-reflex in the spinal dog. *The Journal of Physiology* **34**:1–50. doi:10/ggj5gs

Shmuel A, Augath M, Oeltermann A, Logothetis NK. 2006. Negative functional MRI response correlates with decreases in neuronal activity in monkey visual area V1. *Nat Neurosci* **9**:569–577. doi:10.1038/nn1675

Silson EH, Reynolds RC, Kravitz DJ, Baker CI. 2018. Differential Sampling of Visual Space in Ventral and Dorsal Early Visual Cortex. *J Neurosci* **38**:2294–2303. doi:10.1523/JNEUROSCI.2717-17.2018

Smith AT, Williams AL, Singh KD. 2004. Negative BOLD in the visual cortex: Evidence against blood stealing. *Hum Brain Mapp* **21**:213–220. doi:10.1002/hbm.20017

bioRxiv preprint doi: https://doi.org/10.1101/2020.09.05.284133; this version posted September 8, 2020. The copyright holder for this preprint (which was not certified by peer review) is the author/funder, who has granted bioRxiv a license to display the preprint in perpetuity. It is made available under aCC-BY-NC 4.0 International license.

Stoll S, Finlayson NJ, Schwarzkopf DS. 2020. Topographic Signatures of Global Object Perception in Human Visual Cortexa. *NeuroImage* 116926. doi:10/ggz9kg

Supèr H, Roelfsema PR. 2005. Chronic multiunit recordings in behaving animals: advantages and limitationsDevelopment, Dynamics and Pathiology of Neuronal Networks: From Molecules to Functional Circuits. Elsevier. pp. 263–282.

Szinte M, Knapen T. 2019. Visual Organization of the Default Network. *Cereb Cortex*. doi:10/ggtm5t

Tani N, Joly O, Iwamuro H, Uhrig L, Wiggins CJ, Poupon C, Kolster H, Vanduffel W, Le Bihan D, Palfi S, Jarraya B. 2011. Direct visualization of non-human primate subcortical nuclei with contrast-enhanced high field MRI. *Neuroimage* **58**:60–68. doi:10.1016/j.neuroimage.2011.06.019

Thomas JM, Huber E, Stecker GC, Boynton GM, Saenz M, Fine I. 2015. Population receptive field estimates of human auditory cortex. *NeuroImage* **105**:428–439. doi:10/f6sbd8

Valencia-Alfonso C-E, Luigjes J, Smolders R, Cohen MX, Levar N, Mazaheri A, van den Munckhof P, Schuurman PR, van den Brink W, Denys D. 2012. Effective deep brain stimulation in heroin addiction: a case report with complementary intracranial electroencephalogram. *BIOL PSYCHIAT* **71**:e35-7. doi:10.1016/j.biopsych.2011.12.013

van Beest E, Mukherjee S, Kirchberger L, Schnabel UH, van der Togt C, Teeuwen RRM, Barsegyan A, Roelfsema P, Self MW. 2019. A Fovea-Like Representation of Space in Mouse Visual Cortex (SSRN Scholarly Paper No. ID 3441090). Rochester, NY: Social Science Research Network. doi:10.2139/ssrn.3441090

van Es DM, van der Zwaag W, Knapen T. 2019. Topographic Maps of Visual Space in the Human Cerebellum. *CURR BIOL* 1–10. doi:10.1016/j.cub.2019.04.012

Van Essen DC, Newsome WT, Maunsell JHR. 1984. The visual field representation in striate cortex of the macaque monkey: Asymmetries, anisotropies, and individual variability. *Vision Research* **24**:429–448. doi:10.1016/0042-6989(84)90041-5

van Kerkoerle T, Self MW, Dagnino B, Gariel-Mathis M-A, Poort J, van der Togt C, Roelfsema PR. 2014. Alpha and gamma oscillations characterize feedback and feedforward processing in monkey visual cortex. *Proc Natl Acad Sci USA* **111**:14332–14341. doi:10.1073/pnas.1402773111

Vanduffel W. 2018. Long-term value memory in primates. *Proc Natl Acad Sci USA* **115**:1956–1958. doi:10.1073/pnas.1800247115

Vanduffel W, Fize D, Mandeville JB, Nelissen K, Van Hecke P, Rosen BR, Tootell RB, Orban GA. 2001. Visual motion processing investigated using contrast agent-enhanced fMRI in awake behaving monkeys. *Neuron* **32**:565–577.

Victor JD, Purpura K, Katz E, Mao B. 1994. Population encoding of spatial frequency, orientation, and color in macaque V1. *J Neurophysiol* **72**:2151–2166. doi:10.1152/jn.1994.72.5.2151

Viswanathan A, Freeman RD. 2007. Neurometabolic coupling in cerebral cortex reflects synaptic more than spiking activity. *Nature Neuroscience* **10**:1308–1312. doi:10/cbxvpj

bioRxiv preprint doi: https://doi.org/10.1101/2020.09.05.284133; this version posted September 8, 2020. The copyright holder for this preprint (which was not certified by peer review) is the author/funder, who has granted bioRxiv a license to display the preprint in perpetuity. It is made available under aCC-BY-NC 4.0 International license.

Wandell BA, Dumoulin SO, Brewer AA. 2007. Visual field maps in human cortex. *Neuron* **56**:366–383. doi:10.1016/j.neuron.2007.10.012

Wandell BA, Winawer J. 2015. Computational neuroimaging and population receptive fields. *Trends Cogn Sci (Regul Ed)* **19**:349–357. doi:10.1016/j.tics.2015.03.009

Wandell BA, Winawer J. 2010. Imaging retinotopic maps in the human brain. *Vision Res*. doi:10.1016/j.visres.2010.08.004

Welbourne LE, Morland AB, Wade AR. 2018. Population receptive field (pRF) measurements of chromatic responses in human visual cortex using fMRI. *Neuroimage* **167**:84–94. doi:10.1016/j.neuroimage.2017.11.022

Winawer J, Kay KN, Foster BL, Rauschecker AM, Parvizi J, Wandell BA. 2013. Asynchronous Broadband Signals Are the Principal Source of the BOLD Response in Human Visual Cortex. *CURR BIOL* **23**:1145–1153. doi:10.1016/j.cub.2013.05.001

Winder AT, Echagarruga C, Zhang Q, Drew PJ. 2017. Weak correlations between hemodynamic signals and ongoing neural activity during the resting state. *Nat Neurosci* 1–16. doi:10.1038/s41593-017-0007-y

Woolrich MW, Behrens TEJ, Smith SM. 2004. Constrained linear basis sets for HRF modelling using Variational Bayes. *Neuroimage* **21**:1748–1761. doi:10.1016/j.neuroimage.2003.12.024

Zhu Q, Vanduffel W. 2019. Submillimeter fMRI reveals a layout of dorsal visual cortex in macaques, remarkably similar to New World monkeys. *Proc Natl Acad Sci USA* **32**:201805561–6. doi:10.1073/pnas.1805561116

Zuiderbaan W, Harvey BM, Dumoulin SO. 2017. Image identification from brain activity using the population receptive field model. *PLOS ONE* **12**:e0183295. doi:10/gfwjvr

Zuiderbaan W, Harvey BM, Dumoulin SO. 2012. Modeling center-surround configurations in population receptive fields using fMRI. *J Vis* **12**:10–10. doi:10.1167/12.3.10

bioRxiv preprint doi: https://doi.org/10.1101/2020.09.05.284133; this version posted September 8, 2020. The copyright holder for this preprint (which was not certified by peer review) is the author/funder, who has granted bioRxiv a license to display the preprint in perpetuity. It is made available under aCC-BY-NC 4.0 International license.

Supplemental Figures

- **Supplemental Table T1**
  - ROI abbreviations
- **Supplemental Figure S1-S14**
  - S1: related to Figure 2
  - S2: related to Figure 3
  - S3: related to Figure 4
  - S4: related to Figure 4
  - S5: related to Figure 4
  - S6: Effect of HRF on fit accuracy
  - S7: related to Figure 5
  - S8: related to Figure 6
  - S9: related to Figure 5
  - S10: Comparison MUA-pRF & MUA-RF
  - S11: related to Figure 8
  - S12: related to Figure 10
  - S13: related to Figure 11
  - S14: related to Figure 12

bioRxiv preprint doi: https://doi.org/10.1101/2020.09.05.284133; this version posted September 8, 2020. The copyright holder for this preprint (which was not certified by peer review) is the author/funder, who has granted bioRxiv a license to display the preprint in perpetuity. It is made available under aCC-BY-NC 4.0 International license.

Supplemental Table 1: ROI abbreviations

ROI abbreviation	ROI full name (BA = Brodmann Area)
V1	Primary visual cortex
V2	Visual area V2
V3	Visual area V3
V3A	Visual area V3A
V4	Visual area V4
MT	Middle Temporal visual area
MST	Medial Superior Temporal cortex
TEO	Inferior temporal cortical area TEO
TAa	Temporal area TAa
Tpt	Auditory association cortex (Temporoparietal)
TPO	Temporo-parietal-occipital junction
FST	Fundus of the superior temporal visual areas
A1	Primary auditory cortex
ML	Middle lateral, belt region of the auditory cortex
AL	Anterior lateral, belt region of the auditory cortex
PULV	Pulvinar
LGN	Lateral geniculate nucleus
STR	Striatum
LIP	Lateral intraparietal cortex
VIP	Ventral intraparietal cortex
5	BA 5 (parietal area PE)
7	BA 7, includes BA 7a (Opt/PG) and BA 7b (PFG/PF)
SI	Primary somatosensory cortex (BA 1, 2, and 3)
SII	Secondary somatosensory cortex
F2	Area F2, dorsal caudal premotor cortex
F4	Area F4, ventral caudal premotor cortex
F5	Area F5, ventral rostral premotor cortex
F7	Area F7, dorsal rostral premotor cortex
8	BA 8 (includes the Frontal Eye Fields)
CINp	Poster cingulate cortex (BA 23)
CINa	Anterior cingulate cortex (BA 24c, and BA 32)
OFC	Orbitofrontal cortex (BA 12)
INS	Insular cortex (includes BA 13)
DLPFC	Dorsolateral prefrontal cortex (BA 10, and BA 46)
VMPFC	Ventromedial prefrontal cortex (BA 14)

Occipital lobe	Temporal lobe	Subcortical	Parietal lobe	Frontal lobe

bioRxiv preprint doi: https://doi.org/10.1101/2020.09.05.284133; this version posted September 8, 2020. The copyright holder for this preprint (which was not certified by peer review) is the author/funder, who has granted bioRxiv a license to display the preprint in perpetuity. It is made available under aCC-BY-NC 4.0 International license.

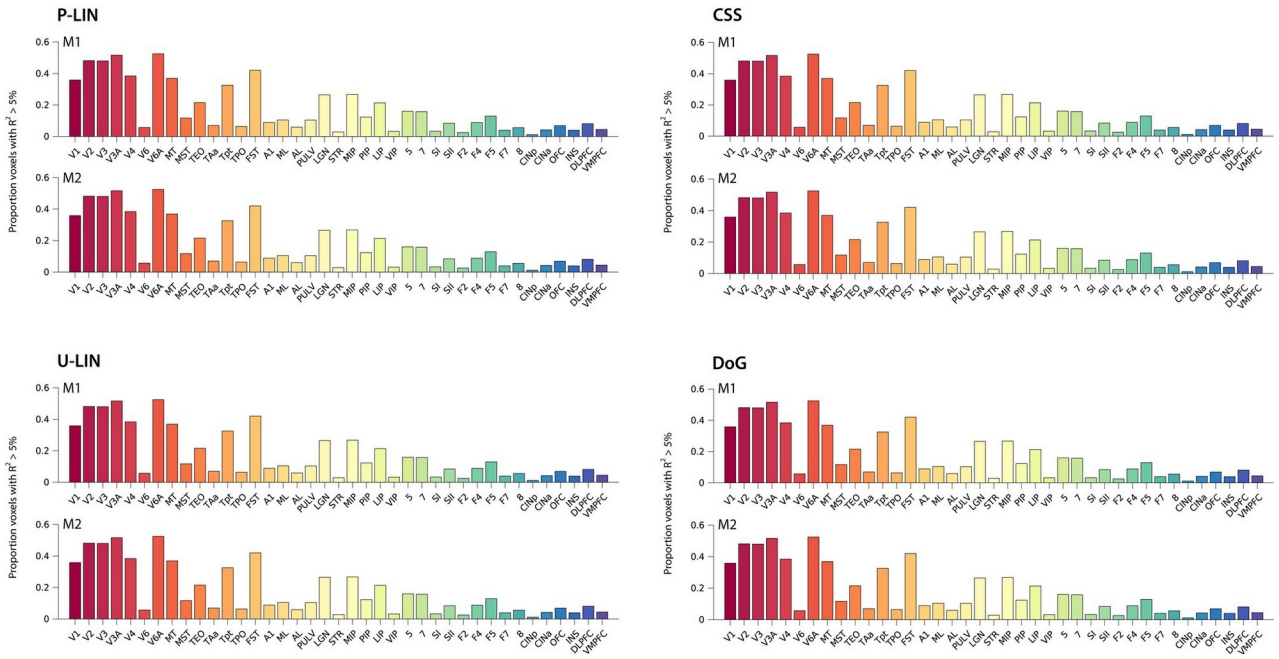

Supplemental Figure S1. Proportion of voxels with R^2 > 5% per ROI. For both animals (M1, M2) an all four pRF models. Supplement to Figure 2B that reports absolute numbers of voxels per area.

bioRxiv preprint doi: https://doi.org/10.1101/2020.09.05.284133; this version posted September 8, 2020. The copyright holder for this preprint (which was not certified by peer review) is the author/funder, who has granted bioRxiv a license to display the preprint in perpetuity. It is made available under aCC-BY-NC 4.0 International license.

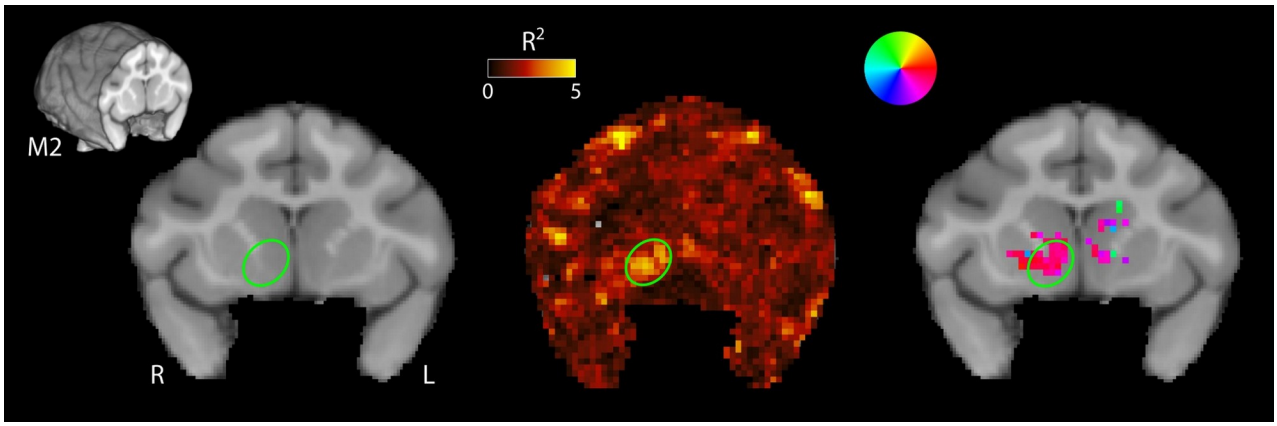

Supplemental Figure S2. Voxels in the right nucleus accumbens (Nac) have ipsilateral pRFs. The right NAc in the ventral striatum (green outline) is retinotopically tuned in both monkeys (only M2 shown). Although R^2 values are lower than in the cortex or thalamus, they stand out from the surrounding regions. Polar angle maps of the fitted pRFs indicate that the right NAc is tuned to visual information in the right (ipsilateral) visual field.

bioRxiv preprint doi: https://doi.org/10.1101/2020.09.05.284133; this version posted September 8, 2020. The copyright holder for this preprint (which was not certified by peer review) is the author/funder, who has granted bioRxiv a license to display the preprint in perpetuity. It is made available under aCC-BY-NC 4.0 International license.

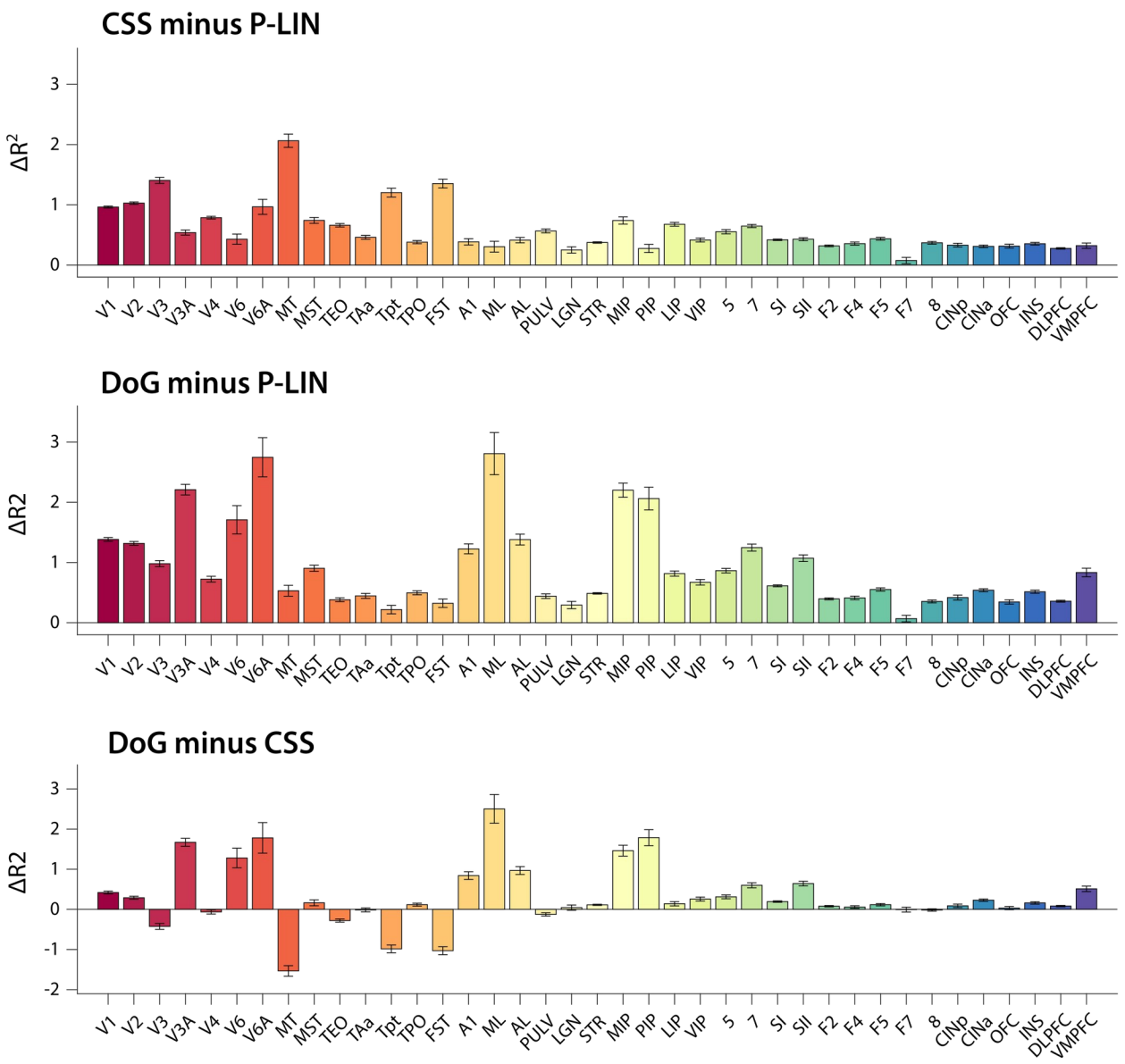

Supplemental Figure S3. Fit accuracy advantage of CSS and DoG models across brain areas. Both the CSS (top panel) and DoG (middle panel) models had a higher fit accuracy (cross-validated R2) than the conventional P-LIN model across all brain regions with retinotopic information. Difference between the CSS and DoG was minimal (bottom panel).

bioRxiv preprint doi: https://doi.org/10.1101/2020.09.05.284133; this version posted September 8, 2020. The copyright holder for this preprint (which was not certified by peer review) is the author/funder, who has granted bioRxiv a license to display the preprint in perpetuity. It is made available under aCC-BY-NC 4.0 International license.

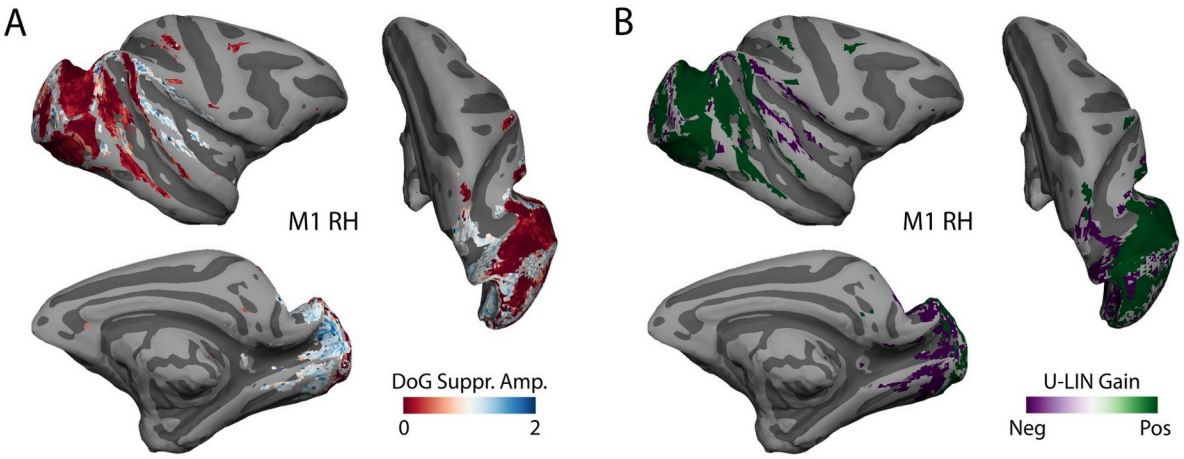

Supplemental Figure S4. (A) Normalized amplitude of the suppressive surround Gaussian in the DoG model fits (R^2 > 5%). Values larger than one (blue tints) indicate that the suppressive surround has a larger amplitude than the positively responding center Gaussian. The right hemisphere of M1 is shown as an example. Voxels with a strong suppressive component were found in the medial occipital and parietal cortices, and around the lateral sulcus. **(B)** Similar example display as in (A), but here the gain value of the of U-LIN fits is shown for voxels with R^2 > 5%. Green tints represent positive gain values, purple tints indicate negative gain values (i.e., negative or suppressive BOLD responses). Negative gain values are seen in the same voxels that have a strong suppressive surround in the DoG model suggesting that these voxels are best characterized by a suppressive or negative response to visual stimuli.

bioRxiv preprint doi: https://doi.org/10.1101/2020.09.05.284133; this version posted September 8, 2020. The copyright holder for this preprint (which was not certified by peer review) is the author/funder, who has granted bioRxiv a license to display the preprint in perpetuity. It is made available under aCC-BY-NC 4.0 International license.

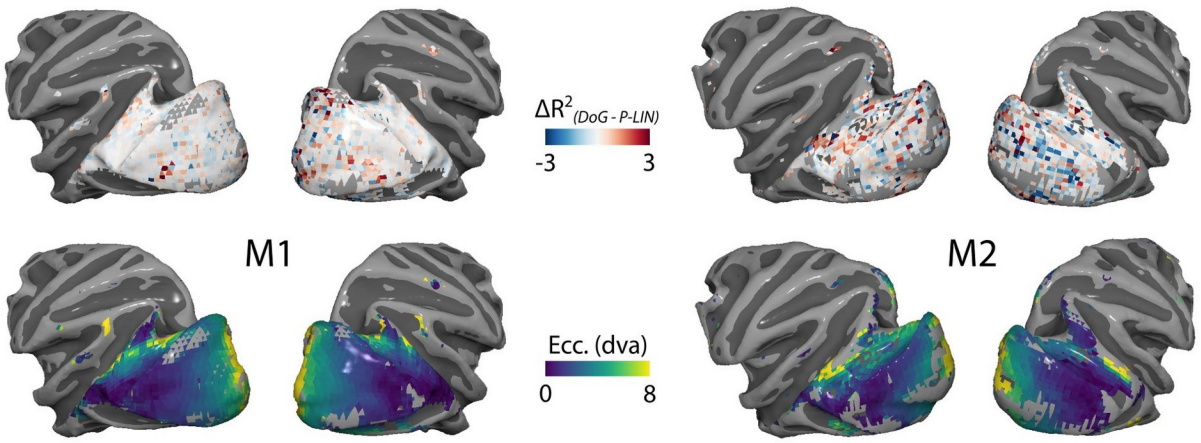

Supplemental Figure S5. Voxels with a good fit for both DoG and P-LIN models, were found in both animals (M1 and M2). Voxels for which the DoG model outperformed the P-LIN model were found throughout visual cortex (top panels), but not clearly clustered in cortical space nor specific for either foveal or peripheral eccentricities (bottom panels).

bioRxiv preprint doi: https://doi.org/10.1101/2020.09.05.284133; this version posted September 8, 2020. The copyright holder for this preprint (which was not certified by peer review) is the author/funder, who has granted bioRxiv a license to display the preprint in perpetuity. It is made available under aCC-BY-NC 4.0 International license.

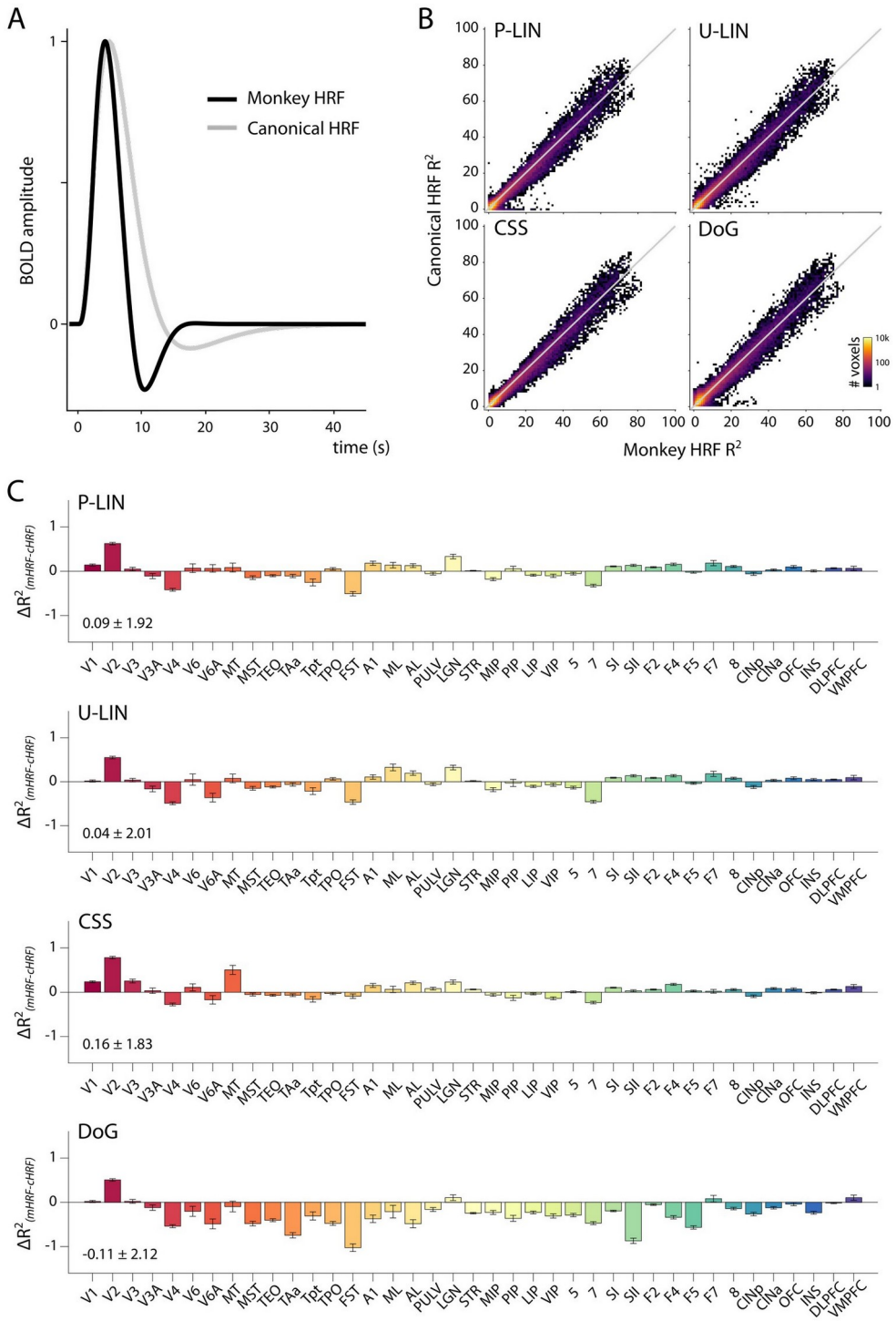

Supplemental Figure S6. Comparison of hemodynamic response functions (HRFs). (A) All pRF models were fit on the BOLD response with two distinct HRFs: a monkey-specific HRF (see Material and Methods for details on how this was estimated) and a canonical HRF provided by the analyzePRF toolbox. The monkey HRF (black line) had a faster decay and more pronounced negative component than the canonical HRF (gray line). **(B)** The choice of HRF had a relatively small effect on the fit accuracy (R^2)of all four models. The color map in this binned scatter-plot (1 × 1 % bins) indicates the number of voxels. **(C)** Mean difference in R^2 value between the HRFs for all models and ROI's. There is a small advantage of the monkey HRF in early visual areas for all models. For the DoG model the canonical HRF fit slightly better in later cortical areas. The inset text indicates the mean R^2 difference (HRF_{monkey} - $HRF_{canonical}$) over all voxels ± the standard deviation.

bioRxiv preprint doi: https://doi.org/10.1101/2020.09.05.284133; this version posted September 8, 2020. The copyright holder for this preprint (which was not certified by peer review) is the author/funder, who has granted bioRxiv a license to display the preprint in perpetuity. It is made available under aCC-BY-NC 4.0 International license.

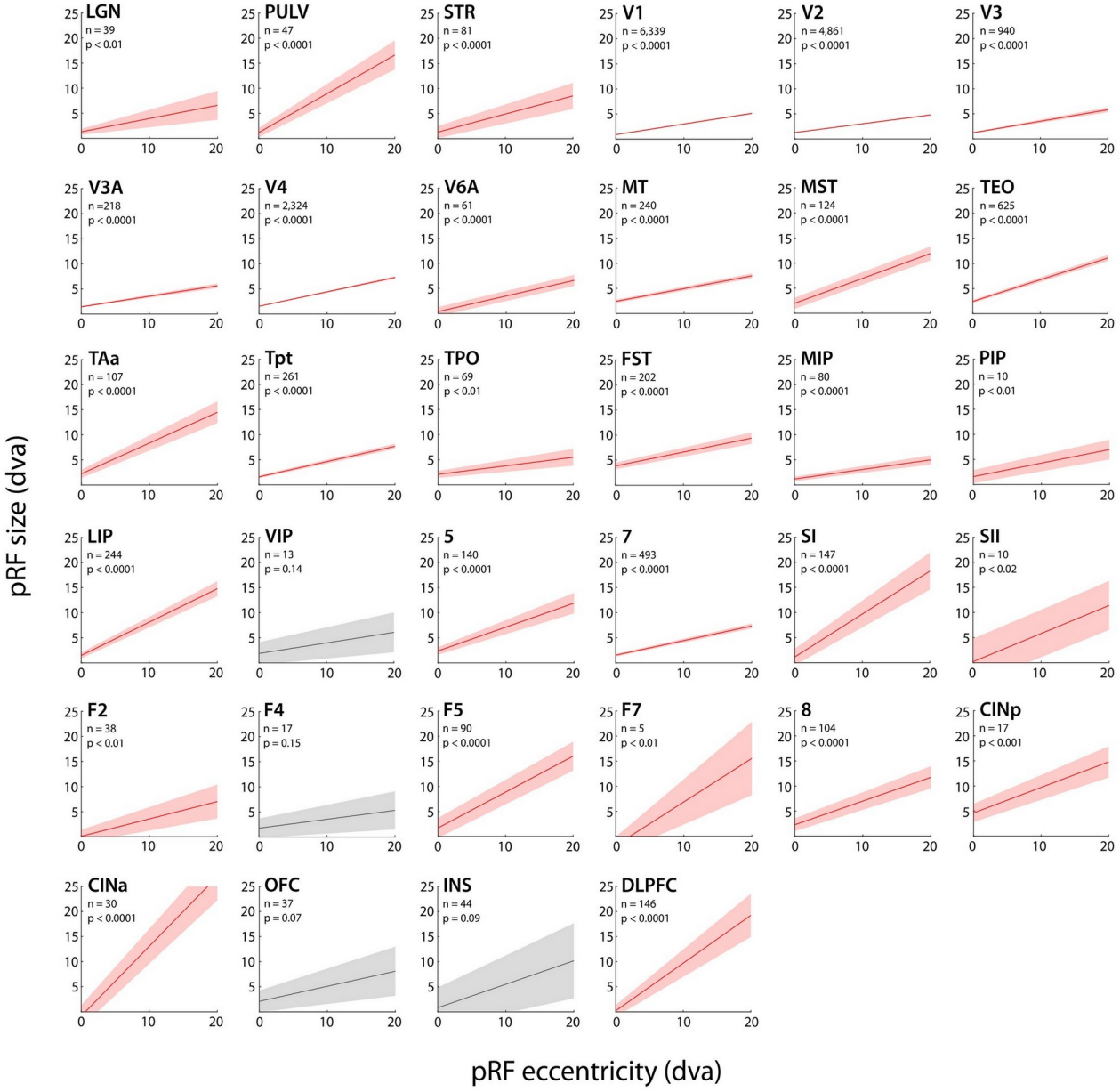

Supplemental Figure S7. Eccentricity-size relationship for all ROI's. Linear fits (intercept and slope) on the eccentricity-size relationship per brain area. Shaded areas indicate the 95% confidence interval of the fit, the *n*-value indicates the number of voxels (R^2 > 5%) the fit was based on. Areas with linear fits plotted in red have a significant slope. For the few areas where the slope was not significant (gray plots), there was still a clear trend towards a positive correlation.

bioRxiv preprint doi: https://doi.org/10.1101/2020.09.05.284133; this version posted September 8, 2020. The copyright holder for this preprint (which was not certified by peer review) is the author/funder, who has granted bioRxiv a license to display the preprint in perpetuity. It is made available under aCC-BY-NC 4.0 International license.

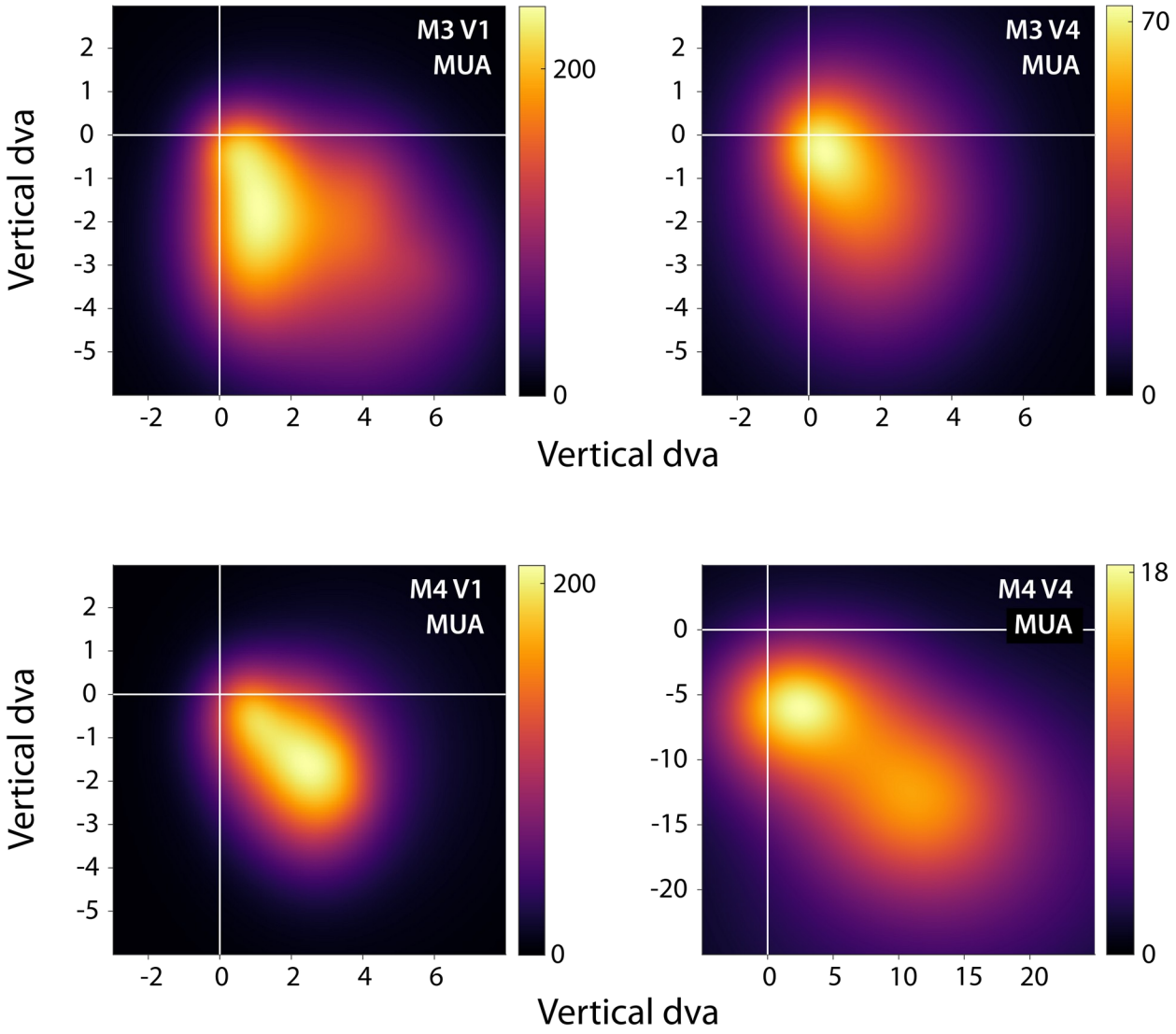

Supplemental Figure S8. Heatmaps of visual field coverage of the Utah arrays. pRFs with a fit accuracy of R^2 > 50% based on the MUA and the CSS model were reconstructed in 2-D, normalized to their peak value, and summed across electrodes. This results in heatmap representations of the visual field coverage for V1 and V4 arrays in both animals. Hotter colors represent the presence of more (proportions of) pRFs in that spatial location of the visual field. See Figure 7 for individual pRF locations.

bioRxiv preprint doi: https://doi.org/10.1101/2020.09.05.284133; this version posted September 8, 2020. The copyright holder for this preprint (which was not certified by peer review) is the author/funder, who has granted bioRxiv a license to display the preprint in perpetuity. It is made available under aCC-BY-NC 4.0 International license.

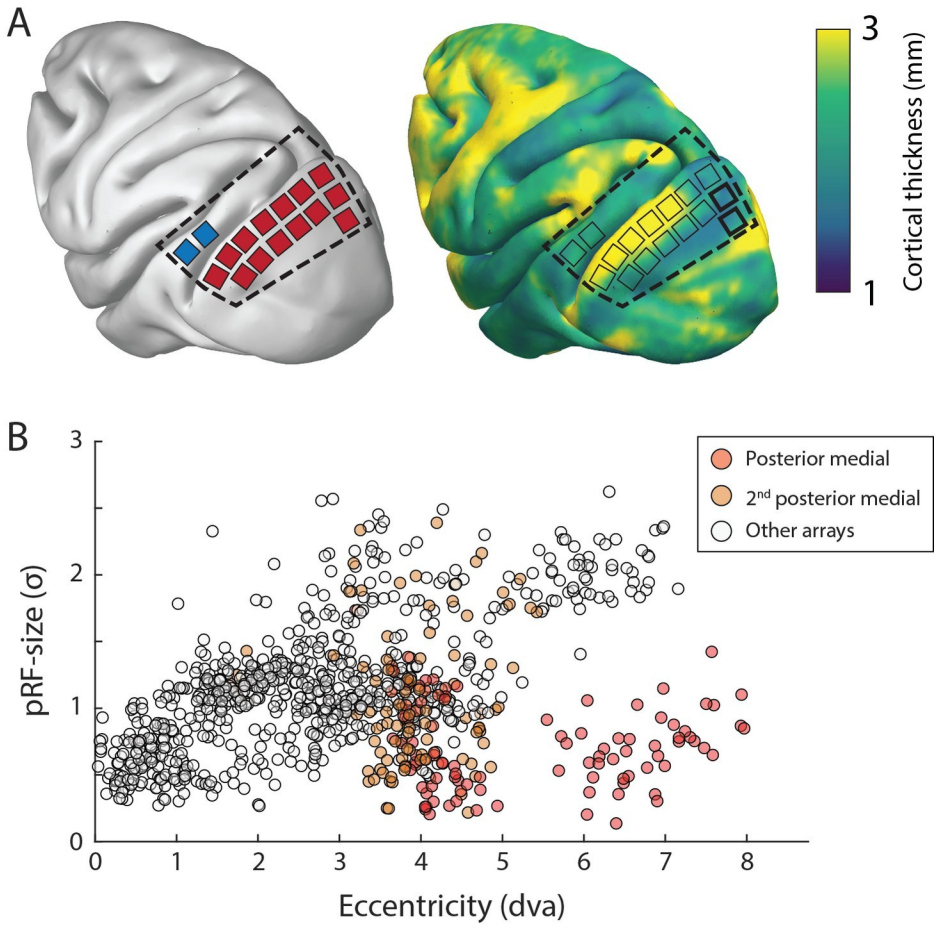

Supplemental Figure S9. Arrays with deviating pRF sizes. (A) Schematic representation of the location of the craniotomy made during surgery (dashed line) and the implanted electrode arrays (left panel, red: V1, blue: V4) depicted on the NMT template brain. The color map in the right panel indicates the thickness of the cortical gray matter of the NMT template brain. **(B)** For both monkeys, the estimated pRF sizes for the V1 electrode arrays in the posterior medial corner of the craniotomy (red and orange circles; thick lines in the right panel of **A**) indicate arrays with Rfs that were surprisingly small for their eccentricity, compared to the size-eccentricity correlation in all other arrays (gray circles). Given the length of the array electrodes (1.5 mm), the typical thickness of the striate cortex, and these small pRF sizes, it is likely that the deviating pRFs do not reflect the tuning of V1 neurons, but instead that of the underlying geniculostriate white matter. The pRFs in panel B were estimated by the CSS model with $R^2 > 70\%$.

bioRxiv preprint doi: https://doi.org/10.1101/2020.09.05.284133; this version posted September 8, 2020. The copyright holder for this preprint (which was not certified by peer review) is the author/funder, who has granted bioRxiv a license to display the preprint in perpetuity. It is made available under aCC-BY-NC 4.0 International license.

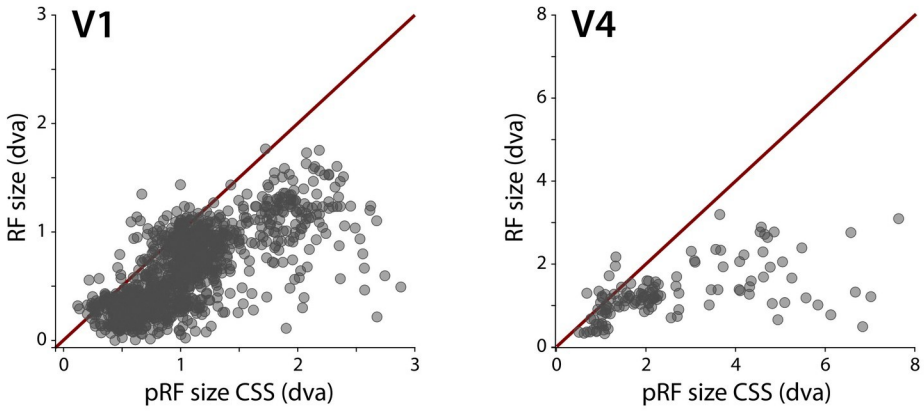

Supplemental Figure S10. Comparison of pRF sizes from CSS-model fits on MUA with RF-sizes derived from conventional MUA-based RF-mapping. Dots are individual electrodes (left: V1, right: V4). The red line is the unity line. The plots are zoomed to a restricted size -range.

bioRxiv preprint doi: https://doi.org/10.1101/2020.09.05.284133; this version posted September 8, 2020. The copyright holder for this preprint (which was not certified by peer review) is the author/funder, who has granted bioRxiv a license to display the preprint in perpetuity. It is made available under aCC-BY-NC 4.0 International license.

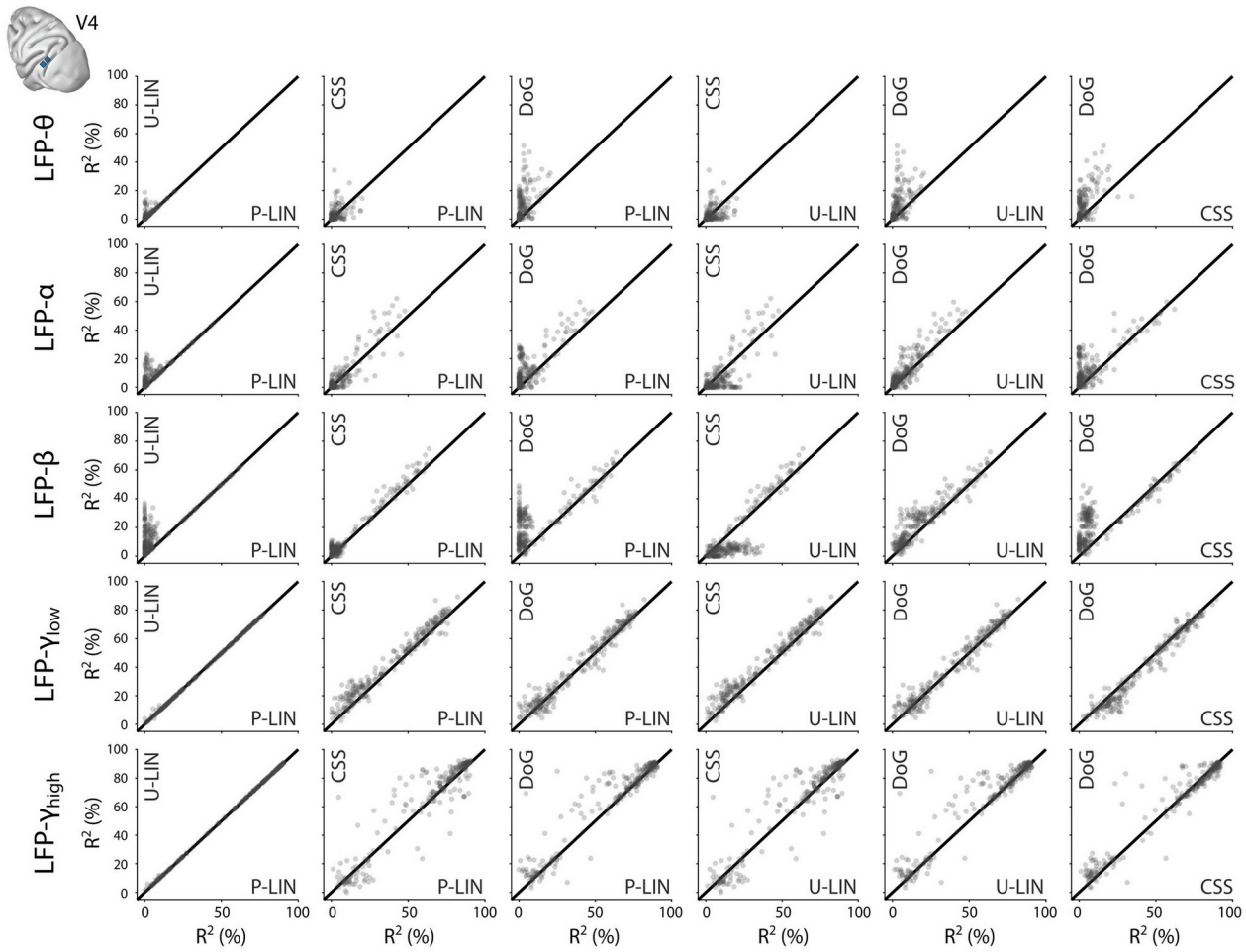

Supplemental Figure S11. Comparison of LFP-based fit-results from the four pRF models for V4 electrodes. Scatter-plots comparing the fit accuracy across pRF models and LFP frequency bands. Each dot represents an electrode.

bioRxiv preprint doi: https://doi.org/10.1101/2020.09.05.284133; this version posted September 8, 2020. The copyright holder for this preprint (which was not certified by peer review) is the author/funder, who has granted bioRxiv a license to display the preprint in perpetuity. It is made available under aCC-BY-NC 4.0 International license.

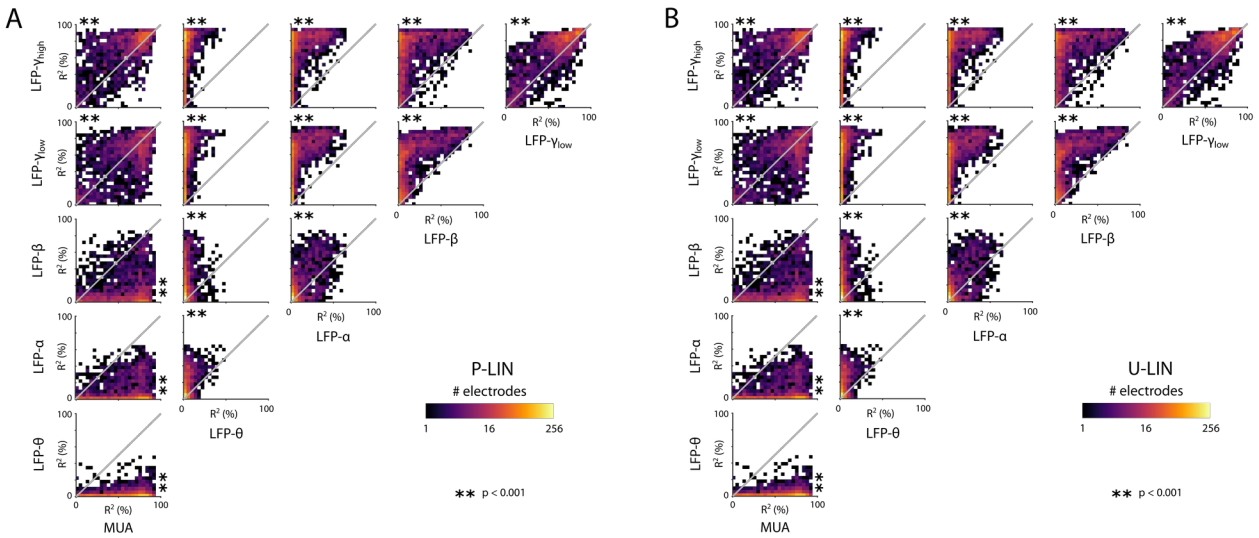

Supplemental Figure S12. Comparison of pRF fit accuracies for MUA and LFP signals from the same electrodes. (A) Binned scatter plots comparing the R^2 values of pRF fits from the P-LIN model based on different electrophysiological signals. The gray line indicates similar fit accuracy for the two signals. Colors indicate the number of electrodes in a 4 × 4 % two-dimensional bin (logarithmic scale). Asterisks indicate which of the two signals has significantly higher R^2 values (Kruskal-Wallis, with post-hoc Tukey's HSD multiple comparisons of mean rank, $^{**}p < 0.001$). **(B)** Same as in (A) but for the U-LIN model. Figure 10 shows similar results for the CSS and DoG models.

bioRxiv preprint doi: https://doi.org/10.1101/2020.09.05.284133; this version posted September 8, 2020. The copyright holder for this preprint (which was not certified by peer review) is the author/funder, who has granted bioRxiv a license to display the preprint in perpetuity. It is made available under aCC-BY-NC 4.0 International license.

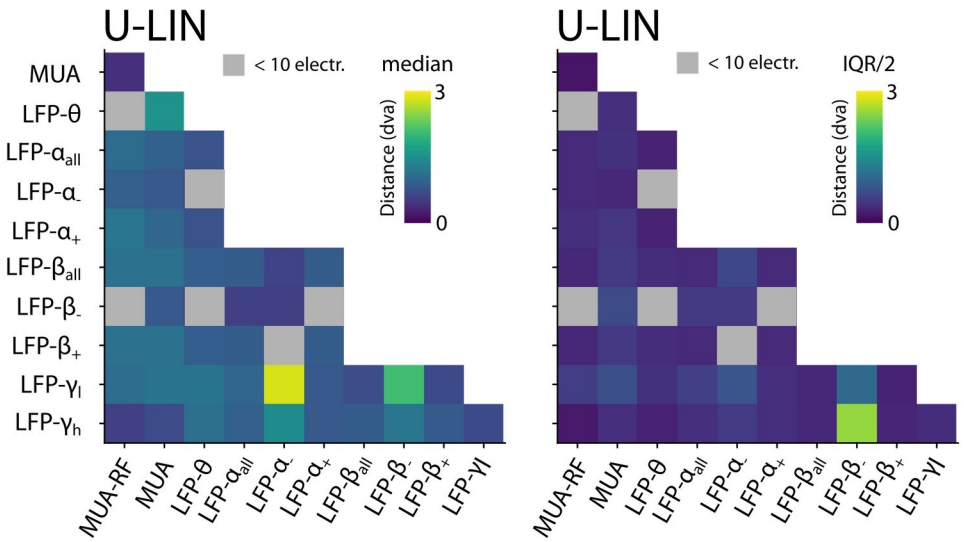

Supplemental Figure S13. Distance between U-LIN pRF center estimates from different electrophysiological signals recorded on the same electrodes. (A) Median distance (left) and half IQR (right) between electrophysiological signals. Electrodes were only included when their pRF fit accuracy R^2 > 25% (MUA, LFP) or the SNR > 3 (MUA-RF). Gray squares indicate channels.

bioRxiv preprint doi: https://doi.org/10.1101/2020.09.05.284133; this version posted September 8, 2020. The copyright holder for this preprint (which was not certified by peer review) is the author/funder, who has granted bioRxiv a license to display the preprint in perpetuity. It is made available under aCC-BY-NC 4.0 International license.

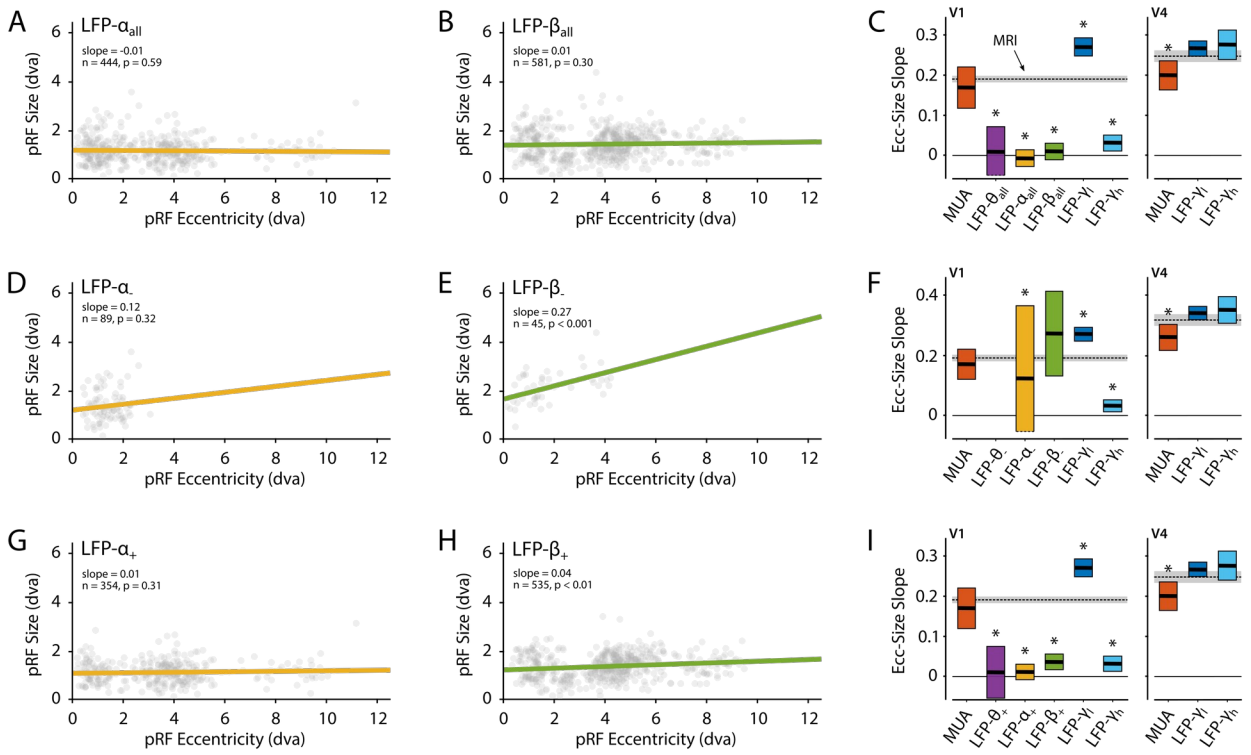

Supplemental Figure S14. Eccentricity-size relationship for LFP-α and LFP-β split by positive and negative gains from U-LIN fits. **(A)** Eccentricity-size relationship based on U-LIN estimates from LFP-α for all electrodes with R^2 > 25%. **(B)** Same as (A) but for LFP-β. **(C)** Comparison of eccentricity-size slope values from the U-LIN model for all electrophysiology signals with the MRI U-LIN fits (dashed line with 95% CI) in V1 (left) and V4 (right) respectively. Black horizontal lines indicate the estimated slope, colored boxes denote the 95% CI. Asterisks indicate a significant interaction between signal type and eccentricity from a linear mixed model comparing the eccentricity size relationship of MRI-based pRFs with each electrophysiological signal (i.e., the absence of such interaction indicates that there is no evidence for a difference in slope between the electrophysiological signal and the MRI-based pRFs).**(D)** Same as in (A), but only electrodes with negative gain values are included. **(E)** Same as (B), but only electrodes with negative gain values are included. **(F)** Same as (C), but only electrodes with negative gain values are included for the low-frequency components of the LFP. **(G)** Same as in (A), but only electrodes with positive gain values are included. **(H)** Same as (B), but only electrodes with positive gain values are included. **(I)** Same as (C), but only electrodes with positive gain values are included for the low-frequency components of the LFP. LFP-θ: 4-8 Hz; LFP-α: 8-16 Hz; LFP-β: 16-30 Hz; LFP-γ_l: 30-60 Hz; LFP-γ_h: 60-120 Hz.